Development and Application of Multidimensional Computational Models for Hall Thrusters

by

Horatiu Cosmin Dragnea

A dissertation submitted in partial fulfillment
of the requirements for the degree of
Doctor of Philosophy
(Aerospace Engineering)
in The University of Michigan
2018

Doctoral Committee:

Professor Iain D. Boyd, Chair
Professor John E. Foster
Professor Alec D. Gallimore
Professor Mark J. Kushner

Indeed, we are accused of tomfoolery more than we deserve. We then simply admit to being in good company with the rest of plasma physics, with theorists and experimentalists who also have their kit bags of approximate (and occasionally inaccurate) tools.

Charles K. Birdsall

Computational setup circa 2013.

Horatiu Cosmin Dragnea

horatiud@umich.edu

ORCID iD: 0000-0003-4461-0428

To my parents and my sister.

ACKNOWLEDGEMENTS

I first want to acknowledge my family. You have always inspired me to work hard and stay focused. Without your support and guidance none of this would have been possible.

Prof. Iain Boyd, thank you for bringing me to Michigan. I couldn't have hoped for a better relationship with my adviser. You were there for me when I was getting started and didn't quite know what I was doing, but as I progressed in my studies you gave me the freedom to focus on what I was interested in. Prof. Alec Gallimore, thank you for welcoming me at PEPL! Prof. Mark Kushner, your "Physical Processes in Plasmas" class provided perhaps the most clear descriptions of plasma related phenomena. And the plasma ball that you brought that fist day of class made it clear it was going to be a great class! Prof. John Foster, thank you for you thoughtful questions and comments following my pre-defense.

Throughout the years my work has been supported by several different sources. I would like to first thank the University of Michigan/AFRL Center of Excellence in Electric Propulsion (MACEEP) which provided funding for the thruster erosion project through AFRL Grant No. F9550-09-1-0695. Next, I had the privilege of being awarded a NASA Space Technology Research Fellowship (grant number NNX13AL51H). This award not only funded my research, but provided great opportunities to learn directly from the top NASA researchers in the field during my summer terms as a

At GRC I would like to thank George Souals for being my NSTRF mentor, and also Dr. John Yim for overseeing my stay. At JPL I would like to thank Dr. Alejandro Lopez Ortega for bringing me in for the summer and helping me get started with Hall2De and overseeing my krypton work. I would also like to acknowledge Dr. Yiangos Mikellides for all his thoughtful comments related to the Hall2De work, and for allowing me to complete the project after I returned to Michigan.

I would like to thank past and present members of NGPDL. Paul, thanks for teaching how easy it is to work in terminal. Ashley, thanks for helping me get started with Monaco, and thanks for being patient and answering all my questions, especially when you were working on your thesis! Brandon, thank you for helping me get started with HPHall, and providing the sputtered boron VDFs. Maria, thanks for providing cathode flow data, and for organizing a fun white-water rafting trip! Ken, thank you for all of your help with the 2D model development, and most importantly for encouraging/pushing me to go down that path. Astrid, thank you for being my conference buddy and listening to my electron model problems.

To the colleagues at PEPL (past and present): thank you for accepting me as an honorary lab member. Ray, thank you for providing clarification on the X2 data,

even though you were long gone from Michigan at that point. Scott, we never got to simultaneously characterize the X3... But I appreciate all your help in providing X2 data, and letting me turn on the thruster! Marcel, thank you for your help in generating those MagNet B field maps. Sarah, thanks for keeping the NHT dream alive! Ethan, thank you for showing me how to work with the gauss meter and the HARP.

All other friends, thank you for keeping me grounded.

TABLE OF CONTENTS

LIST OF FIGURES

LIST OF TABLES

LIST OF APPENDICES

Appendix

LIST OF ABBREVIATIONS

AEHF Advanced Extremely High Frequency

AFRL Air Force Research Laboratory

CEX Charge Exchange

CFD Computational Fluid Dynamics

CRDS Cavity Ring-Down Spectroscopy

DSMC Direct Simulation Monte Carlo

ESA European Space Agency

H6US H6 Unshielded

GPS Global Positioning System

HiVHAc High Voltage Hall Accelerator

HET Hall Effect Thruster

LVTF Large Vacuum Test Facility

MD Molecular Dynamics

NASA National Air and Space Administration

NHT Nested Hall Effect Thruster

PIC Particle-in-Cell

PEPL Plasmadynamics and Electric Propulsion Laboratory

SOR Successive Over-Relaxation

SMART Small Missions for Advanced Research in Technology

SPT Stationary Plasma Thruster

VDF Velocity Distribution Function

ABSTRACT

The goal of this work is to aid the development of high-power Hall-effect thrusters through modeling and simulation. The focus is both on improving the state-of-the-art in the field of Hall thruster numerical simulation, as well as studying several physical processes that are important to Hall thruster development and application. Since Hall thrusters have been in use for more than half a century, they have built a reputation of reliability, however they are known for low power operation with primary applications such as station-keeping and orbit raising. Within the past decade there has been a significant effort to increase the power levels for these electric propulsion devices, but when considering such recent developments, several problems become apparent.

First, as we scale these devices to higher power, higher flow rates and more propellant are needed. This translates into increased costs for ground testing, as well as in-space operation. These issues are addressed through a study of an alternative and less expensive option to the ubiquitous xenon gas: krypton. This new chemical species was added to the Hall2De simulation framework and two thrusters were simulated with krypton propellant. Computed thrust values were found to be within 6% for xenon, and within the 2% experimental measurement error for krypton.

Next, scaling to higher power leads to more energetic ions impacting the thruster surfaces that may in turn lead to higher observed erosion rates. Therefore, we must consider the problem of discharge channel erosion, which is investigated by simulat-

ing an optical experimental diagnostic that is meant to non-invasively determine the erosion rate: cavity-ring-down spectroscopy. The simulation result over predicts the boron number density in the plume by a factor of 3, and this may be attributed to the significant ($\pm 50\%$) uncertainty in the thruster operation time.

Further, the desire to scale Hall thrusters to higher power has led to the idea of concentrically nesting multiple discharge channels into a single thruster. This novel configuration has yielded anomalous thrust gains which have been investigated through a cold gas (neutral) simulation of dual channel operation. In conjunction with significant experimental work performed by colleagues at the Plasmadynamics and Electric Propulsion Laboratory (PEPL) it was found that the anomalous thrust gains may be explained based on the near-plume pressure distribution. In an effort to fully characterize the thruster, a plasma simulation of the single channel mode operation was performed, and thrust was matched to within 9%, while discharge current was matched to within 5% of the measured values. Moreover, it was determined that improved modeling capabilities are required in order to simulate the dual-channel or even independent outer-channel operating modes. Therefore, a new Cartesian 2D axisymmetric electron fluid model is developed, verified and then integrated within an existing state-of-the-art hybrid-particle-in-cell framework.

CHAPTER I

Introduction

1.1 Motivation

Some may question why we should concern ourselves with the study of spacecraft, when there seem to be a multitude of topics that require urgent attention right here, on Earth. But spacecraft have become indispensable to our daily lives, in both direct and more subtle, but equally impactful ways. As technology has permeated our day-to-day routine, we have become unwittingly dependent on constellations of satellites for basic services such as communications and navigation. There are generations that do not know a world without fingertip Internet access, and Global Positioning System (GPS) navigation has all but rendered maps obsolete. Expanding our perspective beyond the individual, the same key applications in communication and navigation systems have forever changed transportation, the economy, as well as national defense.

Further increasing the level of abstraction, one begins to wonder about possible threats coming from space, such as asteroids or comets and this is the focus of planetary defense initiatives which rely on both observation and possible deflection using space-based assets. Further exploration of the universe both helps expand our knowledge and understanding of the world we live in, and gives us a better chance of preserving it. While learning more, we also begin to ponder the possibility of expand-

ing human presence to the stars.

In summary, spacecraft are critical to the continuation of our standard of life, our modern society and perhaps our species. Specific missions may affect us everyday with a relatively small apparent impact (such as being able to check our email on our phone), or perhaps once in a lifetime, but with a massive impact (like deflecting an Earth-bound asteroid). However, the one common denominator for this broad range of applications is the propulsion system. The work described in this dissertation is focused on in-space propulsion and the particular device of interest is the Hall effect thruster. A broad introduction to in-space propulsion systems is next presented in Section 1.2, then a focused description of Hall thrusters is given in Section 1.3, and finally, the research objectives are presented in Section 1.4.

1.2   In-Space Propulsion Systems

The purpose of an in-space propulsion system is to move a spacecraft from one point in space to another. The governing equation relating the spacecraft motion and fuel consumption is next derived from fundamental principles. We start with Newton's second law which states that the sum of external forces exerted on a body must equal the rate of change of momentum (Eq. 1.1):

$$\vec{F}_{ext} = \frac{d\vec{p}}{dt} \tag{1.1}$$

where $\vec{F}_{ext}$ is the summation of external forces acting on the body, $\vec{p}$ is the momentum of the body, and t is time. Now consider that our body of interest is a powered spacecraft located in an area of the cosmos where gravity and friction forces are negligible. This allows us to assume that $\vec{F}_{ext} = 0$. At any point in time we may define the instantaneous values of mass and velocity for the spacecraft: m and $\vec{v}$. Note that the

2

mass decreases in time, as propellant is exhausted. To keep our illustrative scenario simple, we assume that the propellant mass flow rate and velocity are constant: $\dot{m}$ and $\vec{u}_e$. Additionally, assume the exhaust velocity is uniform. We may thus rewrite Eq. 1.1 in scalar form, considering that the exhaust velocity and the spacecraft velocity have opposite directions:

$$0 = m\frac{dv}{dt} - \dot{m}u_e \tag{1.2}$$

Integrating Eq. 1.2 between an initial (t_i) and final (t_f) time we find:

$$m_f = m_i e^{\left(-\frac{\Delta v}{u_e}\right)} \tag{1.3}$$

where $\Delta v = v_f - v_i$ is the velocity change required for the spacecraft maneuver that we are considering. We next introduce the spacecraft specific impulse, I_{sp}, and rewrite Eq. 1.3:

$$I_{sp} = \frac{F_{th}}{\dot{m}g} \tag{1.4}$$

$$\frac{m_f}{m_i} = e^{\left(-\frac{\Delta v}{gI_{sp}}\right)} \tag{1.5}$$

where F_{th} is the magnitude of the thrust and g is the gravitational acceleration value at sea level on Earth. Equation 1.5 is also known as the rocket equation. It suggests that for a maneuver that requires a large velocity change, unless the specific impulse is equally large, a significant fraction of the initial mass will be used to carry propellant instead of payload. Therefore, specific impulse is a good measure of how efficiently we can perform a maneuver while maximizing the payload mass.

Note that escaping the Earth's gravitational pull and reaching orbit requires significant amounts of thrust and this requirement surpasses the need for high I_{sp} in space lift systems. However, once in space, the specific impulse considerations may become

equally important. Figure 1.1 illustrates how a vast array of both Earth-to-orbit and in-space propulsion technologies compare to each other in terms of thrust and specific impulse. Note how chemical propulsion systems are located almost exclusively in the low specific impulse but high thrust region, while the electric propulsion category extends in the high specific impulse region, while providing low levels of thrust.
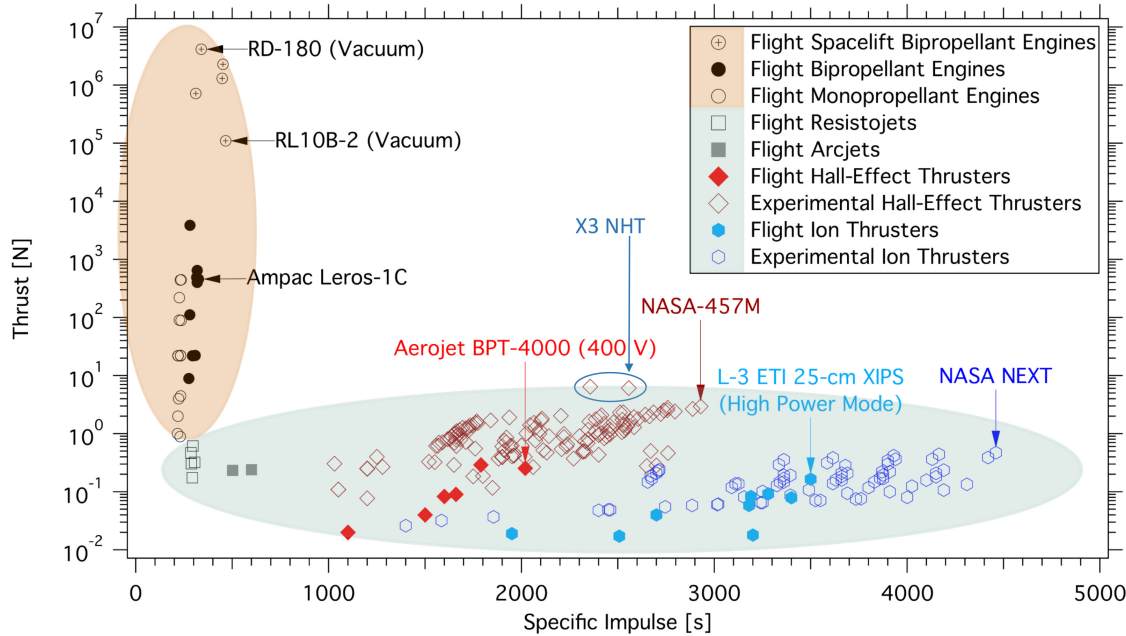
Figure 1.1: Thrust versus specific impulse for a wide range of propulsion technologies. Chemical propulsion systems are highlighted with an orange background, while electric propulsion thrusters are highlighted with a green background. Reproduced and modified with permission from [32].

Electric propulsion devices are typically grouped into three major categories:

1. Electrothermal: while the propellant gas is heated electrically, it is accelerated by the traditional mechanism of thermal expansion through a converging-diverging nozzle. Examples include resistojets and arcjets.

2. Electrostatic: the propellant gas is first ionized and then accelerated electrostatically by an applied electric field. Examples include the gridded ion thruster and the Hall Effect Thruster (HET).

4

3. Electromagnetic: the propellant gas is ionized and accelerated by interactions between electric and magnetic fields. Examples include: magnetoplasmadynamic thrusters, pulsed inductive thrusters, pulsed plasma thrusters, ambipolar thrusters and helicon thrusters.

Hall thrusters constitute the focus of this work, and they will next be described in more detail in Section 1.3. However, it is first important to highlight some of their advantages compared to other propulsion systems, in addition to the relatively high value of specific impulse. When compared to gridded ion thrusters, HETs have a smaller footprint for the same power level, they are simpler to integrate on spacecraft as they require fewer power supplies [29], and provide a greater ratio of thrust to input power. Moreover, they have a well established flight heritage, with roughly a hundred being flown by the former Soviet Union on satellites between 1972 and 1991 [106] to aid in stationkeeping. In addition, HETs have also been used for primary propulsion by the European Space Agency (ESA) Small Missions for Advanced Research in Technology (SMART)-1 technology demonstration mission, launched in 2003 that was successfully completed in 2006 [80]. Finally, in 2011 the US Air Force satellite Advanced Extremely High Frequency (AEHF)-1 suffered a catastrophic loss of its chemical primary propulsion system. However, it was equipped with Hall thrusters for stationkeeping, which were successfully used to bring the satellite from its initial low transfer orbit to its final destination in a geosynchronous orbit [82]. Finally, a recent reliability study [88] that considered field anomalies and failures from orbiting satellites has found that Hall thrusters have "robustly outperformed chemical propulsion" options, and also proved to be more reliable than gridded ion thrusters.

1.3   Hall Effect Thrusters

Hall effect thruster are gridless electrostatic devices used for in-space propulsion. While magnetic fields are necessary for HET operation, the two fields are generated independently of eachother, and thrust is not produced via $\vec{E} \times \vec{B}$ acceleration of the ions, hence these thrusters are not characterized as "electromagnetic". A typical configuration for a state-of-the-art Hall thruster is shown in Figure 1.2. It consists of an annular discharge channel whose walls are made of a dielectric material with a low sputter yield (such as boron nitride), an anode which also serves as a propellant injector, and a hollow cathode which may be located at the center of the thruster, or externally mounted. The thrusters presented in the current work all have centrally mounted cathodes, with the exception of the Russian designed SPT. The propellant gas is typically chosen to be non-reactive, with a large molecular weight and a low ionization potential. Noble gases such as xenon and krypton are thus ideal choices.

1.3.1   Hall Effect Thruster Operation Principles

The anode is typically biased to a positive potential value of several hundred volts, while the cathode voltage is negative, and on the order of tens of volts. This potential difference gives rise to an axial electric field, E_z, as seen in Fig. 1.2(a). The radial magnetic field, B_r, is generated by electromagnets located in the thruster walls. As the cathode is heated and ignited, it begins to thermionically emit electrons, some of which enter the thruster channel. The magnetic field impedes their motion towards the anode. They become trapped in an $\vec{E} \times \vec{B}$ drift, as shown in Fig. 1.2(b). This is the Hall current from which the device derives its name. Next, the propellant gas is introduced at the anode injector, and as the neutral atoms travel through the channel they collide with the trapped electrons. Ions are born through electron-impact ionization. Due to the choice of magnitude for the magnetic field (several hundred

6

Gauss), while the electrons remain trapped in the azimuthal drift, while ions proceed through the channel unimpeded, and are accelerated by the axial electric field. The above was a simplified explanation of the operating principles of a Hall thruster. For a more detailed description, the reader is encouraged to seek reference [29].

(a) Axial-radial view (r-z).   (b) Azimuthal view (r-θ).
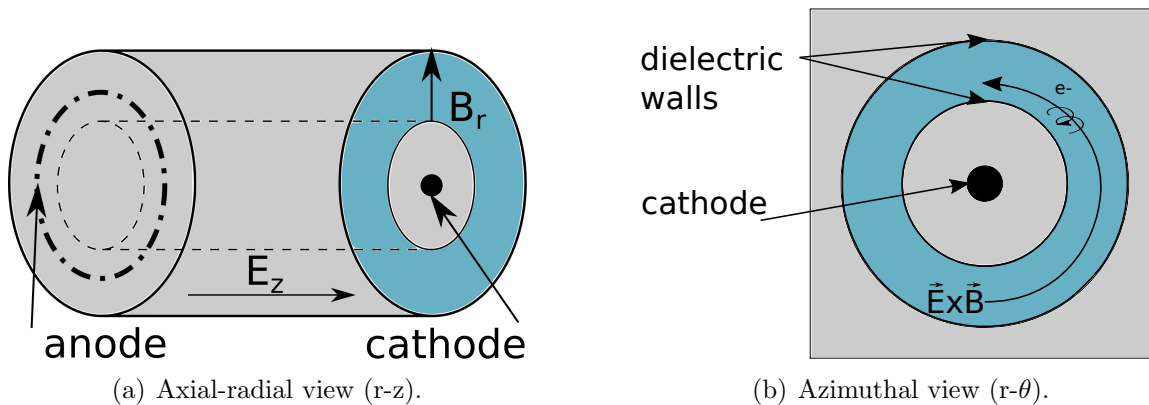
Figure 1.2: Description of Hall thruster operation. Not drawn to scale.

1.3.2 High Power Hall Effect Thrusters

Hall thrusters have been in development and use for more than 60 years, and due to their low thrust but high efficiency, they have typically been used on spacecraft for stationkeeping or orbit-raising, while several missions have even used HETs for primary propulsion (Section 1.2). However, starting in 1999 there has been a push for higher power devices. The NASA Glenn Research Center (GRC) has led this effort which produced a series of 20-50 kW class HETs. First, the 50 kW class NASA-457Mv1 thruster was tested with both xenon and krypton propellant. When operating with xenon, it reached a maximum total power of 97 kW, maximum discharge current of 112 A, maximum total efficiency of 58%, and specific impulse values in the range of 1550-3560 seconds [48, 62, 61]. This initial work provided physical insight and demonstrated scaling techniques that were next implemented in an optimized version of the thruster, the NASA-457Mv2 [94]. It showed improved performance over the

first iteration, however this thruster was not tested beyond 50 kW. Further, using the same scaling concepts, the NASA-300M and NASA-400M thrusters were developed. The NASA-300M 20-kW class thruster showed a peak total efficiency of 67% at the 500 V and 40 A operating point with xenon [51], which is also studied in the current work in Section 3.3. The NASA-400M generated a peak anode specific impulse of 4940 seconds with krypton propellant, at 40 kW discharge power [79]. Looking beyond thruster development, and considering applications, the proposed Asteroid Redirect Mission[8]) planned to utilize a state-of-the-art Hall thruster to reach an asteroid and return that asteroid to translunar orbit. However, while that project was eventually cancelled, the 12.5 kW resulting power and propulsion unit has been re-purposed for use in the newly proposed Deep Space Gateway concept [37, 26]. The mission is to demonstrate exploration system capabilities in cislunar space, with a final goal of reaching for Mars and beyond.

1.3.3   Nested Channel Hall Effect Thrusters

A promising approach to use Hall thrusters for primary propulsion while minimizing the footprint on the spacecraft is to nest multiple channels. This concept is demonstrated by the 10 kW class dual channel Nested Hall Effect Thruster (NHT), dubbed "X2", developed at the PEPL at the University of Michigan. The channels can operate independently or together, increasing the throttling range for the device. Moreover, Liang [58] observed additional thrust gains due to the channel interaction. Specifically, while keeping a constant flow rate, a thrust increase between 4% and 9% (depending on the propellant mass flow rate) was recorded for dual channel operation when compared to the sum of thrust values from individual single channel tests, as demonstrated in Fig. 1.3. Figure 1.4(a) shows the X2 thruster operating in dual channel mode with xenon propellant in the laboratory. Alongside it, Fig. 1.4(b)

8

shows a schematic of the thruster along with magnetic field lines (reproduced from [58]). This thruster will be later simulated in Sections 5.2 and 5.3.
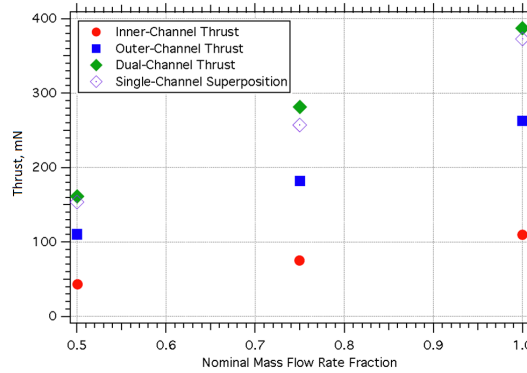
Figure 1.3: Thrust gains observed for the X2 in dual-channel operation versus super-position of single channel values [58].
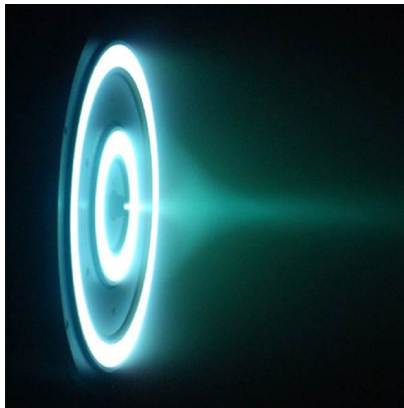
(a) Dual channel mode operation [58].
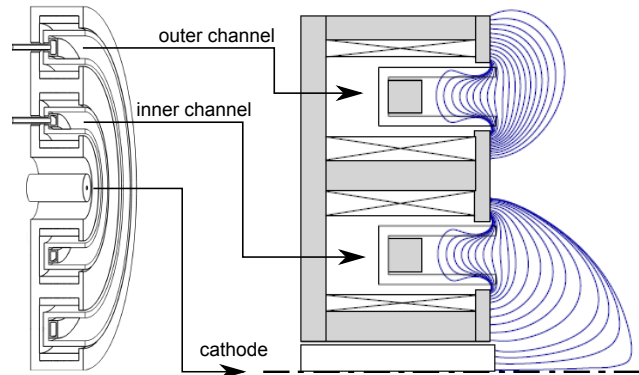
(b) Axisymmetric simulation setup. Magnetic field is shown with blue lines. Fig. 5.6(a) shows the computational mesh.

Figure 1.4: X2 thruster in the laboratory, and simulation.

Further work by Florenz [25] has led to the development of a three-channel 100-kW class NHT with three discharge channels: the X3 thruster. Recent work by Hall [32] has contributed to the characterization of the X3, and brought the state-of-the art NHT into the thousand mN regime, as shown in Fig. 1.1. While these exciting developments pave the way for future high-power Hall thruster research, the current work will only focus on the simpler two-channel NHT.

1.4 Research Objectives

In order to qualify a thruster for flight, rigorous ground testing must be performed, and this is often expensive and time consuming. Moreover, facility effects [11] may influence the measurements and give unrealistic expectations compared to real performance in space. Therefore, computer simulations and analytical models provide valuable insight into the development and performance of HETs while also helping reduce costs.

This work is focused both on improving the state-of-the-art in the field of numerical simulation, and investigating several physical processes of interest in the Hall thruster community. We start by introducing the reader to the state-of-the-art numerical simulation methods in Chapter II. When considering the recent developments in the field of high-power Hall thrusters, several problems become apparent. First, propellant cost, which is addressed through a study of an alternative and less expensive option in Chapter III. Next, the problem of discharge channel erosion is investigated in Chapter IV. Further, two approaches are used to analyze NHT operation in Chapter V. It is determined that improved modeling capabilities are required, and the development of a new Cartesian 2D axisymmetric electron fluid model is presented in Chapter VI. Finally, conclusions and future work are listed in Chapter VII.

CHAPTER II

Existing Computational Models

Several computational models are used throughout this work, and this section provides background on each of them. We start with the multi-fluid Hall thruster simulation framework Hall2De, which is briefly described in Section 2.1. Next, the direct simulation Monte Carlo method implementation, Monaco, is discussed in Section 2.2. Finally, the hybrid-particle-in-cell (hybrid-PIC) HET simulation framework with quasi-1D electrons, HPHall, is introduced in Section 2.3.

2.1 Multi-Fluid Model

The simulation framework Hall2De [53, 64, 76] has been developed at the Jet Propulsion Laboratory over the past decade for the purpose of studying HETs. The computational grid is aligned with the magnetic field, and a typical domain includes both the thruster channel and a plume that extends several channel lengths downstream. The model is axisymmetric, with the radial zero coordinate located at the thruster centerline.

Different models are used for each of the plasma species: neutrals, ions and electrons. Under the assumption of free molecular flow, the neutral particle density and velocity distributions are computed with a view-factor algorithm [53]. A hydrodynamic

approach is used to model the ions, and they are divided into multiple populations, based on energy. The ions generated upstream of the acceleration region are part of the high energy population, while the ions generated downstream form the low energy population. Thus, in most cases the HET physics can be modeled with two populations of ions. In addition to solving separate continuity and momentum equations for each population, each charge state is also resolved independently. The different energy populations and charge states interact with each other through ionization, charge exchange and elastic collisions. Finally, the electrons are modeled using a fluid approach. The Generalized Ohm's law in vector form in the directions parallel and perpendicular to the magnetic field lines, coupled with charge conservation and plasma quasi-neutrality yield the plasma potential, while the electron temperature is computed from an energy conservation equation.

2.2   Direct Simulation Monte Carlo

The mass, momentum and energy equations characterizing a gas flow may be determined either from a macroscopic or molecular description. Since the Velocity Distribution Function (VDF) is not always known, the set of equations is not closed until one defines the shear stresses and heat fluxes in the flow. Thus under certain conditions a macroscopic description becomes invalid. This situation concerns non-equilibrium gases, where the length scales that describe the transport terms in the Navier-Stokes equations are on the same order as the gas mean free path, the mean distance travelled by the gas particles between collisions. Recognizing that a molecular description is necessary to resolve the gas behavior leads to a discrete rather than continuum approach to modeling. A brief introduction to rarefied gases and kinetic theory is provided next, but for a more comprehensive treatment of these topics the reader is encouraged to seek references [6] and [4].

The discussion on kinetic theory begins with a classification of gas flows based on the level of interaction between molecules. A dimensionless parameter may be constructed from the ratio of the mean-free-path and a length scale that is relevant to the flow, as shown in Eq. 2.1. This is the Knudsen number (named after Danish physicist Martin Knudsen, 1871-1949), and may be used to provide a roadmap of mathematical model validity for various flow regimes, as illustrated in Fig. 2.1.

$$Kn = \frac{\lambda}{L} \tag{2.1}$$

where λ is the mean-free-path, and L is a relevant flow scale. One way to compute L is to consider the length scale associated with a spatial gradient from the flow, for example a temperature gradient, dT/dy. We can thus write: $L = \frac{T}{dT/dy}$, where y is the normal position coordinate, and T is temperature.
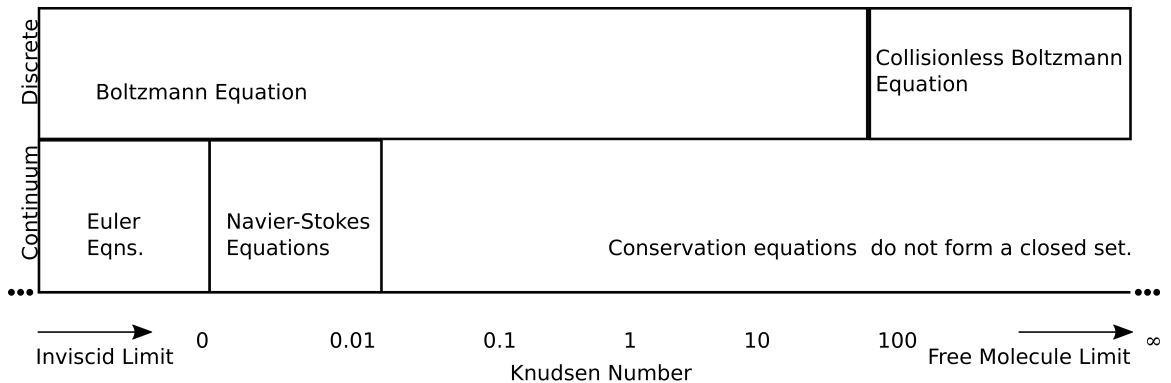
Figure 2.1: Mathematical model applicability for various flow regimes based on Knudsen number[4].

The governing equation that describes gas behavior for a dilute gas at a molecular level is Boltzmann's equation (Eq. 2.2). The dilute gas assumption is in place to allow only for two-body, binary collisions.

13

$$\frac{\partial(nf)}{\partial t} + \vec{C} \cdot \frac{\partial(nf)}{\partial \vec{r}} + \vec{a} \cdot \frac{\partial(nf)}{\partial \vec{C}}$$

$$= \int_{-\infty}^{\infty} \int_{0}^{4\pi} n^2 \left\{ f\left(\vec{C}'\right) f\left(\vec{Z}'\right) - f\left(\vec{C}\right) f\left(\vec{Z}\right) \right\} g \sigma d\Omega d\vec{Z} \qquad (2.2)$$

Here f is the *velocity distribution function*, n is the number density, $\vec{r}$ is the particle position and $\vec{a}$ is the particle acceleration caused by an external force. $\vec{C}$ is the particle velocity, $\vec{Z}$ is the collision partner particle velocity, and the same symbols primed represent the post-collision particle velocities. The *total collision cross-section* is given by $\sigma_T = \int_{0}^{4\pi} \sigma d\Omega$. Note that g is a scalar quantity historically referred to as the *relative velocity*, and Ω is the solid anglef.

Solving this integro-differential equation analytically is possible only for certain special cases. One approach is to use *moment methods*, which requires taking the moment, $\bar{Q}$ of the Boltzmann equation with respect to a quantity Q, as described in Eq. 2.3.

$$\bar{Q} = \int_{-\infty}^{\infty} Q f dc \qquad (2.3)$$

By taking the moment of the Boltzmann equation, one arrives at the Equation of Change (Eq. 2.4). Here, the presence of the $\overline{\vec{C}Q}$ term suggests that each additional integration will lead to an equation containing an even higher order moment therefore creating a closure problem. However, by assuming that the VDF contains a finite set of macroscopic quantities or moments, the system may be closed.

$$\frac{\partial}{\partial t}(n\bar{Q}) + \nabla \cdot (n \cdot \overline{\vec{C}Q}) - n\vec{F} \cdot \frac{\partial Q}{\partial \vec{C}} = \Delta[\dot{Q}] \qquad (2.4)$$

where $\Delta[\dot{Q}]$ is the rate of change of property Q due to intermolecular collisions.

Assuming that the gas is in a state of local thermal equilibrium everywhere implies that the VDF is Maxwellian. To maintain the VDFs in equilibrium it must be that $Kn \to 0$, which in turn gives molecular transport coefficients that are zero. Finally, taking moments of the Boltzmann equation for mass, momentum and energy yields the Euler inviscid equations.

The Chapmann-Enskog [12] approach assumes a form of the VDF based on a Maxwellian with a small perturbation. By expanding the VDF it is possible to obtain closure by determining the shear stress and heat transfer coefficients. After applying a similar process as in the previous paragraph, but also including higher order moments, the Chapmann-Enskog solution produces the Navier-Stokes equations, for a regime of $Kn < 10^{-2}$.

The *model equation* approach is another analytic attempt to solve the Boltzmann equation. It involves assuming a form for the collision terms and a well-known example is the BGK equation, named after Bhatnagar, Gross and Krook [3].

While the discrete nature of the gas molecules makes the analytic solution of the Boltzmann equation difficult, it provides inspiration to approach the problem numerically. Thus, the idea of a direct physical simulation is born. This is different than a typical Computational Fluid Dynamics (CFD) calculation, where one solves an established set of mathematical equations that are expected to characterize the flow of interest. Direct physical simulation reproduces the physical behavior of the

gas at the molecular level and collects the macroscopic results using statistical methods. The implementation of boundary conditions which can become very complex in CFD simulations is greatly simplified here, and also there is no need to provide any information about the initial flow field [4]. On a more fundamental level, CFD solutions inherently assume an underlying Maxwellian VDF, whereas Direct Simulation Monte Carlo (DSMC) does not include any such assumptions and can thus capture non-Maxwellian distributions which characterize non-equilibrium effects.

In a DSMC simulation there are simulated particles which represent a large number of identical real molecules or atoms. Therefore the molecular collisions are not deterministic. However, the collisions between simulated particles are performed stochastically which allows for a sampling of all representative collision pairs within a cell, in a Monte Carlo fashion. Although the exact location of computational particles in a cell is not important, the velocity distribution function is recovered accurately, provided that the cell size is smaller than the local mean free path and the timestep is smaller than the mean collision time.

The Monaco framework is a state-of-the-art implementation of the direct simulation Monte-Carlo method[7]. It is capable of handling 2D, 2D-axisymmetric and 3D domains. The computational mesh is composed of triangles (for 2D) or tetrahedra (for 3D). Furthermore, the program may be run in either serial or parallel, allowing for very efficient large simulations[17]. Several types of boundary conditions are available in Monaco:

- **diffuse wall**: particles interact with the wall and reflect (or stick) based on the specifications; thermal accommodation may also be specified

- **inflow**: particles are introduced with specified velocity components, and the user selects the number density at the injection surface

- **sputtering wall**: a combination of inflow and diffuse wall; particles impacting the wall interact as in the diffuse wall boundary, while sputtered particles are introduced as through an inflow condition with the additional benefit of allowing the user to specify a custom (non-Maxwellian) VDF

- **outflow**: particles are free to exit the simulation domain

- **symmetry line**: particles are reflected or rotated

2.3 Hybrid Particle-in-Cell

As discussed in the previous chapter, particle methods are ideal for simulating the physical behavior of molecules, while introducing a minimum number of assumptions. However, there are cases when particle methods may become too expensive for an engineering application to be feasible. One such scenario occurs with the plasma of Hall thrusters. Assuming a uniform three dimensional mesh, and a serial (single-processor) implementation, a full-PIC simulation is expected to take several hundreds of thousands of years with a state-of-the-art processor, and several hundreds of TB of memory available (see Appendix A). A full-PIC 3D simulation was generated by Passaro et. al [78], by employing a multi-block grid and parallel algorithms for the Poisson solver, however total walltime or memory usage was not reported.

The difficulty here arises if one tries to model all the species (neutrals, ions and electrons) as particles, due to the large difference in mass between the heavier species, and the electrons. However, this also provides an opportunity to separate the longer time scale (ions and neutrals) from the faster electron motion. Due to the de-coupling of the electron motion, a hybrid approach may be used where we model the electrons with a different technique than the heavy species.

The familiar axisymmetric, hybrid-PIC simulation framework HPHall was developed by Fife[24] at MIT in 1998 to study Hall effect thrusters. The code treats heavy species such as ions and neutrals as particles. Their behavior is resolved using a PIC method which is explained in Section 2.3.1. The electrons are modeled as a fluid continuum (Section 2.3.2) in order to reduce computational cost. The latest version of HPHall [42, 27, 43, 41, 93] is used in Section 5.3 to help characterize the X2 thruster inner channel operation.
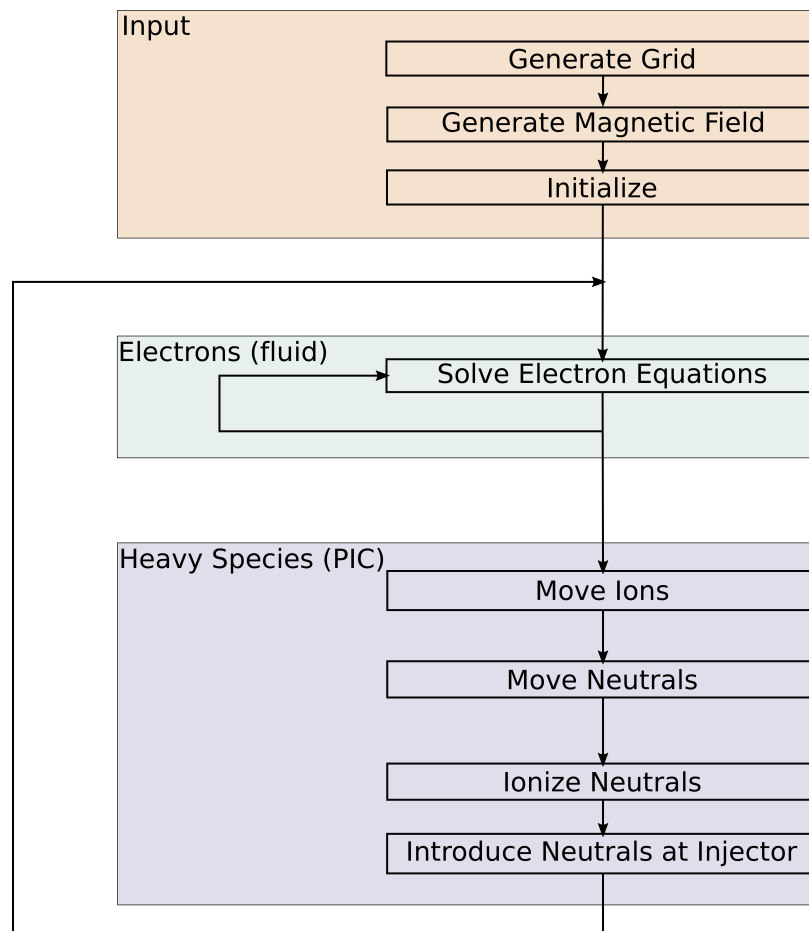
Figure 2.2: A typical hybrid-PIC simulation cycle [24].

A typical HPHall simulation cycle is shown in Fig. 2.2. One starts with the input stage, where the magnetic field and mesh are generated. Then initial values are used to initialize the plasma solver. First the electron algorithm is run, in order to com-

pute the plasma potential and the electron temperature. This is repeated until the desired number of electron timesteps is reached, and then the information is passed to the PIC algorithm, which handles the heavy species movement. Next, the ionization and neutral injection take place, and the computational cycle returns to the electron module with updated values of the plasma density, neutral density and the ion current. This second iteration process takes place at the heavy species timestep, which is larger than that used for electrons. This larger loop gives the amount of physical time that we are simulating. Once we reach the final simulation time, the time-averaged results and performance parameters of the thruster are output.

2.3.1 Particle-in-Cell
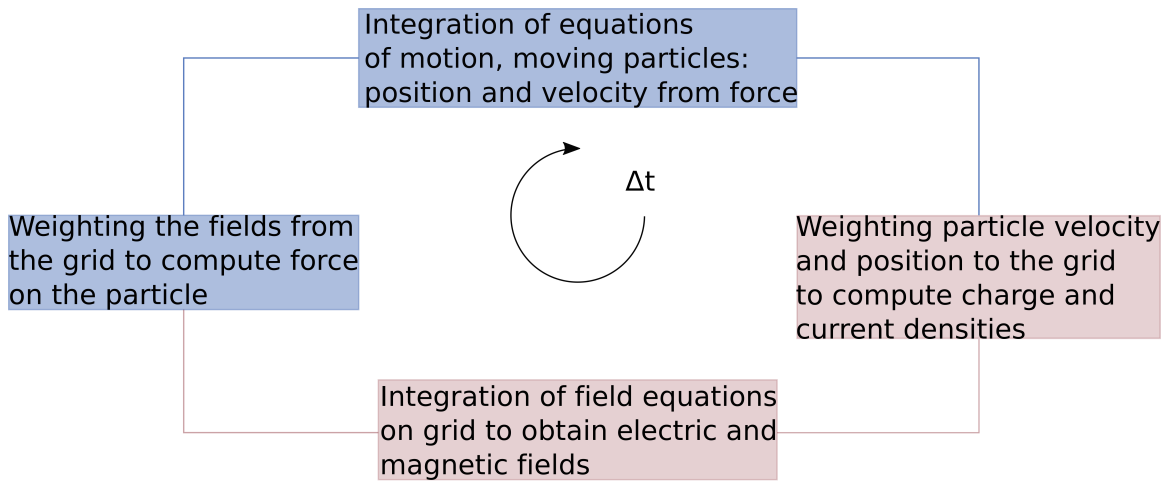
Figure 2.3: A typical particle-in-cell simulation cycle. Particle-related steps are shown in blue, while grid-related steps are in red.

Particle-in-Cell (PIC) methods attempt to model charged particles that are moving in space due to both self-generated forces, and due to applied fields. Both fields produced by the particles, and the particle motion which results form the applied forces must be accounted for. By knowing the positions and velocities of all the particles, one may compute the fields produced by the particles by using Maxwell's

equations. Then one uses the Newton-Lorentz equations of motion to compute the forces acting on the particles from the electric and magnetic fields. The fields are computed from the initial charge and current densities, then the particles are moved, and the fields are re-calculated based on the new particle positions and velocities. This is an iterative process which is repeated for multiple steps in time. The process is illustrated in Fig. 2.3.

The PIC algorithm uses a spatial grid on which the electric and magnetic fields are computed. However, the position and velocity of a particle may take on continuous values in phase space. Hence to exchange information between phase space and the spatial grid, a process of weighting is employed in both directions. The diagram in Fig. 2.3 shows the particle-related computational steps in blue, while highlighting grid-related calculations in red.

Additional details, along with an example of a simple PIC code are provided by Birdsall and Langdon in [5].

2.3.2 Quasi-1D fluid

In an effort to simplify the description of HET physics, Morozov [71] introduced the "thermalized potential" approximation, which is equivalent to assuming that electrons are isothermal along the magnetic field lines. This was justified by the observation that in Hall thrusters the electron mobility is much larger for transport along the magnetic field lines rather than across them.

While the assumption of azimuthal symmetry leads to an axisymmetric formulation, the added simplification of isothermal field lines further reduces the dimensionality of

the electron conservation equations to a quasi-1D form. We first define the magnetic field line coordinates, and then write the conservation equations for electrons along and across lines of force. Further details may be found in Fife's original description [24].

From Maxwell's equations $\nabla \cdot \vec{B} = 0$ and therefore a magnetic stream function, λ, can be defined:

$$\frac{\partial \lambda}{\partial z} = rB_r$$
$$\frac{\partial \lambda}{\partial r} = -rB_z \tag{2.5}$$

The electron equations along lines of force, as implemented in HPHall [24] are:

$$\phi - \frac{kT_e}{e} \ln n_e = \phi^*(\lambda) \tag{2.6}$$

$$T_e = T_e(\lambda) \tag{2.7}$$

where ϕ is the plasma potential, k is Boltzmann's constant, T_e is the electron temperature in K, e is the elementary charge, n_e is the electron number density and ϕ^* is a constant along each line of force.

Across lines of force:

$$u_{e,\hat{n}} = \mu_{e,\perp} \left\{ -rB\frac{\partial \phi^*}{\partial \lambda} - rB\frac{k}{e} \left[\ln(n_e) - 1\right] \frac{\partial T_e}{\partial \lambda} \right\} \tag{2.8}$$

$$\frac{\partial \phi^*}{\partial \lambda} = \frac{-I_a + I_w - 2\pi k \frac{\partial T_e}{\partial \lambda} \int_0^l n_e \mu_{e,\perp} B(\ln(n_e) - 1) r^2 ds - 2\pi e \int_0^1 n_i u_{i,\hat{n}} r ds}{2\pi e \int_0^l n_e \mu_{e,\perp} B r^2 ds} \tag{2.9}$$

$$S_h - S_i = \frac{\partial}{\partial t}\left(\frac{3}{2} n_e k T_e\right) + \nabla \cdot \left(\frac{5}{2} n_e k T_e \vec{u}_e + \vec{q}_e\right) \tag{2.10}$$

$$S_h = \vec{j}_e \cdot \vec{E} \tag{2.11}$$

$$S_i = \dot{n}_e \varphi' E_i \tag{2.12}$$

where $u_{e,\hat{n}}$ is the electron velocity in the direction normal to the field lines, I_a is the number of electrons emitted at the cathode, I_w is the total near-wall current, $u_{i,\hat{n}}$ is the ion velocity in the direction normal to the field lines, S_h is the Joule heating term, S_i is the inelastic loss term, and φ' is the normalized ion production cost. $\mu_{e,\perp}$ is the effective electron mobility across field lines, and is defined in Section 5.3.1.2, where the electron transport model is explained in detail.

A detailed analysis of wall effects by Fife [24] considers the energy loss to the wall and sheath. Upon integration of the primary and secondary electron energy fluxes across Maxwellian distributions, the following expression for the wall heat flux is obtained:

$$\frac{q_w}{\vec{\Gamma}_e} \approx \begin{cases} \exp\frac{e\phi_w}{kT_e} \left[2k\left(T_e - \delta_{eff} T_{sec}\right) - (1 - \delta_{eff}) e\phi_w\right], & T_e < 16.5 \text{ eV} \\ 2k\left(T_e - T_{sec}\right), & T_e < 16.5 \text{ eV} \end{cases} \tag{2.13}$$

The total near-wall current is used in the electron continuity equation (Eq. 2.9) instead of accounting for localized effects. This current is computed as follows:

$$I_w = e\Gamma_e \delta_{eff}\left(\frac{2\pi\Delta z}{\sin(\theta)}\right) = \Gamma_e \delta_{eff}\left(\frac{2\pi r E m_e}{B^2 \sin(\theta)}\right) \tag{2.14}$$

22

where q_w is the net energy flux to the wall, Γ_e is the electron flux, ϕ_w is the wall potential, δ_{eff} is the effective secondary emission coefficient, T_{sec} is the temperature of the secondary electrons and θ is the angle between the direction perpendicular to the wall, and the direction of the magnetic field at the wall.

The cathode is modeled as a perfect current source, and the boundary conditions for both plasma potential and electron temperature are fixed (Dirichlet). However, the anode plasma potential is computed from the expression of the anode sheath potential drop, as follows:

$$\phi_{anode} = -\frac{kT_e}{e} \ln \left[\frac{I_a}{Aen_e \sqrt{\frac{kT_e}{2\pi m_e}}} + e^{-\frac{1}{2}} \sqrt{\frac{2\pi m_e}{m_i}} \right] \tag{2.15}$$

$$\phi_{cathode} = \text{constant} \tag{2.16}$$

$$T_{e,cathode} = \text{constant} \tag{2.17}$$

where A is the anode surface area.

2.4 Applications

All three of the computational models presented above are applied in this work to the study of Hall thrusters.

The full-fluid Hall2De simulation is employed in Chapter III to study the expected performance of two different HETs operating with krypton propellant: the H6US and the NASA-300M. Krypton propellant is implemented as a new species in the code.

The direct simulation Monte Carlo method is used in Chapter IV to model thruster

channel erosion for an SPT-70 device. A sputtering wall boundary conditions is implemented. DSMC is later also applied in Section 5.2 to study the neutrally charged species pressure distributions and number densities for the X2 NHT operating in dual-channel mode.

Finally, the hybrid-PIC framework HPHall is used to characterize the independent operation of the X2 NHT inner channel in Section 5.3. In addition, a significant code development effort is presented for the 2D-axisymmetric standalone electron model (Chapter VI), which is also implemented within the existing HPHall framework.

CHAPTER III

Evaluation of Alternative Propellant

3.1 Motivation

The traditional choice of propellant for Hall thrusters has been xenon. However, several studies have considered the use of krypton as an alternative [60, 59, 73]. Both gases are non-reactive, and xenon has certain advantages, such as a lower ionization potential and a higher atomic weight. Thus less energy is needed to ionize xenon than krypton, and since the particle is more massive, the thrust value is expected to be higher. However, using krypton can significantly lower the costs of testing: as of April 2018, xenon gas was approximately 9 times more expensive than krypton.

Although most simulation work has focused on xenon propellant thrusters, there have been previous efforts to evaluate the use of krypton gas. In 2001 Garrigues [28] used a 1D hybrid model to investigate thruster performance of the SPT-100 with krypton gas, and found that for the same voltage and mass flow rate similar values of thrust may be obtained between xenon and krypton, but a lower efficiency is observed for krypton gas (30% versus 40% for xenon). In 2008 Yim [103] applied a 2D hydrodynamic model to study krypton operation of the NASA-173Mv1 HET. However the model did not capture the peaks of electric field and electron temperature accurately since the thermal conductivity term in the electron energy conservation equation was

neglected. Both previous efforts focused only on the thruster channel. The present work is the first attempt to simulate both thruster and plume with krypton propellant using a 2D axisymmetric model and validate the results with experimental measurements.

Several updates are made to include krypton as a propellant into the fluid model Hall2De which was introduced in Section 2.1. These updates are presented in Section 3.2. The NASA-300M thruster (Section 3.3) is used for assessment of simulation accuracy by comparison with experimental data. The simulation setup is explained in Section 3.3.1, while the results are shown in Section 3.3.3. The H6US thruster is simulated (Section 3.4) both with xenon and krypton, with the setup described in Section 3.4.1 and results in Section 3.4.2. Finally, a summary is presented in Section 3.5.

3.2   Hall2De Updates

In order to include krypton propellant in the simulation, several updates are implemented [23], related to the properties of the new propellant gas. The ionization cross-sections of krypton affect the ionization rate which results in different densities of neutral and charged species than in the xenon case. Further, the ionization potential plays a direct role in the electron energy equation, by changing the electron energy losses.

Table 3.1 provides a comparison of the atom mass and the ionization threshold energies [55] for krypton, compared to xenon. While the krypton mass is 64% that of xenon, the ionization potential for krypton is consistently higher than for xenon, for up to the fourth charge state.

26

Table 3.1: Propellant gas properties [55].

	Xe	Kr	% Kr/Xe
Mass (a.m.u.)	131.3	83.8	63.8
Ionization potential 1 (eV)	12.1	14.0	115.7
Ionization potential 2 (eV)	12.1+21.2	14.0+24.4	115.3
Ionization potential 3 (eV)	12.1+21.2+31.1	14.0+24.4+35.8	115.2
Ionization potential 4 (eV)	12.1+21.2+31.1+50.0	14.0+24.4+35.8+50.9	109.4

Energy loss mechanisms are implemented through the introduction of a collision cross-section corresponding to each process. Elastic scattering cross-sections are presented in Section 3.2.1 for krypton, and compared to the existing implementation of xenon cross-sections used in Hall2De. The krypton values are consistently lower, with a maximum difference of 42% lower than the xenon values. Electron-impact ionization processes are also considered, and the cross sections are shown in Section 3.2.2. Krypton cross-sections are lower than those of xenon for all ionization processes, and the maximum percent difference for each process is presented in Section 3.2.2. Charge Exchange (CEX) cross-sections are discussed in Section 3.2.3, and in this case the values reported for krypton are only at most 11% lower than those for xenon. We note that the CEX and elastic scattering cross-sections are 10 to 100 times larger than the ionization cross-sections, depending on the ionization process. For all processes considered, the xenon cross-sections are larger than for krypton at a given energy, and this increases the probability of each process occurring. However, considering results from kinetic theory [6], we recall that the collision event probability is also proportional to the mean relative velocity between particles (Eq. 3.1).

$$\text{collision probability} \propto \sigma g \tag{3.1}$$

where σ is the collision cross-section and g is the relative velocity of two colliding particles. As shown in Eq. 3.2 for the case of a simple gas with identical particles involved in collisions, the mean relative velocity is in turn proportional to the inverse square root of the mass.

$$\langle g \rangle = 4\sqrt{\frac{kT}{\pi m}} \tag{3.2}$$

Therefore we conclude that the total collision probability must be directly proportional to the collision frequency and inversely proportional to the square root of the mass:

$$\text{collision probability} \propto \frac{\sigma}{\sqrt{m}} \tag{3.3}$$

Throughout the present work we provide explanations of various simulation results based on the differences in cross-sections, but the effect of mass is discussed as well. Since krypton atoms are lighter than those of xenon, the effect of mass is to reduce the differences in collision outcomes for the two species that would be observed based on cross-section values alone.

3.2.1 Electron Elastic Scattering

The electron elastic scattering cross-sections are plotted in Fig. 3.1 for both xenon and krypton. Data for xenon is selected from two sources: Register [83] for energies between 1 and 4 eV, and Nickel [74] for values above 4 eV. Several other authors reported consistent values of krypton elastic cross-sections, and the most recent publications are selected. Thus krypton data from Yuan [105] is used for energies between

0 and 7.5 eV, while the data reported by Wagenaar [100] is used for energies between 7.5 and 750 eV. The values for krypton are lower than for xenon throughout the entire energy range, with a maximum difference of 42%.
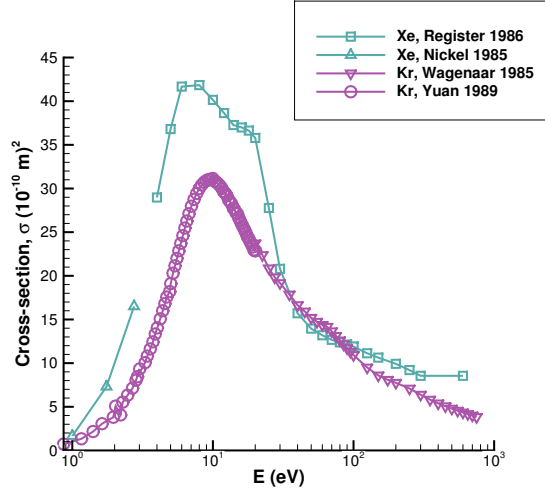
Figure 3.1: Electron elastic scattering cross-sections.

3.2.2 Electron-impact Ionization

Three charged states of the propellant gas are included in the simulation, and we consider all six ionization processes that may result in singly, doubly or triply charged ions.

The ionization cross-sections for electron impact ionization from the ground state up to the singly, doubly and triply charged states are shown in Fig. 3.2. The xenon cross-sections for all three cases are extracted from Rejoub [86]. For all three processes the cross-sections from Wetzel [102] have an uncertainty of 15%, while those reported by Rejoub [86] have an uncertainty of only 5%.

For the single ionization process, data from Wetzel [102] is used between 13 and 15

29

eV, while between 15 and 1000 eV, data from Rejoub [86] is implemented. The cross-sections for krypton are lower than for xenon, with a maximum difference of 26%. When accounting for the different mass of the two gases, the probability of single ionization for krypton is only 7.5% lower than that of xenon undergoing the same process.

For the double ionization process, between 40 and 45 eV data from Wetzel [102] is used, and from 45 to 1000 eV, the cross-section values are taken from Rejoub's work [86]. For this process the krypton cross-sections are at most 43% lower than those for xenon, however when considering the mass ratio of the gases, the ionization collision probability value for krypton is 29% lower than that of xenon.

For triple ionization from the ground state, the data from Rejoub [86] is used in the entire range (90 - 1000 eV). In this case the cross-section values for krypton are significantly smaller than for xenon, with a maximum difference of 89%. Considering the effect of mass, the triple ionization process is 86% less likely to occur for krypton than for xenon.

Next, the cross-sections for ionization of singly charged ions are shown in Fig. 3.3, while Fig. 3.4 shows the cross sections for doubly charged to triply charged ion transitions. Xenon cross-sections from Bell [2] are used for the single to double ionization process.

For krypton, only data from Tinschert [97] could be identified, so cross-sections from that source are used in all the above mentioned cases for the entire energy range presented. For low energies there are large uncertainties in the cross-section values ($\approx 100\%$), however the uncertainties reduce rapidly for higher energy collisions. For single to double ionization, the large uncertainties occur between 15 and 23 eV, for

double to triple between 21 and 23 eV, and for single to triple between 50 and 56.6 eV.

The krypton cross-sections are lower than the xenon values for all three cases. For the singly to doubly charged ionization process the maximum difference is 50%, for doubly to triply charged it is 37% and for singly to triply charged the difference is 79%. When considering the probability of these ionization events to occur (including effect of mass), the trend remains the same: for krypton the singly to doubly charged transition is 38% less likely to occur than for xenon, for doubly to triply charged it is 20% less likely to occur, and finally, for singly to triply charged it is 73% less likely to occur than for the xenon case.

3.2.3   Charge Exchange

The CEX collision process is implemented by considering a collision cross-section, as shown for the neutral - singly charged ion case in Fig. 3.5. Since the cross-sections for collisions with doubly and triply charged ions are obtained by scaling the CEX cross-sections shown in Fig. 3.5 by the charge number, they are not shown. The curve for krypton is obtained from Hause [36], and the values are consistently lower than the xenon cross-sections for the entire energy range, with a maximum difference of 11%. However, when accounting for the effects of mass on collision probability, we notice the opposite trend: the krypton collision is 10% more likely to occur.
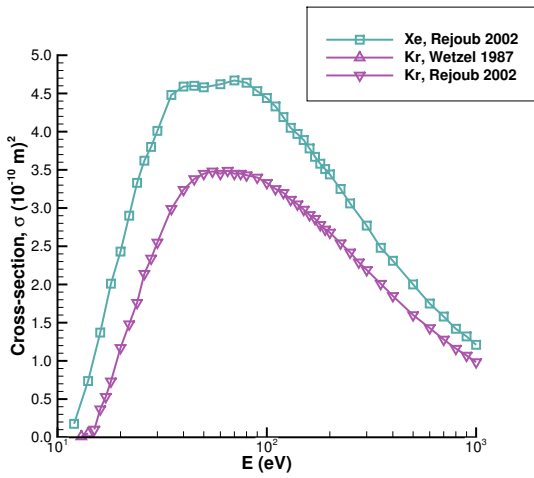
(a) Ground to singly charged.
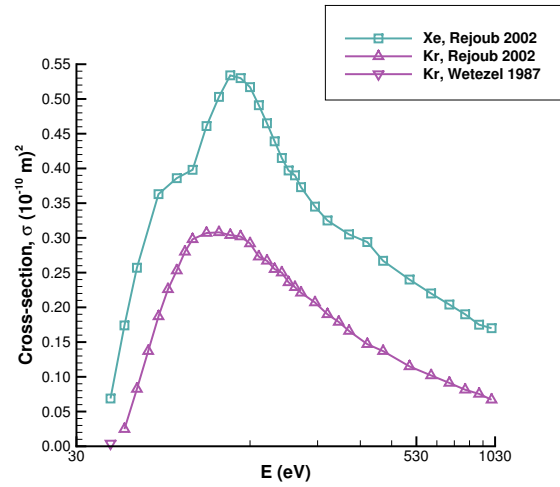
(b) Ground to doubly charged.
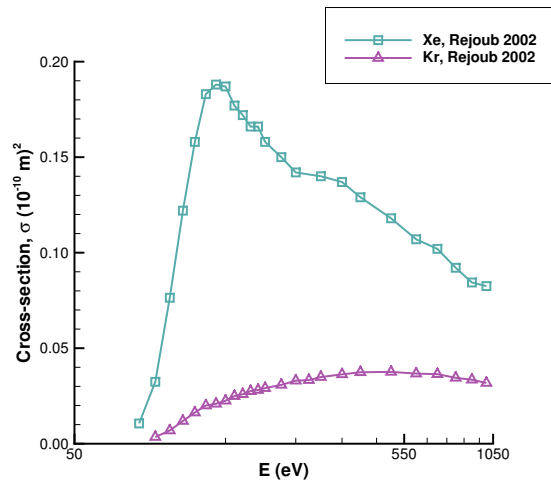
(c) Ground to triply charged.

Figure 3.2: Ionization cross-sections from the ground state.
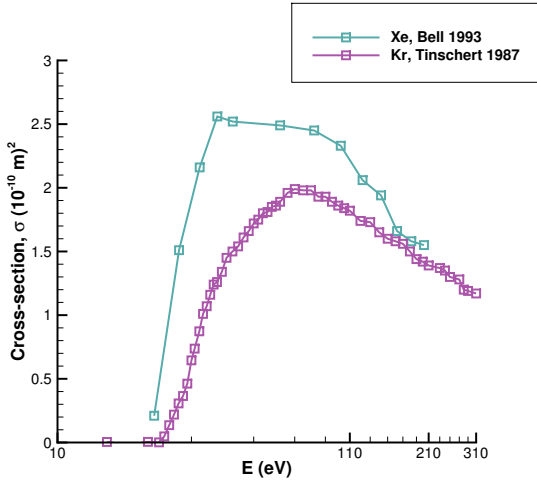
(a) Singly to doubly charged.
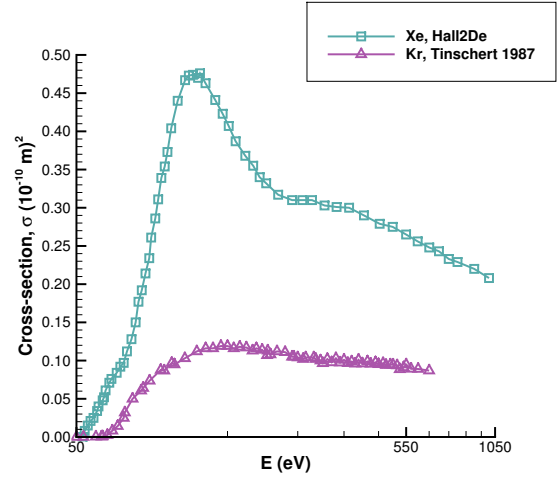
(b) Singly to triply charged.

Figure 3.3: Ionization cross-sections from singly charged ions.
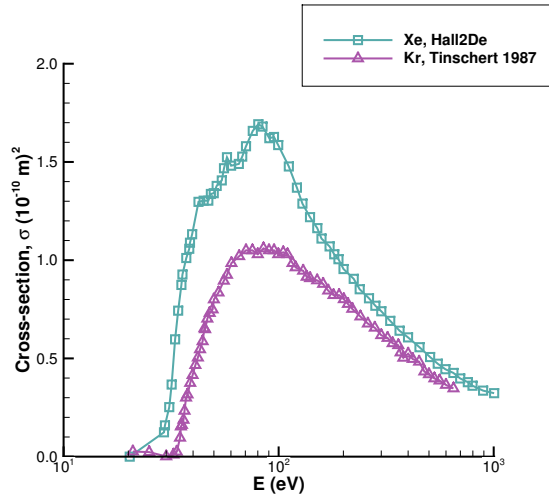
Figure 3.4: Cross-sections for the doubly to triply charged ionization process.
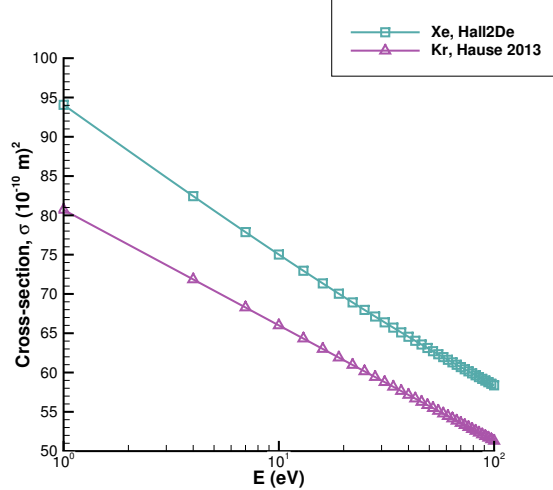
Figure 3.5: Cross-sections for the charge exchange process (neutral $\leftrightarrow$ singly charged ion).

3.3 Experimental Assessment for NASA-300M Thruster

The krypton implementation must be assessed against experimental data, and the NASA-300M thruster is selected for this purpose due to the availability of experimental measurements [51] and a previous Hall2De simulation with xenon propellant [69]. The NASA-300M is a 20-kW class Hall thruster that was designed, fabricated, and assembled at NASA Glenn Research Center in 2004-2005, and further characterized in 2010-2011. Finally, in 2013 the principles of magnetic shielding [68] were applied to produce the NASA-300MS [52]. In the present work, the unshielded thruster is simulated.

3.3.1 Simulation Setup

The starting point for the comparison is a previous xenon simulation, performed for the 500 V, 40 A operating condition. However, only the magnetic field-aligned mesh is identical between the original work performed by Mikellides [69] and the present simulations.

(a) Plasma properties.

(b) Electron collision frequencies.
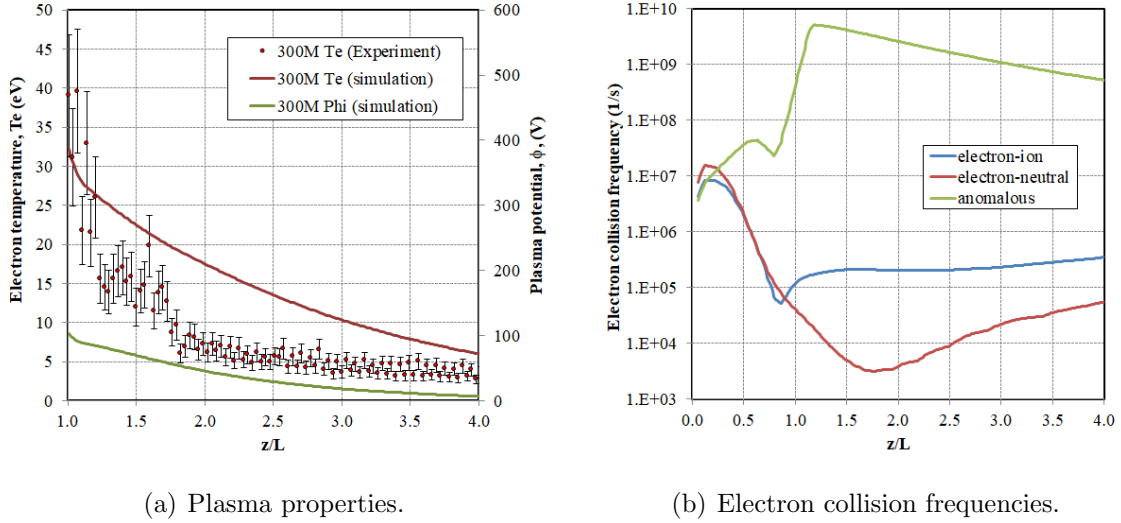
Figure 3.6: Electron collision frequency values selected to use within the Hall2De simulation are experimentally informed by the NASA-300M thruster operating at 500 V, 40 A with xenon propellant.

The electron collision frequency profile is informed by experimental measurements of the temperature and thrust. However, this data was only available for xenon thruster operation. Therefore, the same anomalous electron collision frequency profile is used for both xenon and krypton simulations. Figure 3.6 presents plasma properties at the channel centerline. The electron temperature profile obtained from the simulation is compared to the experimental measurement in Fig. 3.6(a). In addition, the computed plasma potential in the near-plume region is also presented on the same plot. Since measurements inside the channel may perturb the plasma parameters and result in an axial shift of as much as 15-20% of the channel length [49], the comparison inside the channel is not shown. The electron temperature obtained from Hall2De lies within the experimental error, for up to 1.5 z/L. Next, the electron-ion, electron-neutral and anomalous collision frequencies are plotted in Fig. 3.6(b). The anomalous collision frequency increases sharply at the channel exit, but begins to decrease further in the plume.

Table 3.2: NASA-300M operating conditions.

P_d (kW)	V_d (V)	I_d (A)	Xe $\dot{m}$ (mg/s)	Kr	% difference Kr vs. Xe
20	500	40.0	35.7	25.8	-35.5

Furthermore, in the laboratory the magnetic field was fine-tuned for each operating condition [69]. In the simulations we account for differences in magnitude between the xenon and krypton magnetic fields, but use the xenon magnetic field topology in both cases. While these approximations may produce discrepancies between simulation and experiment, the goal is to qualitatively evaluate the results of the krypton simulation by comparison with values from experiments, and also a xenon simulation.

A set of two Hall2De simulations are prepared: one with xenon and one with krypton propellant. The operating conditions are summarized in Table 3.2. To operate at the same power level, the krypton mass flow rate is 35.5 percent lower than in the case of xenon, and this value is the same as used in the experiment.

3.3.2 Theoretical Estimate

Before analyzing the simulation data, a simplified thruster performance calculation estimate is performed. The goal is to compute the thrust (Eq. 3.4) and specific impulse (Eq. 3.5) for the two propellant gases by only considering the discharge voltage and discharge current. The estimate for thrust magnitude requires a value for mass flow rate and speed, while the specific impulse is dependent on the thrust and mass flow rate.

$$F_{thrust} = \dot{m}v \tag{3.4}$$

$$I_{sp} = \frac{F_{thrust}}{g_0 \dot{m}} \tag{3.5}$$

Starting with the definition of thruster mass efficiency in Eq. 3.6 we can express the mass flow rate as a function of beam current, ion mass, and charge. Assuming that the beam current can be estimated as approximately 75% of the discharge current, setting the mass efficiency to a value of 1, and only considering singly charged ions, provides a means of estimating the mass flow rate directly from the discharge current.

$$\eta_{mass} = \frac{I_{beam} m_{ion}}{i_{charge} e \dot{m}} \tag{3.6}$$

The velocity magnitude value needed in the thrust computation may be derived from an energy conservation principle. By neglecting all other forms of energy, we set the kinetic energy equal to the electric potential energy, and thus derive the expression in Eq. 3.7. Note that we are using the value of the discharge voltage without accounting for the cathode fall. The potential reduction due to the cathode fall may be considered as part of the thruster efficiency. It is difficult to ascertain how the cathode fall value for krypton compares to that of xenon, so in order to produce a prediction based solely on known data, we compute the velocity magnitude as described here.

$$v = \sqrt{\frac{2 V_d e}{m_{ion}}} \tag{3.7}$$

Therefore equations 3.6 and 3.7 can be combined with Eq. 3.4 and Eq. 3.5 to provide thrust and specific impulse estimates based only on the thruster operating point as defined by its discharge current and voltage.

$$\eta_{current} = \frac{I_{beam}}{I_d} \tag{3.8}$$

Table 3.3: NASA-300M performance estimates for $I_d = 40$ A, and $V_d = 500$ V.

	Xe	Kr	% difference Kr vs. Xe
$\dot{m}$ (mg/s)	27.8	16.7	-39.9
F_{thrust} (mN)	943.1	731.8	-22.4
I_{sp} (s)	3458	4457	28.9

Applying the above approach for the operating condition discussed in Section 3.3.1 at 40 A and 500 V for both xenon and krypton yields the results summarized in Table 3.3. We assumed a value of 0.8 for the current utilization efficiency (Eq. 3.8), which is based on the average value measured for the 300M [44].The percent difference between the krypton and xenon estimates for all three parameters is independent of operating condition, so the trends shown in this example are expected to hold at all operating conditions. Thus when comparing the Hall2De simulations, the krypton case should produce a higher specific impulse but lower thrust than when using xenon propellant.

3.3.3 Results

Performance data for xenon and krypton thruster operation from both experimental measurements [51] and Hall2De simulations are summarized in Table 3.4 for the 20 kW and 500 V operating condition.

As expected from the reduced order model in Section 3.3.2, for the same voltage and discharge current, the krypton propellant produces higher specific impulse than xenon, in both simulation and experiment. For the simulation values, the increase is 15%, while the back-of-the-envelope calculation predicted an increase of 28.9% and the experimentally measured values showed an increase of only 6%. This discrepancy is due to the mass efficiency of the thruster being actually less than one.

The computed thrust for the xenon simulation is 6% lower than the experimental

Table 3.4: NASA-300M performance results for $I_d = 40$ A, and $V_d = 500$ V.

				% computed vs. measured	
	Xe	Kr	% Kr vs. Xe	Xe	Kr
F_{thrust} (mN) computed	965.8	803.4	-16.8	-6.2	1.8
F_{thrust} (mN) measured	1029.4	788.9	-23.4	-	-
I_{sp} (s) computed	2757.7	3174.3	15.1	-6.1	1.7
I_{sp} (s) measured	2937.3	3122.0	6.3	-	-

measurement. As reported by Kamhawi [51], the uncertainty of the inverted pendulum thrust stand measurements is estimated at 2%, which leaves a 4% discrepancy in the numerical results. This may be explained by differences in the applied magnetic field. Specifically, the topology of the magnetic field used in the simulations is modified to ensure radial symmetry about the channel centerline. However, the actual magnitude of the field, and the centerline profile are retained in the simulations.

For krypton, the computed thrust is within the 2% uncertainty of the experimental measurements. Since the specific impulse and thrust are linearly dependent, the comparison with experiment is only performed for thrust.

In addition to thrust and specific impulse, thruster lifetime is also a critical parameter to consider when exploring a new propellant. Surface erosion is a significant life limiting process, so we are interested in quantifying factors that contribute to this process. As described by Mikellides [69], the erosion rate ϵ may be defined as:

$$\epsilon = j_{i,\perp} \cdot Y$$

where $j_{i,\perp}$ is the ion current in the direction normal to the surface and Y is the sputter yield per unit charge, a function of both ion energy and incidence angle. The flux towards each surface is given a positive sign. Figures 3.7 and 3.8 show the Hall2De

computed ion current density incident to the inner and outer walls of the thruster and pole pieces, respectively. We notice that for all surfaces examined the flux of singly charged ions is dominant in magnitude, however we also show the fluxes for the higher charge species.

For the inner pole region singly charged Xe has a larger current density in the region between the cathode and 1.1 r/L than Kr, with a maximum value of 280 A/m^2 versus 168 A/m^2 for Kr. Then Kr current density becomes larger between radial coordinates of 1.1 r/L and 1.5 r/L. A similar trend is maintained for both the doubly and triply charged species however, the point where the Kr flux becomes dominant changes. For the doubly charged species this occurs at r = 0.8 r/L while for the triply charged species at 0.6 r/L.

The outer pole region shows higher fluxes of Kr for the singly charged ion species - roughly twice as large as for Xe: the maximum for Kr is 0.017 A/m^2, while for Xe the maximum value is 0.0084 A/m^2. The same trend is observed for the doubly charged species. However, the triply charged xenon current is three times larger than for Kr.

For the inner wall we observe that both singly charged Xe and Kr produce similar ion current densities with a maximum of 156 A/m^2 for Xe and 152 A/m^2 for Kr. This effect is two orders of magnitude larger than the contribution from the doubly charged ions, and 3-4 orders of magnitude larger than the contribution from triples. However, it is interesting to note that doubly and triply charged Xe ions have a larger current contribution to the wall than Kr.

For the outer channel wall, the singly charged Kr ion current density is slightly larger ($\approx 10\%$) than for Xe, with a maximum value of 144 A/m^2 versus 129 A/m^2. This

trend is however reversed for the doubly and triply charged species, but since the magnitudes are two and four orders of magnitude smaller than the fluxes from the singly charged species, the effect is negligible.

While the erosion rate is directly proportional to the ion current density in the direction incident to the wall, it is also directly proportional to the sputter yield. In turn, the sputter yield depends on the ion energy. Assuming that the energy gained by the xenon and krypton particles while traversing the sheath is similar (similar potential drop) we may base our discussion of erosion rate only on the ion current densities. Therefore, we expect that the erosion rate for the outer channel will be similar with xenon and krypton propellant, while for the inner channel we expect the Kr propellant to produces 10% higher erosion. Considering the inner pole piece, we expect a significant difference from using Kr since the erosion rate in the region between the cathode and r = 1.1 r/L is 1.7 times smaller than for Xe. For the outer pole piece we expect twice as much erosion from the Kr propellant, however these values are four orders of magnitude smaller than what is observed in the channel and on the inner pole.

3.4 Application to H6US

The H6US thruster was developed and characterized through a joint effort by National Air and Space Administration (NASA), the University of Michigan, and the Air Force Research Laboratory (AFRL) between 2007 and 2008. It is a 6 kW device with a throttling range between 100-600 mN and 1000-3000 s specific impulse [31, 85, 10, 84]. In 2011-2012 the H6 HET was used for a proof of concept development of magnetic shielding [68], at which point the original thruster was dubbed the H6US, and the magnetically shielded device H6MS [65, 40, 67, 70].
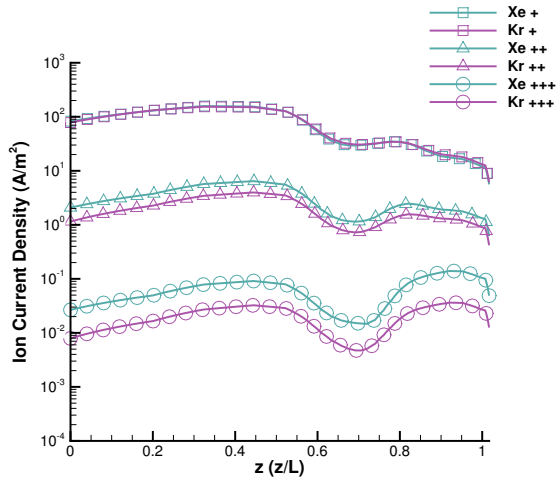
(a) Inner wall.
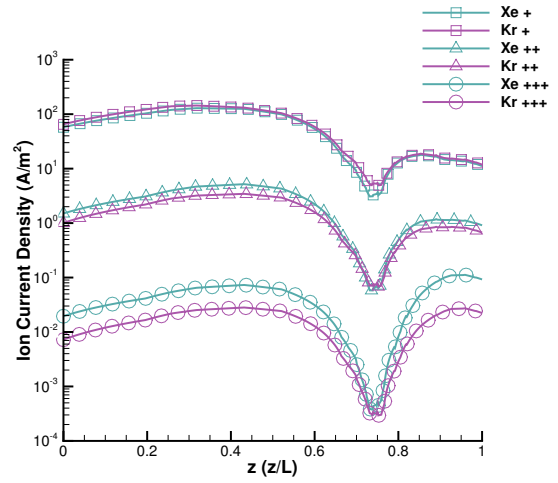
(b) Outer wall.

Figure 3.7: NASA-300M time-averaged ion current from Hall2De normal to the thruster walls for single (square), double (delta) and triple (circle) ions of xenon (green) and krypton (purple) gases. These values are for the lower-energy ion fluid (channel ions) - the other population showed small contributions and was not included.
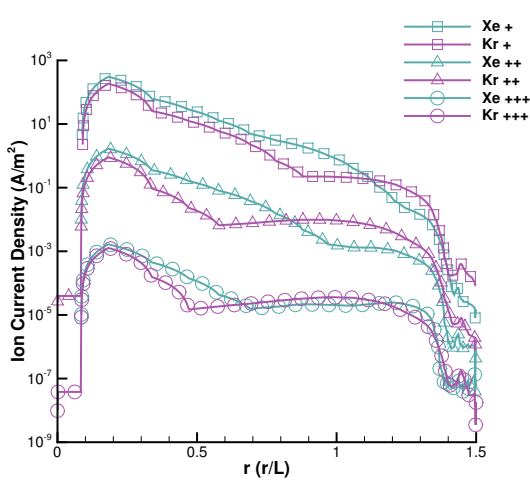
(a) Inner pole.
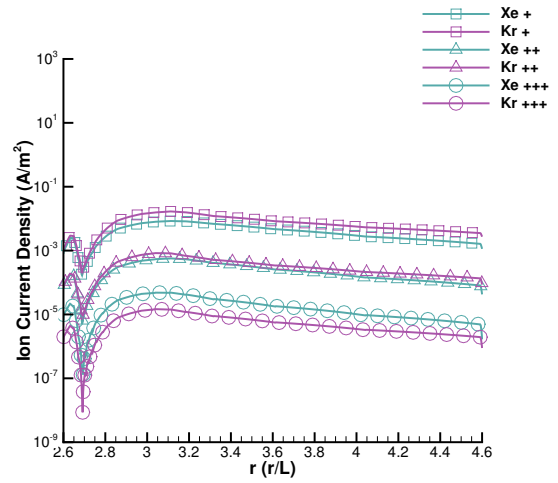
(b) Outer pole.

Figure 3.8: NASA-300M time-averaged ion current from Hall2De normal to the thruster pole pieces for single (square), double (delta) and triple (circle) ions of xenon (green) and krypton (purple) gases. These values are for the high-energy ion fluid (cathode ions) - the other population showed small contributions and was not included.

3.4.1 Simulation Setup

A baseline simulation is prepared for the H6US with xenon propellant, operating at 6 kW and 300 V at a mass flow rate of 19.7 mg/s. Next, a simulation with krypton gas is set up that uses the flow rate, magnetic field topology and magnitude from the xenon case. In addition, since there is no experimental guidance available, the electron anomalous collision frequency profile from the xenon simulation is also used for the krypton propellant. The full simulation domain extends axially to a value of 10.25 z/L, and radially to a value of 7.25 r/L, however, for illustration purposes, the figures are cropped to maximum values of 4 z/L and 4 r/L, respectively.

Upon completing the simulation, the computed anode current value is 28.8 A, which implies that the thruster is operating at 8.64 kW, and not 6 kW as in the xenon case. Thus a third simulation is prepared, where the krypton flow rate is set to 14.1 mg/s. This value is computed from the definition of mass efficiency, shown previously in Eq. 3.6. The beam current value is found by fixing the discharge power to 6 kW, the voltage to 300 V, and assuming $I_{beam} = 75\%I_d$. The mass efficiency is assumed to be the same as in the 19.7 mg/s krypton simulation, and that value is 0.992.

Note that the reduced mass flow rate for krypton is 28.4% lower than in the xenon simulation, within 7% of the difference in flow rate for the 300M experiments (Table 3.2, final column). Also, the percent difference in flow rate between krypton and xenon is 8% smaller than the prediction made in Section 3.3.2. The xenon flow rate used in the H6US simulation is 19.7 mg/s, while the prediction from Eq. 3.6 is 20.6 mg/s. The back-of-the-envelope calculation presented in Section 3.3.2 assumed only singly charged ions, and including higher charged species while keeping the efficiency constant will result in a reduced mass flow rate. Since the H6US simulation includes doubly and triply charged ions, the presence of these higher charge states explains

the difference in flow rate.

3.4.2 Results

Table 3.5 provides a summary of the macroscopic performance simulation results for the H6 thruster. The computed anode current values are shown for the three test cases. While the first krypton case yields a power level of 8.64 kW, the second krypton case where the mass flow rate is adjusted to lower the power gives 5.73 kW, showing that the scaling is successful. Closer agreement may be achieved by repeating the process and using the new value of efficiency obtained from the 14.1 mg/s simulation.

The thruster performance parameters are shown in Table 3.5: thrust and specific impulse. The thrust value is 14.8% higher than for xenon in the first krypton case, and 18.9% lower in the second. As expected, when operating at similar power levels, the thruster using a propellant that has a less massive atom and a higher ionization potential should produce a lower value of thrust. However, since the mass flow rate is lower and this is inversely proportional to the specific impulse, a higher I_{sp} is observed in both Kr cases. Thus, when using the same flow rate as xenon, a 14.8% higher I_{sp} is computed, while using a reduced mass flow rate produces a value that is 13.3% higher. Both trends in thrust and specific impulse are consistent with the back-of-the-envelope estimate from Section 3.3.2. While the percent difference in thrust between xenon and krypton is similar in value to the 20% predicted in Table 3.3, the increase in specific impulse for the krypton case is not as high as expected (25%), and this is due to the less than one value of mass efficiency from the simulation.

Furthermore, the table shows the current fractions for singly, doubly and triply charged ions. For single ions, the xenon current fraction is lower than for kryp-

ton, while for multiply charged ions, the xenon current fractions are higher than for krypton. These results are expected, considering the cross-section values presented previously in Section 3.2.2. When comparing the magnitude of different ionization cross-sections, the ground to singly charged values are the largest for both xenon and krypton. However, when comparing the ground to singly charged and ground to doubly charged transition, the maximum cross section decrease is 89% for xenon, and 91% for krypton. Further, when looking into the percent decrease between the singly charged to triply charged transition, the cross section decreases by 96% for xenon, and by 99% for krypton. This suggests that relative to the ground to singly charged transition, xenon ground to doubly charged and ground to triply charged transitions are more likely to occur than for krypton (the cross-sections do not decrease as much), however the relative percent differences between xenon and krypton are small.

When looking at the ground to singly charged versus the singly to doubly charged transition, we notice a significant difference. For xenon the maximum percent difference is 45%, versus 99% for krypton. This suggests that when comparing the two processes, for xenon we expect to see the production of more double ions that originate from the single to double ionization process than for krypton, and this may help explain the difference in doubly charged ion current fraction between the two gases seen in Table 3.5.

Finally, when comparing the ratio of ground to singly charged against singly charged to triply charged, the xenon propellant cross-sections decrease by 90% while for krypton it is by 97%. Also, the ratio of ground to doubly charged versus doubly charged to triply charged transition cross-sections decreases by 65% for xenon and 70% for krypton. Combined, these ratios suggest that the xenon cross-sections decrease less than the krypton ones when compared to the lower level ionization processes. In

Table 3.5: H6US thruster performance and ion current fractions from Hall2De simulation results for Kr and Xe propellant. Kr simulations were performed first at the same flow rate, and then at the same power as the Xe case.

Species	Xe	Kr	Kr
Flow rate (mg/s)	19.7	19.7	14.1
Anode current (A)	-21.1	-28.8	-19.1
Thrust (mN)	412	473	334
I_{sp} (s)	2200	2530	2420
Current fraction +	0.798	0.870	0.896
Current fraction ++	0.186	0.126	0.100
Current fraction +++	0.016	0.005	0.004

turn, this implies that we should expect a lower ratio of krypton triple ions than xenon triple ions when compared to the other two ion populations.

All of the arguments presented above regarding the ratio of ion currents are based on the cross-section values, and more specifically the maximum percent change between cross sections. Since these comparisons illustrate changes in cross-sections for the same species, and the ion mass does not change, the percent difference in collision probabilities will be the same as the percent change in collision frequencies. A more detailed statistical analysis may be performed in the future, however, experimental measurements from a retarding potential analyzer (RPA) will be necessary to fully validate the current fractions computed with Hall2De.

Figures 3.9-3.15 show comparisons between the xenon and krypton simulations at similar power levels. The electron temperature distribution is qualitatively similar between the two cases, as shown in Fig. 3.9. Since the thruster is operating at similar power levels in both cases, the Joule heating term from the energy equation ($\vec{E} \cdot \vec{j_e}$) is expected to have similar magnitudes for the two propellants, and this is a dominant effect within the thruster channel.

However, in the near-field plume, the temperature values decrease more rapidly for krypton than for xenon. Since the electric field and electron current density both diminish in the plume, this region is no longer dominated by the effects of Joule heating, but instead by the thermal conductivity and ionization loss terms. The thermal conductivity term decreases dramatically in the plume for both xenon and krypton, as seen in Fig. 3.10. The ionization cross-sections are consistently larger for xenon than krypton, and the ionization potential of krypton is higher than that of xenon. The combination of these physical properties makes xenon easier to ionize, but this process occurs primarily within the thruster channel.

However, Fig. 3.12 confirms that the neutral number density of krypton in the near plume is higher than that of xenon. As shown in Section 3.2.2, slower particles of lower charge number have higher ionization cross-sections, therefore a large population of slow krypton neutrals may be undergoing a significant number of ionizations that may lead to the rapid decrease in electron temperature that we observe in the plume. This hypothesis is also supported by measurements by Hargus [35] which suggest that latent krypton ionization occurs farther downstream than in the case of xenon.

The plasma potential distribution (Fig. 3.11) is also qualitatively similar inside the channel. However, higher potential values are seen in the xenon near-field plume, as expected since the electron temperature is also higher in that region than in the krypton case.

The singly charged ion species (Fig. 3.13) fraction for both gases is larger than the higher charge species due to the higher ground to singly charged ionization probability when compared to the other ionization processes. When considering a comparison

(a) Xenon $\dot{m} = 19.7$ mg/s.

(b) Krypton, $\dot{m} = 14.1$ mg/s.
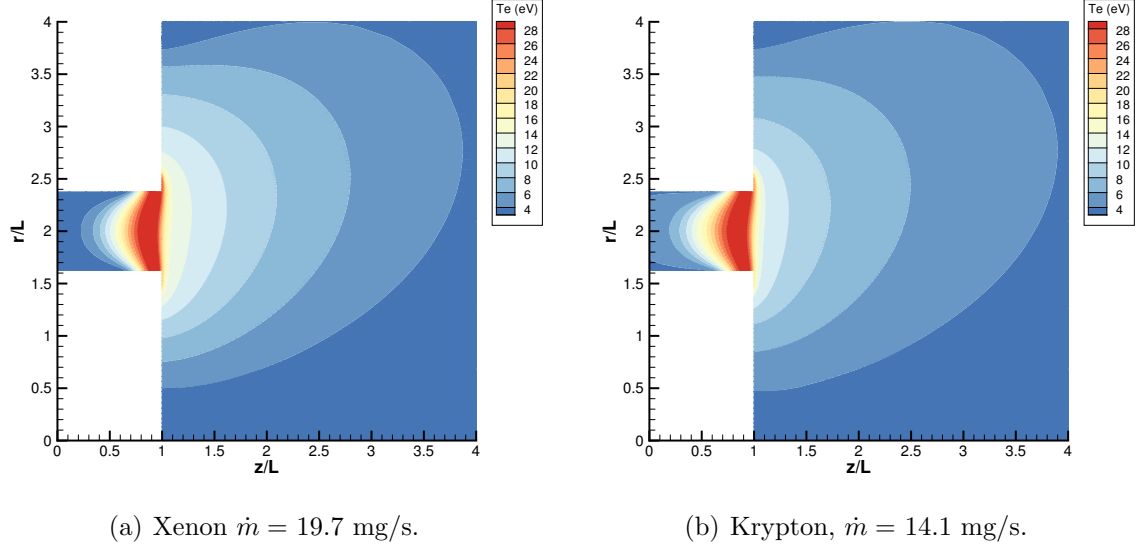
Figure 3.9: H6US time-averaged electron temperature from Hall2De.

of the doubly charged ion species (Fig. 3.14), we observe larger differences between xenon and krypton, with the krypton showing lower density values throughout the entire domain. A similar trend is also true for the triply charged ions shown in Fig. 3.15. These observations are consistent with the ion current fractions reported in Table 3.5, which show that the xenon singly charged current fraction is lower than for krypton, while for the higher charge states the trend is reversed.
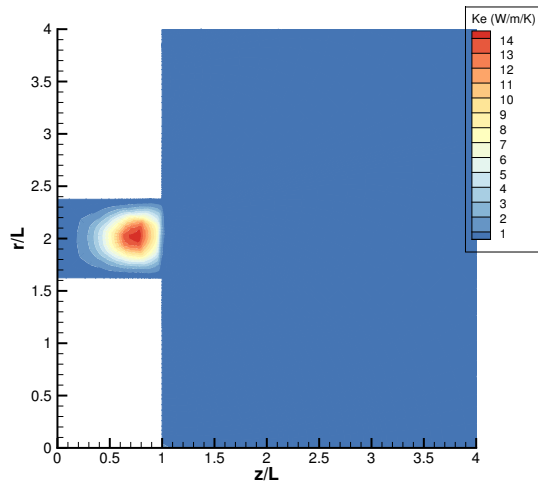
(a) Xenon $\dot{m} = 19.7$ mg/s.
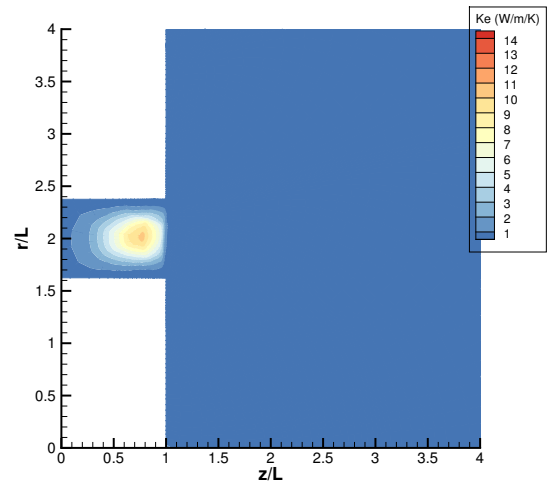
(b) Krypton, $\dot{m} = 14.1$ mg/s.

Figure 3.10: H6US time-averaged thermal conductivity magnitude from Hall2De.
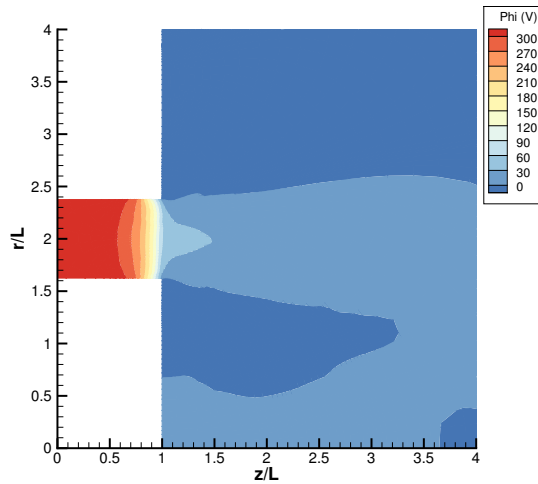
(a) Xenon $\dot{m} = 19.7$ mg/s.
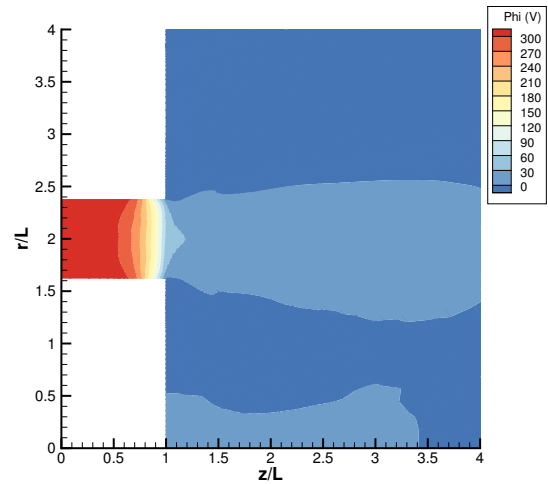
(b) Krypton, $\dot{m} = 14.1$ mg/s.

Figure 3.11: H6US time-averaged plasma potential from Hall2De.
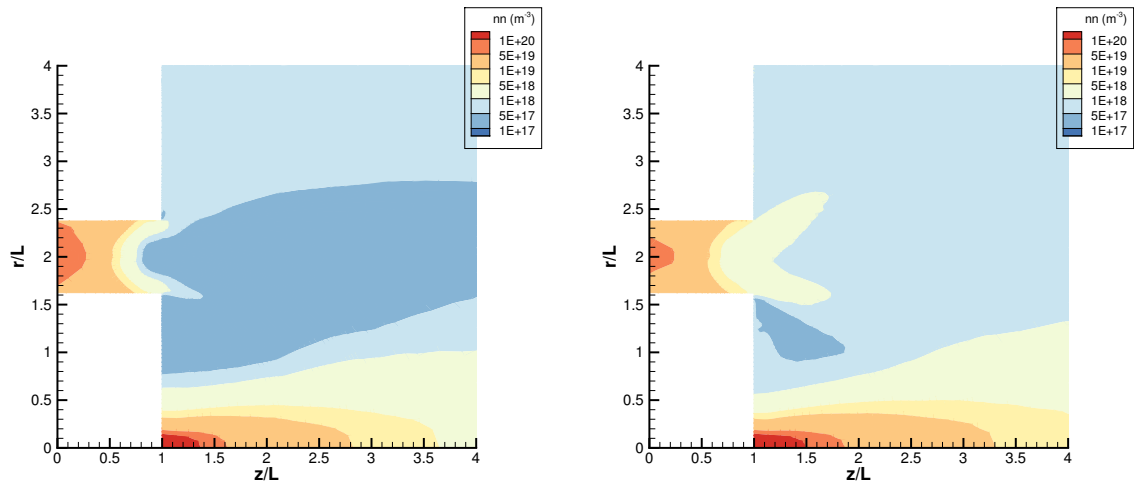
(a) Xenon $\dot{m} = 19.7$ mg/s.

(b) Krypton, $\dot{m} = 14.1$ mg/s.

Figure 3.12: H6US time-averaged neutral number density from Hall2De.
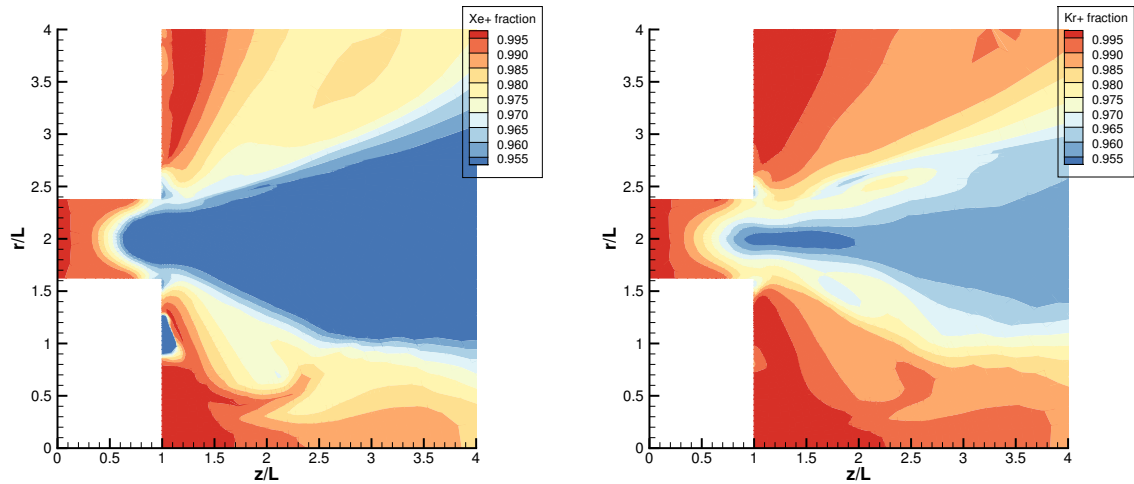
(a) Xenon $\dot{m} = 19.7$ mg/s.

(b) Krypton, $\dot{m} = 14.1$ mg/s.

Figure 3.13: H6US time-averaged singly charged ion fraction from Hall2De.
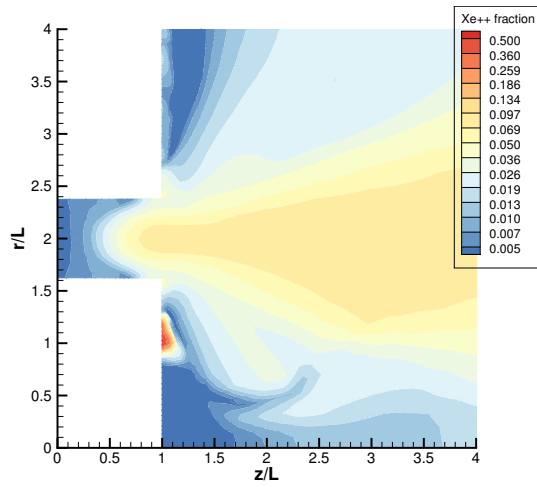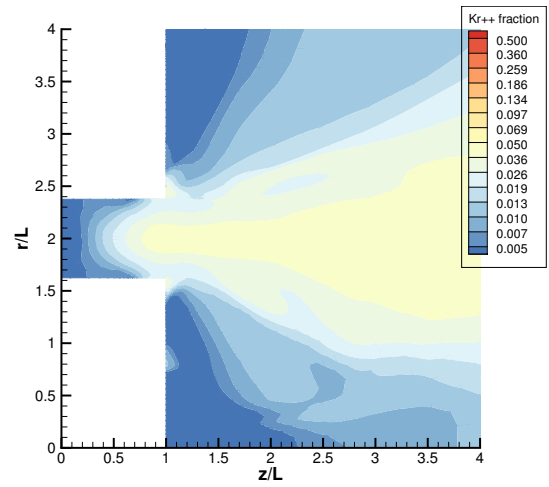
(a) Xenon $\dot{m} = 19.7$ mg/s.

(b) Krypton, $\dot{m} = 14.1$ mg/s.

Figure 3.14: H6US time-averaged doubly charged ion fraction from Hall2De.
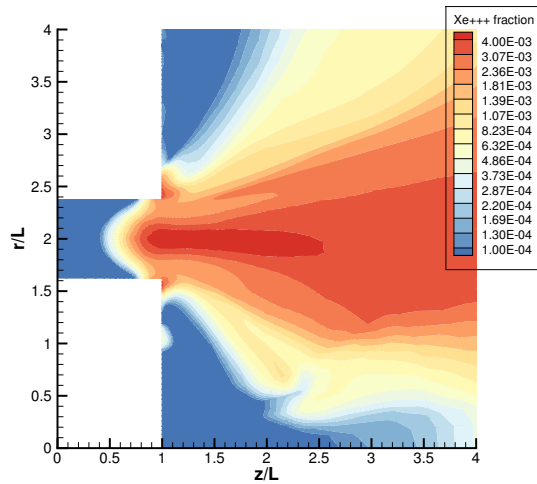
(a) Xenon $\dot{m} = 19.7$ mg/s.
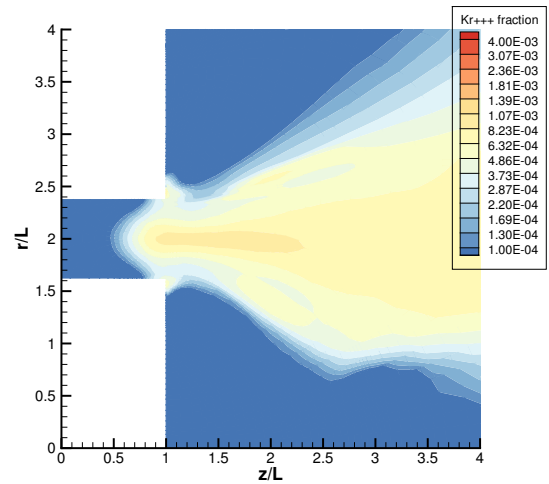
(b) Krypton, $\dot{m} = 14.1$ mg/s.

Figure 3.15: H6US time-averaged triply charged ion fraction from Hall2De.

3.5 Summary

Krypton was incorporated as a propellant species in the Hall2De code, thus enabling further exploration of a less expensive alternative to the ubiquitous xenon gas that is currently being used for the majority of Hall effect thrusters. This work involved updates to all the physical properties that describe krypton such as mass, ionization potentials and collision cross-sections. First, a back-of-the-envelope thruster performance calculation was presented to help evaluate the simulation results under the assumptions of a single charged species, and a mass efficiency value of unity. Next, a first set of simulations was performed on the NASA-300M thruster to assess the implementation by comparison with experimental data, and the thrust value was matched to within 6% for xenon and 2% for krypton. The trends observed in thrust and specific impulse matched the reduced order theoretical calculation. The thrust was 17% higher for the xenon propellant than krypton, while the prediction was 22.4%. Moreover, the krypton simulation produced a specific impulse value 15% higher than xenon, while the theoretical estimate was an increase of 28.9%. We observed a lower increase than expected because in computing the predicted value it was assumed that the thruster had a mass efficiency of one, and only singly charged ions, while in the simulation the efficiency value was lower, and three charged species were present.

Additionally, thruster surface erosion was also investigated. Incident ion current density values from Hall2De suggest that for the inner pole piece we expect a 1.7 higher erosion rate for xenon propellant than for krypton, between the cathode and r = 1.1 r/L. For the channel walls, the erosion rate is similar between xenon and krypton with a maximum difference of 10% with the Kr having the higher erosion rate on the inner channel. Finally, for the outer pole the expected Kr erosion rate is roughly double that of Xe however, the ion fluxes on this surface are four orders of magnitude smaller than

for the other surfaces studied, so the effect of erosion is considered small in this region.

Upon finding satisfactory performance of the krypton implementation by comparison with both the theoretical model and NASA-300M thruster, the next goal was to study the performance and plasma properties of krypton in an H6US thruster. Given the lack of experimental data for krypton operation, the numerical investigation began with a xenon test case. It was found that a 28.4% lower mass flow rate was required for krypton to reach the same 6 kW discharge power as the xenon case. Further, 13.3% higher specific impulse was recorded when compared to xenon, and the thrust values obtained with krypton were lower by 19% than with xenon. The percent difference in thrust was close to the theoretical estimate. However, the specific impulse increase for krypton was lower than expected, due to the presence of multiply charged species in the simulation which led to a lower mass flow rate for xenon (compared to the estimate), and thus a higher specific impulse. In addition, the ion current fractions for the two gases were compared, and the Hall2De results showed the expected trend, based on the difference in cross-sections. While the singly charged xenon current fraction was smaller than that of krypton, both higher charge states had higher fractions than krypton, and this behavior was also observed in the spatial distribution of ion number densities. Finally, the electron temperature was examined. While in the thruster channel Joule heating ensured that the two propellants produced a similar temperature distribution, once the electric field and current density began to diminish in the near-field plume, a faster decrease in temperature was observed for the krypton propellant. Considering the neutral and ion number density profiles, the likely cause for the temperature decrease were higher ionization losses for the krypton case.

In summary, the simulation of two types of Hall effect thrusters in conjunction with a

simple theoretical model and experimental data have shown that the krypton species was successfully implemented in the Hall2De framework. It was found that krypton ionization may occur farther downstream than for xenon. In addition, while the use of krypton propellant is expected to produce lower thrust than xenon, operating the thruster at the same power level will require a significantly lower flow rate, and produce a higher specific impulse.

CHAPTER IV

Channel Erosion

4.1 Motivation

Historically, the main failure mode of Hall thrusters has been the erosion of their insulating ceramic channel walls. Since the eroded material from the plume may deposit on sensitive spacecraft surfaces such as solar panels, the expected mission duration may be limited. Hence, added knowledge of the erosion process can provide valuable information about the thruster lifespan, spacecraft integration, and a better understanding of the physical processes involved. While the recent development of magnetic shielding [65, 40, 67] has effectively mitigated thruster channel erosion, this technology is still not in use for most commercial thrusters, or the high-power NHT designs. Thus, thruster erosion is still a significant limiting factor that must be considered when planning a mission with an unshielded thruster design.

Presently, the end-of-life for an unshielded thruster is predicted by operating the device in a vacuum chamber for a long duration, until significant damage to the walls is observed and quantified. Some methods for characterizing the damage, like multi-layer chip erosion [13], involve modifying the channel walls to include several tracer materials that can be easily tracked during the erosion process. Another diagnostic technique, developed in [89], involves installing flush-mounted Langmuir probes in

the thruster wall. Yet this only provides localized information, and requires special machining of the thruster walls.

Therefore, a non-intrusive technique that can be used during testing, which does not require thruster wall alterations or extended operation is advantageous. This method would provide significant cost benefits as well as reduced interference with the plasma. A Cavity Ring-Down Spectroscopy (CRDS) technique was developed in [56] to satisfy these requirements. The procedure provides line integrated values of sputtered boron number density in the plume, measured at a distance of 2 mm away from the thruster exit plane. CRDS records the number of boron atoms in the ground electronic state. Thus atoms with excited electronic energy states, or boron ions are not accounted for. A computer simulation of a SPT-70 HET is developed that includes sputtered boron, and the results are compared to the experimental measurements.

Section 4.2.1 describes how the boron sputtering process is modeled in the simulation. The numerical simulation setup is presented in Section 4.2.2, and the post-processing algorithm used to obtain line-integrated number density values from the raw simulation data is explained in Section 4.2.3. The results are then presented and discussed in Section 4.3. The conclusion is provided in Section 4.4.

4.2 Simulation Setup

In the present case, only neutral boron and xenon atoms are considered, and electromagnetic plasma effects are neglected. Since the mean-free-path for boron and xenon collisions is large compared to the thruster channel size, little interaction is expected between the ionized species as well, so plasma effects are not expected to have a significant influence on the results. The computer code used for the simu-

lation, Monaco [7], is an implementation of the DSMC method and is described in Section 2.2. The program may be run on both scalar and parallel systems [17], and the results presented in this Chapter are obtained after executing the code on 6 cores. A new type of boundary condition is developed specifically to simulate the erosion of boron atoms from the thruster walls. Boron particles are introduced from the wall at a rate consistent with the erosion process, and the velocities of the boron atoms are assigned by sampling from the appropriate VDFs. The wall does not recede in time, but due to the relatively short real-time duration of the simulation (15 milliseconds), this factor has minimal impact on the results. In the initial simulation, boron atoms simply reflect back into the domain upon colliding with a thruster wall surface. It was suggested by the collaborators in the experimental group from Colorado State University that the boron neutrals in fact stick to the thruster wall, and so another simulation was prepared that incorporates this effect. The results are significantly different, and so both cases are presented in Section 4.3.

4.2.1 Modeling the Sputtering Process

The sputter boundary condition reproduces the physics of the wall sputtering process. The number of particles introduced through a given area, in a particular time interval, is derived from the sputtered boron particle flux, as explained in Section 4.2.1.3. The velocities assigned to the new particles are sampled from the corresponding boron VDFs through acceptance-rejection sampling [4]. A brief description of the VDFs is provided in Section 4.2.1.2.

The erosion boundary condition in Monaco requires an input value for the number density of material being eroded. By analyzing the geometry of the thruster, the volume of eroded material may be computed, and this is described in Section 4.2.1.1.

Considering the thruster operation time, an approximate value of the average erosion rate is calculated. Although the real erosion rate is not constant, but decreases in time [104], this approximation will not greatly influence the results since the physical time interval being simulated is short. Finally, the required value for boron number density can be calculated by combining the volume flow rate with knowledge of the sputtered atoms' VDFs.

4.2.1.1 Volumetric Erosion Rate

The geometry of the SPT-70 used in Lee's CRDS experiment [56] was recorded by profilometer measurements [20]. Linear functions that reproduce the profiles are illustrated in Fig. 4.1. It is assumed that before the thruster was first operated, both lines shown in Fig. 4.1 were horizontal. Thus to compute the volume eroded from the inner channel wall, the volume of rotation around the horizontal axis corresponding to the shape in Fig. 4.1(a) is subtracted from the area of a circular cylinder of the same axial length and constant radius of 0.020 m. Similarly, the eroded volume from the outer channel wall is computed by subtracting the volume of rotation of the curve in Fig. 4.1(b) from that of an annular circular cylinder of the same axial length and outer radius equal to the maximum height of the profile, and constant inner radius of 0.035 m.
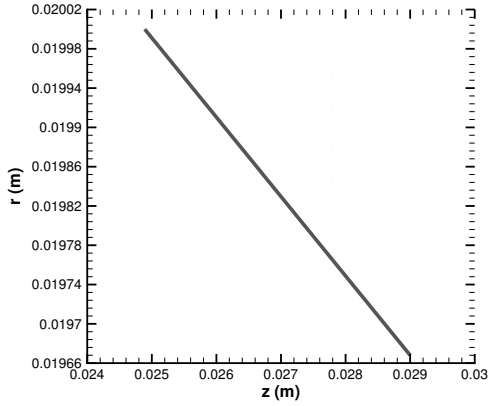
(a) Inner channel wall.
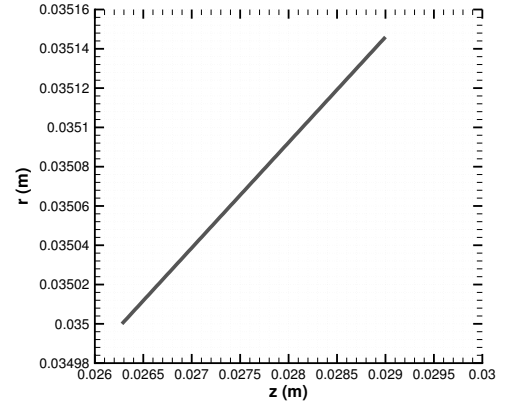
(b) Outer channel wall.

Figure 4.1: Measured erosion profiles for the SPT-70 [20]. The radial 0 coordinate is at the thruster centerline.

Following the procedure outlined above, the volume of eroded material from the outer channel wall is found to be $V_{outer} = 4.37 \times 10^{-8}$ m^3, and that from the inner channel wall, $V_{inner} = 8.53 \times 10^{-8}$ m^3. The total operation time for the HET is estimated to be 40 hours ($\pm$ 50% uncertainty), therefore the total volumetric erosion rate for the SPT-70 is:

$$\dot{V} = 8.96 \times 10^{-13} \text{ m}^3/\text{s} \tag{4.1}$$

4.2.1.2 Erosion VDFs

Smith and Boyd [90] have studied the sputtering of boron nitride due to xenon impact and obtained VDFs for boron atoms from a Molecular Dynamics (MD) simulation at 100 eV energy and 45° angle of incidence. Experiments in [95] have confirmed by laser-induced fluorescence spectroscopy that the VDFs of sputtered boron atoms correspond to Sigmund-Thompson distributions. Further work by Smith [91] has focused on studying additional ion bombardment conditions and sputter yields, and was validated by experimental quartz crystal microbalance measurements (QCM) [87]. However, the current model uses the VDFs identified [90] for the 100 eV energy

and 45° angle of incidence case.

In the direction perpendicular to the eroding wall, the VDF is of the Sigmund-Thompson form given in Eq. (4.2), and is plotted in Fig. 4.2(a). The VDF in the directions tangential to the wall is described by a bimodal Maxwellian in Eq. (4.4) and illustrated in Fig. 4.2(b). Note that the same distribution function, f_t, is used for two directions (axial and azimuthal) that define the plane tangential to the wall. Thus the sampling is done twice in order to obtain independent results for each of the two velocity components. Furthermore, both VDFs in Fig. 4.2 have been normalized such that the area under the curve equals one.

$$f_n(v_n) \propto \frac{v_n^3}{(v_n^2 + v_b^2)^{3-2m}} \tag{4.2}$$

where the constants are defined as: $v_b = 5.25 \times 10^3$ m/s and $m = 0$.

$$f_t(v_t) \quad \propto \quad \sigma g_1(v_t) + (1 - \sigma)g_2(v_t) \tag{4.3}$$

$$g_{1,2}(v_t) \quad = \quad \sqrt{\frac{m_B}{2\pi k_B T_{1,2}}} \cdot \exp\left[-\frac{m_B(v_t - c_{1,2})^2}{2k_B T_{1,2}}\right] \tag{4.4}$$

where the constants are defined as: $\sigma = 0.552$, $c_1 = -1.75 \times 10^3$ m/s, $c_2 = -8.56 \times 10^3$ m/s, $T_1 = 2.62 \times 10^4$ K and $T_2 = 3.86 \times 10^4$ K, and k_B is Boltzmann's constant. The variables v_n and v_t are normal and tangential velocities, respectively.
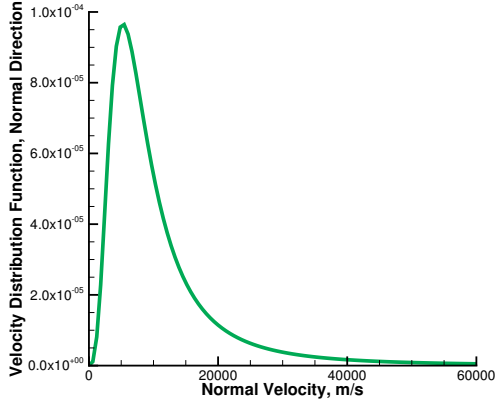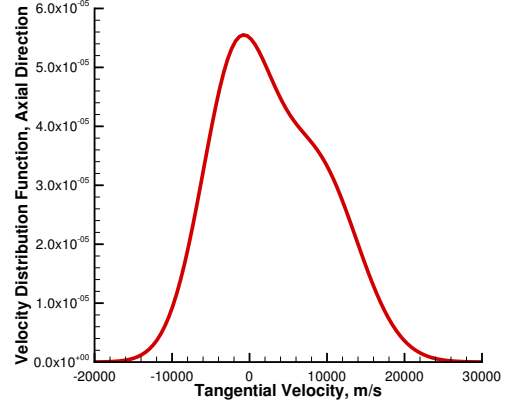
(a) Sigmund-Thompson.
(b) Bimodal Maxwellian.

Figure 4.2: Normalized velocity distribution functions for sputtered boron. [90]

4.2.1.3   Computing the Boron Particle Flux

The number flux of particles (Γ) that pass through a surface, in the direction perpendicular to it, may be expressed as:

$$\Gamma = \int_{0}^{\infty} n v_n f_{[n-\rho]}(v_n) dv_n \tag{4.5}$$

where $f_{[n-\rho]}$ is the density-based normalized VDF in the direction orthogonal to the wall surface. Introducing a normalization constant, $C_n = 7.32 \times 10^{11} \ m^3/s^3$, the distribution function is of the form:

$$f_{[n-\rho]}(v_n) = C_n \cdot \frac{v_n^2}{(v_n^2 + v_b^2)^{3-2m}} \tag{4.6}$$

where m and v_b are the same as in Eq. 4.2. Using Eq. 4.6, Eq. 4.5 is re-written as:

$$\Gamma = n C_n \int_{0}^{\infty} \frac{v_n^3}{(v_n^2 + v_b^2)^{3-2m}} dv_n \tag{4.7}$$

Since evaluating the integral in Eq. 4.7 in the limit at infinity does not yield meaningful results, it is evaluated at a finite upper bound. This value is chosen to be

61

7.32×10^4 m/s which corresponds to the 300 V discharge voltage of the thruster. It can be observed in Fig. 4.2(a) that most of the VDFs are included below this upper velocity bound. For simpler notation, the integral is renamed I:

$$I = C_n \int_0^{7.32 \times 10^4} \frac{v_n^3}{(v_n^2 + v_b^2)^{3-2m}} dv_n \tag{4.8}$$

The flux becomes:

$$\Gamma = nI \tag{4.9}$$

Numerical evaluation of Eq. 4.8 yields $I = 828.1$ m/s. As expected, this value is very similar to the thermal velocity corresponding to particles that have the wall temperature (810 K), which is 831.3 m/s.

Note that the rate at which particles are introduced through a given surface area, A, is given by:

$$\dot{N} = A \cdot \Gamma \tag{4.10}$$

Thus, over a given surface area A, and in a time interval Δt, the number of particles introduced in the simulation, based on the value of the flux from Eq. 4.9, is:

$$\Delta t \cdot A \cdot \Gamma = \Delta t \cdot \dot{N} \tag{4.11}$$

Although the choice for an upper integration limit used in the numerical evaluation of Eq. 4.8 is based on an approximation, the use of different values will not affect the simulation results. Using a higher value will increase I by a small increment, and the reverse will happen with the choice of a lower value. The factor I is used in the code to compute the particle flux, and the two variables are directly proportional. However, as shown in Section 4.2.1.4, the input value of number density is inversely

proportional to I. Therefore any changes in the computation of I will be implicitly accounted for.

4.2.1.4 Boron Number Density Values

Recall that the sputter boundary condition for the simulation requires the boron number density. A reasonable value may be derived from the volumetric erosion rate that was computed in Section 4.2.1.1. The first step is to calculate the mass flow rate of sputtered material, which is HBC grade boron nitride [104]. Its density is well known [46], and defined as $\rho_{HBC} = 1950$ kg/m^3. The procedure described below to compute the mass flow rate is applied to both the inner and outer channel walls, yielding values for the two number densities, respectively.

The first step is to express the mass erosion rate, $\dot{m}_{HBC}$, as the product of the volumetric erosion rate, $\dot{V}$ multiplied by the density of the ceramic, ρ_{HBC}. The volumetric erosion rate was found previously in Eq. 4.1.

$$\dot{m}_{HBC} = \dot{V} \cdot \rho_{HBC} \tag{4.12}$$

The mass flow (erosion) rate of boron nitride may also be expressed as:

$$\dot{m}_{HBC} = m_B \cdot \dot{N}_B + m_N \cdot \dot{N}_N \tag{4.13}$$

where $\dot{N}_B$ and $\dot{N}_N$ are particle erosion rates for boron and nitrogen, respectively, and m_B and m_N are particle masses for boron and nitrogen.

Note that in an experimental facility, a low sputter yield material (typically carbon) is used to coat the interior of the vacuum chamber. During thruster operation, this

material is sputtered and redeposited on the thruster surface. In the present case, the contribution of deposited material on the thruster walls is neglected from the volume flow rate computation. The carbon deposition rate for the experimental facility at Colorado State University was characterized and found to be three orders of magnitude smaller than the thruster wall erosion rate: 11 nm/h versus 3.8 μm/h [20].

Although instantaneously boron and nitrogen may erode at different rates, over long enough time periods entire layers of boron nitride are eroded together. This suggests that considering equal values of the erosion rates for boron and nitrogen is a reasonable assumption. The boron erosion rate may be denoted as $\dot{N}$ and computed as:

$$\dot{N} = \frac{\dot{m}}{m_B + m_N} \tag{4.14}$$

Combining Eqs. 4.9 and 4.10, the number density may be expressed as:

$$n = \frac{\dot{N}}{I \cdot A} \tag{4.15}$$

All the information on the right hand side of Eq. 4.15 is known, thus numerical values for the inner and outer channel walls are obtained:

$$n_{outer} = 1.32 \times 10^{16} \text{ m}^{-3} \tag{4.16}$$

$$n_{inner} = 4.38 \times 10^{16} \text{ m}^{-3} \tag{4.17}$$

Now consider the case where boron atoms consequently stick to the walls, upon colliding with any thruster surfaces. To account for the loss of particles due to the sticking process, the eroded boron mass inflow rate is adjusted:

$$\dot{m}_{sticking} = \dot{m} + \dot{m}_{deposition} \tag{4.18}$$

where $\dot{m}$ is the value obtained from geometric considerations in Eq. 4.13, and $\dot{m}_{deposition}$ is the total rate of mass deposition on the thruster channel surface. The second term from the right hand side of Eq. 4.18 is obtained by integrating the incident boron mass flux (computed by Monaco) over the wall surface, and has a numerical value of 1.54×10^{-10} kg/s. The $\dot{m}_{deposition}$ total value is added to the outer and inner channel wall erosion flow rates in proportions similar to those obtained for the mass flow rate values obtained previously, from geometric considerations. For the case where all particles are reflected by the wall, the accommodation coefficient at the wall is 1, and the reflected particles are assigned a Maxwellian VDF at the wall temperature.

The erosion inflow number density values for the inner and outer channel walls are obtained for the sticking case, by using Eqs. 4.14 and 4.15 with the value of mass flow rate computed from Eq. 4.18:

$$n_{outer} = 1.44 \times 10^{16} \text{ m}^{-3} \tag{4.19}$$

$$n_{inner} = 4.79 \times 10^{16} \text{ m}^{-3} \tag{4.20}$$

Note that the procedure described above to obtain the value of $\dot{m}_{sticking}$ is iterative. The simulation is first run with the initial non-sticking value of $\dot{m}$. This gives the value of deposited boron mass, which is then incorporated in $\dot{m}_{sticking}$ as described in Eq. 4.18. The computed value of $\dot{m}_{deposition}$ is less than 10% of the value used in the case without sticking, for the first such iteration. Since a second iteration is expected to produce a change of less than 1%, the procedure is not repeated again.

Table 4.1: Simulation parameters for Monaco erosion study.

Parameter		Non-sticking wall value	Sticking wall value
n_{Xe}	(m^{-3})	2.25×10^{20}	2.25×10^{20}
n_B^{inner}	(m^{-3})	4.38×10^{16}	4.79×10^{16}
n_B^{outer}	(m^{-3})	1.32×10^{16}	1.44×10^{16}
Timestep	(ns)	300	300
Simulation time	(ms)	12	12
Wall temperature	(K)	810	810
Inflow temperature	(K)	810	810
Number of particles		1.35×10^6	6.50×10^5
Particle weight		1.0×10^{10}	1.0×10^{10}

4.2.2 The Monaco Simulation

An axisymmetric simulation is performed, but plasma effects are not considered. Two neutral gases are introduced in the Monaco domain: 1) the xenon propellant, and 2) the boron that is eroded from the walls. Xenon is included in the simulation to provide a comparison of densities, and show that the number of boron atoms is significantly smaller than that of xenon atoms. The time step is set to 3×10^{-7} seconds, and an average number of model particles in the simulation is 1.35×10^6 when boron reflects from the walls, and 6.50×10^5 when the boron neutrals stick. For xenon, the ratio of real to model particles is 10^{10}, whereas for boron the ratio is 1.25×10^6. The simulation is run for 10,000 time steps to reach a steady state. Then, average values of particle properties are sampled for another 40,000 time steps in order to arrive at the values that are presented in Section 4.3. The simulation input parameters are summarized in Table 4.1.

4.2.2.1 Mesh and Boundary Condition Types

A non-uniform triangular mesh is employed, and is shown in Fig. 4.3. The boundary condition types are labeled on the figure, as follows: SYM for symmetry, IN for in-

flow, OUT for outflow, WALL for the wall condition and SPUTTER for the eroding wall. The xenon inflow condition introduces particles in the domain with specified number density, temperature and bulk velocity components (here all the bulk velocity components are 0 m/s, for both gases). The flux used to determine the number of xenon particles introduced is derived from a Maxwellian VDF. The xenon particles are inserted in the domain through an annular section of 0.005 m width, at a rate of 25 sccm, as described in Lee's experimental set-up [56] . In thruster operation, an additional 2 sccm of xenon is introduced through the cathode, and this is neglected in the present study. The outflow condition allows particles to leave the domain. The wall reflects particles, and may also accommodate a certain fraction of the reflected particles to the wall temperature. In the present simulation, all reflected particles are accommodated to the wall temperature which is set to 810 K, based on experimental measurements by Valentian et. al. [98].

The sputter boundary condition combines characteristics of both the inflow and wall boundary types. Particles colliding with the eroding wall are accommodated to the 810 K wall temperature and reflected back into the domain. New boron particles are introduced to the simulation with the particle flux derived from the Sigmund-Thompson distribution, in Eq. 4.9. For the case where the boron reflects from the walls, the erosion inflow number densities are given in Eqs. 4.16 and 4.17, while for the case where the boron neutrals stick to the walls, the inflow number densities are defined in Eqs. 4.19 and 4.20. Note that the sticking wall condition is enforced within the simulation by removing all boron particles that reach the wall.
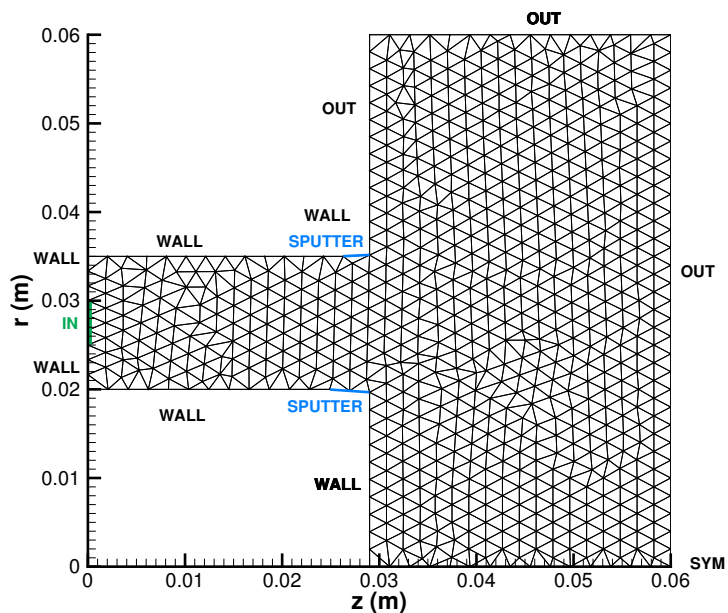
Figure 4.3: 2D-axisymmetric mesh used in Monaco simulation.

4.2.3 Path-Integrated Number Density

The CRDS technique yields path-integrated values of the number density (in m^{-2}) in the plume, which may be deconvolved [56] to yield the values of number density (in m^{-3}). Depending on the deconvolution method, numerical errors may be introduced: Lee's [56] results include negative values for the deconvolved number density. Thus for a more realistic comparison, the path-integrated number density values are analyzed instead. Since Monaco outputs number density values, additional processing is required to yield the line integrated values needed for the comparison.

Number density data is extracted from the plume solution along a radial line that starts at the axial coordinate of 0.031 m. This corresponds to the plane in which the CRDS measurements are recorded. Since the simulation is axisymmetric, the data extracted along the line may be copied in a circular pattern to reproduce the azimuthal plane flow-field. Next, the circular flow field is divided into a number of

lines that each mimic the CRDS interrogating laser beam. In the present case, 1000 such horizontal lines are defined in between the desired values of the dimensionless geometric parameter P. This variable is defined as:

$$P = \frac{r - r_{in}}{r_{out} - r_{in}} \qquad (4.21)$$

where r is the radial coordinate, r_{in} is the inner channel wall radius and r_{out} is the outer channel wall radius.

Finally, the number density values are integrated numerically along each one of the lines, using trapezoidal integration, to yield the values of path-integrated number density.

4.3 Simulation Results

4.3.1 Thruster Flow Field

The Monaco simulation output is presented in the form of contour plots of the number density, radial and axial components of the velocity. Moreover, in the velocity plots, streamlines are also shown to illustrate the direction of the flow through the computational domain. The contour plots for xenon flow properties are identical for both cases of boron wall interaction considered (sticking and reflecting from walls). Therefore, only one instance of these results is shown, in Fig. 4.4. Note that the mean free path for the thruster flow is on the order of 1 m, which is two orders of magnitude larger than the channel length and so there is very little interaction between the xenon and boron atoms within the thruster. The boron flow field results are compared side by side for the two different wall interaction cases, for each property, and discussed below.

Figure 4.4(a) shows the xenon number density in the simulation domain. Note these properties may be significantly different for actual thruster operation, since in the present simulation, plasma effects are neglected. The range of values is between 8.3×10^{16} and 1.2×10^{20} m^{-3}. A local maximum may be observed in the region between radial coordinates 0.025 and 0.030 m, and axial coordinates 0 and 0.004 m. This is due to the introduction of xenon particles from the inflow boundary condition, which is defined on the radial axis between the aforementioned coordinates.

Figure 4.4(b) displays a contour plot of the radial velocity values, whose range is between -192 and 323 m/s. It is observed that above the channel centerline, the velocity values are positive, and below they are negative, which is expected because of the expansion of the entering xenon gas particles. The trend is maintained at the thruster exit where another expansion occurs, showing more pronounced differences in the positive and negative values of the radial velocity.

The axial velocity contours for xenon are illustrated in Fig. 4.4(c). The range of values is between -13.6 and 328 m/s. Note that the thruster centerline serves as an axis of symmetry for the plot. Moreover, since most of the xenon atoms are traveling from left to right in this figure, the axial velocity values are positive, and the streamlines throughout the entire domain are all in the same direction: they start at the xenon inflow boundary and proceed towards the thruster exit.
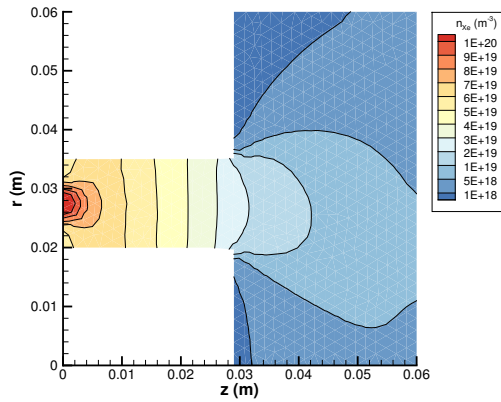
(a) Number density.
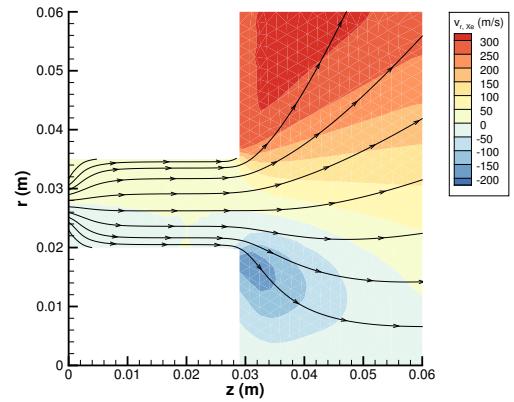
(b) Radial velocity.
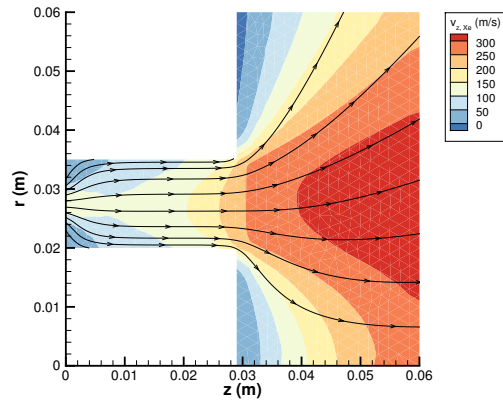
(c) Axial velocity.

Figure 4.4: Neutral xenon flow field contours from Monaco.

Figure 4.5 shows a comparison of the boron number density contours obtained in the two cases considered. In Fig. 4.5(a), where the walls are reflective, the range of values is between 6.8×10^{13} and 1.1×10^{16} m^{-3}. Within the thruster channel, the number density is relatively uniform, with a value larger than 5.0×10^{15} m^{-3}. As the particles exit the thruster, the number density decreases, as expected. In contrast, in Fig. 4.5(b), that results from the sticking case, the range of number density values is between 2.0×10^{13} and 5.0×10^{15} m^{-3}. Here there are two zones of high number density located on the walls, near the thruster exit, where the eroded boron atoms are introduced. Two regions of decreasing density are observed at the two ends of the thruster channel. On the anode side, the decrease occurs because boron particles are leaving the domain through the xenon inflow boundary type or sticking to the walls (which is equivalent to elimination from the domain). On the thruster exit side, the particles are expanding outside the thruster as in the non-sticking case.

Figure 4.6 presents contours of boron number density, from the azimuthal plane. The data shown is located 2 mm away from the exit plane, at the same location where the CRDS laser interrogates the plume. In Fig. 4.6(a) boron atoms reflect from thruster walls, and the range of number density values is between 9.3×10^{13} and 5.2×10^{15} m^{-3}, while in Fig. 4.6(b), where boron neutrals stick, the range is 3.4×10^{13} to 1.7×10^{15} m^{-3}. A ring of maximum number density is observed in the region corresponding to the channel exit for both cases, but clearly the number density values are much higher in the reflecting wall case, than the sticking wall simulation. The values then decrease both towards the center of the annular structure, and away from the center, however the absolute minimum is obtained in the outermost ring.

Figure 4.7 describes the radial velocity values throughout the domain. In Fig. 4.7(a), which corresponds to the reflecting wall case, the range is between -669 and 3630 m/s.

Inside the channel, zones of positive and negative radial velocity alternate. This is because the number of boron particles being eroded from the inner channel wall is greater than the number associated with the outer channel wall. Then, the particles are reflected back down, which explains the change in sign for the velocity. In Fig. 4.7(b), which represents the sticking walls case, the velocity range is -2325 to 8144 m/s. Higher velocity values are observed, as well as a different pattern. In the sticking wall case, the radial velocity values become positive on the outer channel wall except for the erosion region, because all the boron particles that travel in that direction are removed from the domain upon sticking to the wall. A similar explanation applies for the inner channel wall. In the wall reflection case, these particles return from the wall with a radial velocity of opposite sign than in the incident direction, which is why the velocity directions alternate more in Fig. 4.7(a).

The boron particle axial velocity contour plots are illustrated in Fig. 4.8. The range of values in Fig. 4.8(a), where boron atoms do not stick to the walls, is between -533 and 3596 m/s. For axial coordinate values smaller than 0.022 m, the axial velocities are all negative, because the boron atoms are moving towards the anode side, and exiting the domain through the xenon inflow boundary. On the other hand, to the right of the erosion boundary type, the axial velocity has strictly positive values, as the particles traveling through the thruster exit plane move towards the outflow boundaries, to exit the domain. These trends are best illustrated by the streamlines which start on the inner and outer channel walls, where the erosion boundary type is defined, and point either to the left or right sides of the figure, where the boron particles leave the simulation. However, when the boron particles stick to the wall, many streamlines going to the left simply terminate when they reach a wall. This is shown in Fig. 4.8(b), where the range of velocity values is -8132 to 9889 m/s.

Note that the streamlines in Figs. 4.7 and 4.8 diverge from the channel centerline. This suggests that a stream of particles leaves the thruster and follows a path that may lead the particles to deposit on spacecraft surfaces. Particle deposition can have detrimental effects on spacecraft performance. Material from the thruster plume may deposit on solar arrays that would reduce power generation, or if sufficiently high-energy particles are placed on this diverging path, they may erode the surfaces they come in contact with.

(a) Non-sticking walls.

(b) Sticking walls..
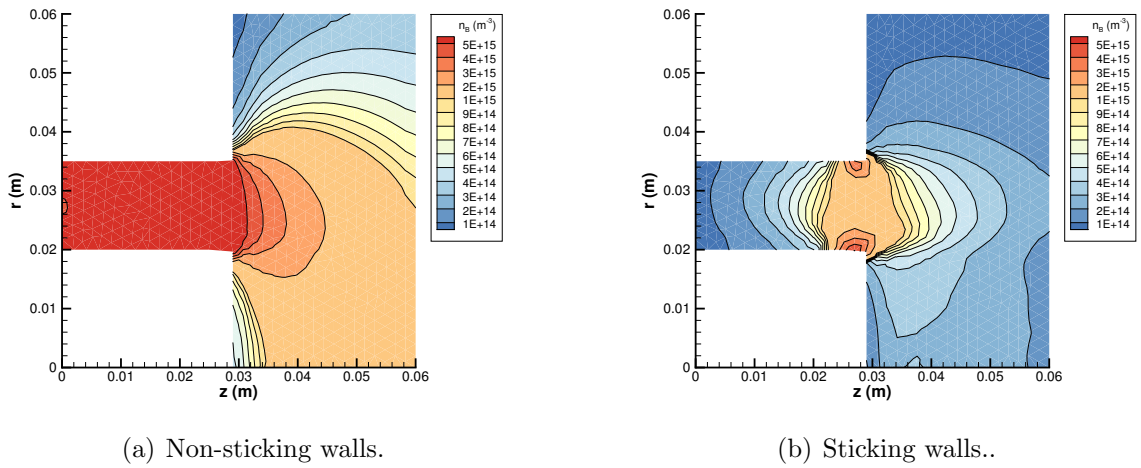
Figure 4.5: Boron number density contours from Monaco (r-z).

(a) Non-sticking walls.

(b) Sticking walls.
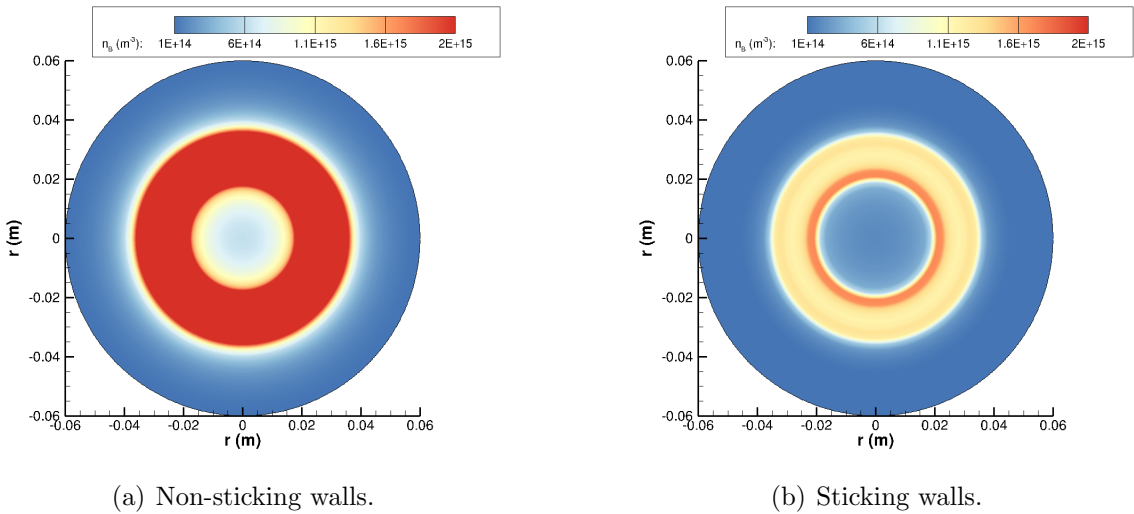
Figure 4.6: Boron number density contours in the azimuthal plane (r-θ), at an axial coordinate of 0.031 m from the anode (xenon injector).

74

(a) Non-sticking walls.

(b) Sticking walls..
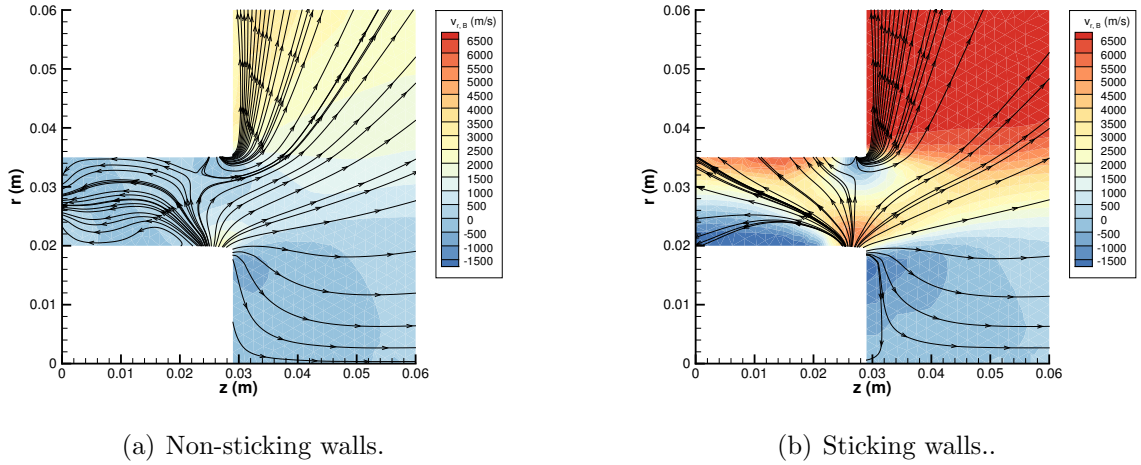
Figure 4.7: Boron radial velocity contours from Monaco (r-z).

(a) Non-sticking walls.

(b) Sticking walls..
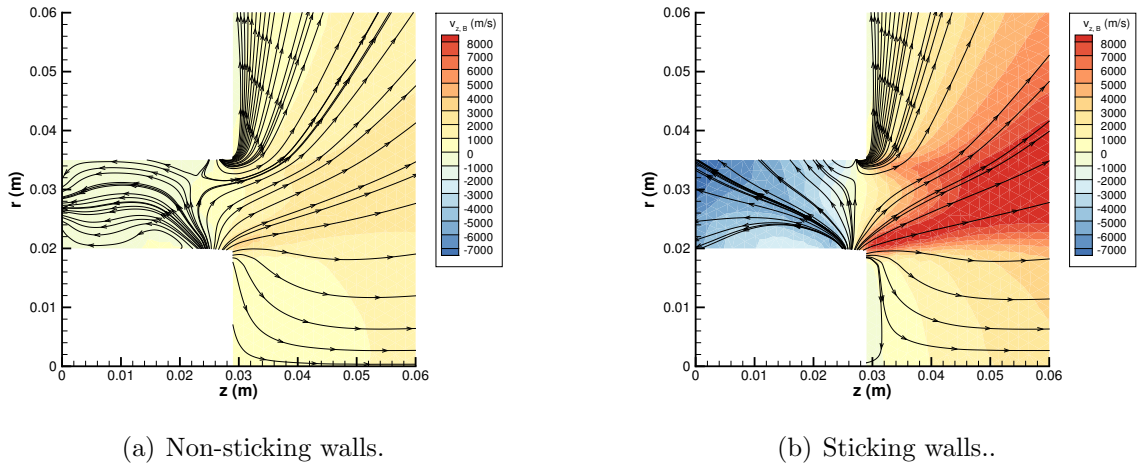
Figure 4.8: Boron axial velocity contours from Monaco (r-z).

4.3.2 Comparison with Experiment

CRDS is a line-of-sight absorption technique in which the directly measured quantity is the path-integrated concentration. In radially symmetric cases, the path-integrated boron number densities can be deconvolved to yield absolute number densities. Two common deconvolution techniques are Abel inversion and onion peeling, with the latter technique tending to reconstruct ring distributions more accurately

[16]. The results of deconvolving the CRDS data with the onion peeling technique have been presented in [56]. Given that all deconvolution techniques accentuate measurement noise, and to compare against directly measured experimental quantities, it is preferable to compare the path-integrated boron concentrations from CRDS and Monaco, as shown in Fig. 4.9.

Good qualitative agreement is observed for both the reflective and sticking walls: both data sets show an increase between $P = -1$ and $P = 0$ that leads to a peak between $P = 0$ and $P = 1$, followed by a steady decrease in the value of line-integrated number density. However, from Fig. 4.9(a) which shows the reflecting wall results, it is clear that the CRDS values are over an order of magnitude lower than those predicted by the Monaco simulation. As observed in Fig. 4.9(b), the simulation results obtained with sticking walls are significantly closer to the measured CRDS values. The number density values differ in magnitude by just a factor of three.

There are several plausible sources of the discrepancy. Since the experimental technique is only observing the electronic ground state boron atoms, atoms in excited electronic states as well as ions are excluded from the measurement. A first order approximate computation of the ionization fraction was performed by using the Saha equation (pp. 162-164 of Ref. [99]). The analysis showed that all of the boron neutrals should ionize. However, since the Saha equation is only applicable to equilibrium mixtures of ions, neutrals and electrons, which is certainly not the case in a SPT-70 HET, it is understood that not all boron atoms will be ionized. Nevertheless, the equilibrium calculation and its results suggest the potential significance that ionization may have. Smith [93] has pursued further HET erosion work, and included single ionization of boron and excitation of ground-state neutral boron to the ^{4}P metastable state. The conclusion from that work is that for Hall thrusters operating at 500 V

76

discharge voltage or less, almost all boron atoms that are sputtered from the walls in the neutral, ground state remain in the neutral, ground state as they travel through the thruster and plume. The SPT-70 was operated at 275 V and 300 V discharge voltage conditions in the laboratory, so it is expected that ionization and excitation of boron are in fact negligible effects.

Finally, uncertainties in some of the simulation input parameters may be affecting the Monaco results. These factors include the thruster operation time and sputtered boron VDFs, which affect the magnitudes of both the boron particle velocities and flux. In particular the thruster operation time has an uncertainty of 50% which is directly proportional to the estimated average erosion rate (Eq. 4.1).

(a) Non-sticking walls.

(b) Sticking walls..
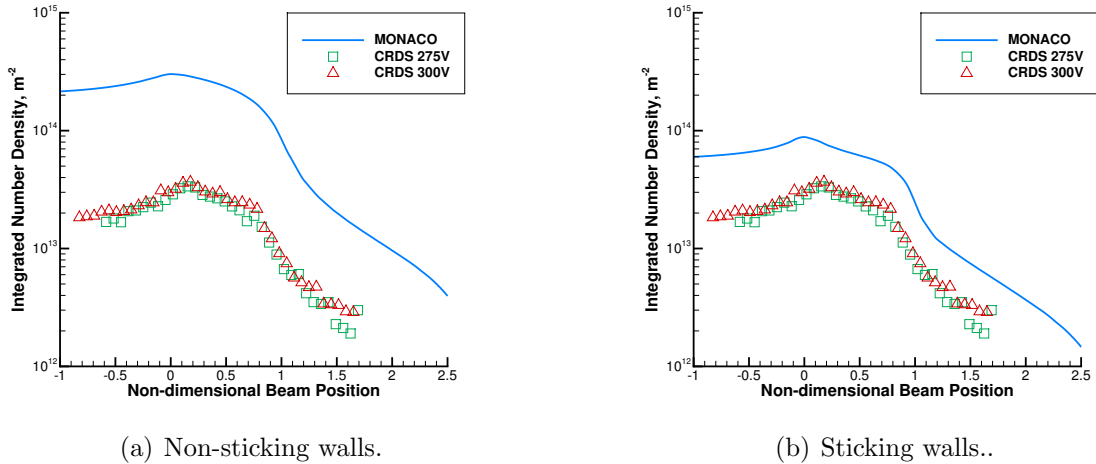
Figure 4.9: Comparison of line-integrated values of number density. The uncertainty in the CRDS measurements is included in the size of the symbols. For the 275 V case it is 8.1%, and for the 300 V case it is 9.3% [57].

4.4 Summary

Channel erosion is the main lifetime constraint for Hall thrusters. Determining the erosion rate may help with mission lifetime predictions, while providing a better

understanding of the erosion physics. A new CRDS diagnostic procedure was developed and tested recently [56] for the purpose of measuring path integrated boron number density. The goal was to use such measurements for more efficient and less costly thruster lifetime estimates. However, in order to make lifetime predictions, full knowledge of the flow field was necessary. Hence, a DSMC numerical simulation of the sputtered boron was performed, and the current chapter presented the setup and results obtained.

The sputtering process was modeled by using the eroded thruster geometry in the simulation, and introducing the boron particles with an appropriate particle flux and VDFs obtained from MD work in [90]. Hence, boron VDFs characteristic to the sputtering process were sampled to assign the velocities of the particles. Moreover, the number flux of boron atoms was computed based on the Sigmund-Thompson distribution which described the boron velocity component orthogonal to the eroding wall. An estimation of the volumetric erosion rate was carried out based on the current, eroded geometry of the thruster, and the approximate operation time.

Once the simulation produced flow field data for boron and xenon, additional processing was required in order to perform a comparison with the experimental measurements. Data was extracted from the boron number density field in the plane where the CRDS procedure was applied. Then, as an analog to the experimental laser interrogation of the flow field, the data was divided into an arbitrary number of lines (laser beams) over which the number density was integrated.

In the final analysis it was found that the DSMC simulation offered good qualitative agreement with the CRDS technique measurements, however the numerical values differed by an order of magnitude when the boron particles were reflecting from the

walls. Another simulation was performed where boron neutrals stick to the walls, upon contact, and the results from this case only differed in magnitude by a factor of three from the CRDS data. Several causes for the discrepancy were identified.

CHAPTER V

Nested Channel Hall Thrusters

5.1   Motivation

Nested channel Hall thrusters are a recent development in electric propulsion, and they are paving the way for higher power systems, such as the 100 kW X3 [32]. In addition to the classical questions related to the physics of single channel HETs, the mechanism and effects of channel interaction are new topics that have to be explored further in order to optimize the technology. In the present work, all modeling efforts are focused on a 10 kW class dual channel device, the X2 thruster.

Section 5.2 presents the results of a joint experimental and computational effort to characterize the effects of neutral ingestion on the nested channel thruster operation. The experimental work was performed by collaborators at the Plasmadynamics and Electric Propulsion Laboratory. The modeling work is focused on describing the near-field neutral xenon pressure distribution, and tracking the propellant which originates from the inner and outer channels during dual channel operation. The DSMC code Monaco is used (Section 2.2).

Section 5.3 presents the first plasma simulation of the X2, and is focused on the inner channel independent operation. The state-of-the-art hybrid-PIC code HPHall is used

(Section 2.3). This computational tool is evaluated by observing the effects of charge exchange collisions, number of particles, mobility parameters and electron temperature anisotropy ratio on the simulation results. For the baseline case, computed time averaged thrust and discharge current values match laboratory measurements to within 9% and 5%, respectively. The addition of charge exchange collisions or increasing the number of particles do not influence the time averaged results significantly. However, when the anomalous plume mobility parameter is varied, the thrust and discharge current change drastically, and in a non-monotonic way.

5.2   Neutral Simulations

In an effort to better understand the anomalous thrust gains observed by Liang [58] that were briefly described in Section 1.3.3, a computer simulation for neutral xenon atoms is prepared. The goal is to investigate the effects of the near-field pressure distribution on thrust.

5.2.1   Simulation Setup

The simulation of xenon neutral particles is performed using the computer code Monaco (Section 2.2). Although a single propellant gas is used in the simulation, two separate xenon species are defined, based on their origin. This enables the tracking of xenon particles injected in the inner and outer channels.

The inner channel mass flow rate is 88.5 sccm, while for the outer channel a value of 221.6 sccm is used. As described in Section 2.2, the Monaco inflow condition requires a number density value, so the flow rates are converted to number densities: 6.83×10^{19} (m^{-3}) for the inner channel and 7.00×10^{19} (m^{-3}) for the outer chan-

Table 5.1: Parameters for the Monaco simulation of the X2 dual channel operation.

Parameter		Value
n_{Xe}^{inner}	(m^{-3})	6.83×10^{19}
n_{Xe}^{outer}	(m^{-3})	7.00×10^{19}
Timestep	$(\mu\mathrm{s})$	3.8
Simulation time	(s)	0.76
Wall temperature	(K)	300
Inflow temperature	(K)	300
Number of particles		1,008,000
Particle weight		5.0×10^{10}

nel. The timestep, $\Delta t = 3.8$ μs, is chosen to ensure that particles spend several timesteps in each cell, allowing them to undergo collisions. The simulation is run for 200,000 timesteps, and an average total number of particles (xenon originating from both inner and outer channels) is 1,008,000 over the entire domain. Since the experimental measurement was performed for cold flow (no plasma), the wall temperature used here is 300 K. The simulation parameters are also summarized in Table 5.1.

Figure 5.1(b) shows the non-uniform triangular mesh that is employed, along with the boundary conditions. The final mesh is generated through iteration: an initial uniform mesh (Fig. 5.1(a)) is used in a first simulation to compute the mean free path over the entire domain. This initial mesh is then refined based on the computed particle mean-free-path to ensure an even distribution of computational particles within the domain. Specifically, regions with a larger mean-free-path (for example in the plume) may be discretized with more coarse cells than regions where there are many collisions, like inside the channel.

There are two inflow conditions (IN): one at the inner channel anode and one at the outer channel anode, a wall condition (WALL) that is implemented at the thruster channel walls, and a line of symmetry (SYM) is located on the south plume boundary.

The north and east domain boundaries enforce an outflow (OUT) condition which allows particles to leave the domain. Both axial and radial coordinates are normalized by the outer channel diameter, and the axial coordinate origin is set at the channel exit.

(a) Original mesh and Knudsen number.

(b) Refined mesh, and boundary conditions.
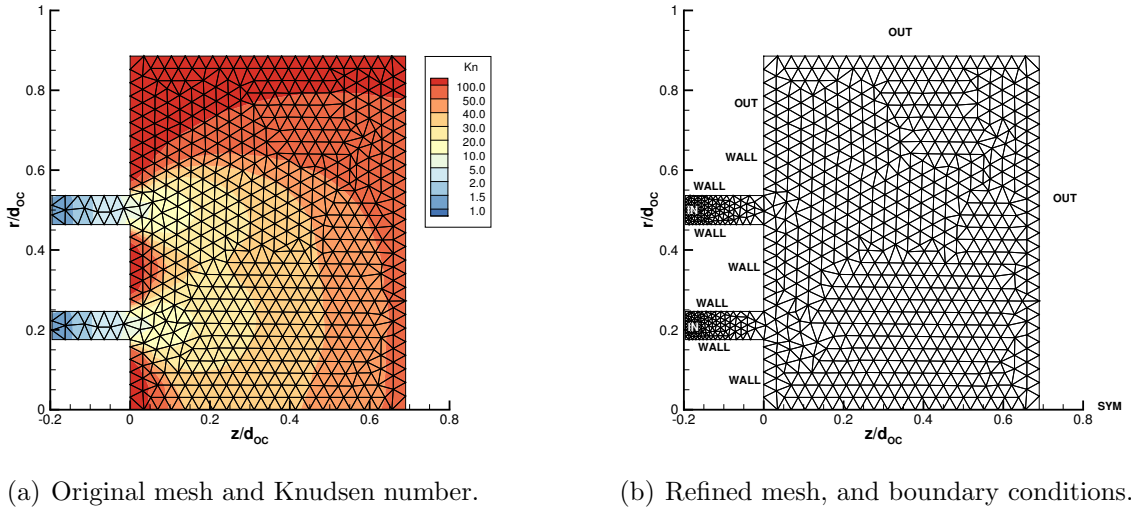
Figure 5.1: Computational domain for Monaco simulation.

5.2.2 Neutral Ingestion

Background neutral ingestion is a well documented facility effect observed during Hall thruster testing [101, 9, 72]. With a nested design, there is the opportunity for neutrals to diffuse from one channel to the other leading to higher values of thrust than one would expect. The DSMC model described in Section 5.2.1 is used to model neutral flow from the two channels and investigate the near-field pressure distribution.
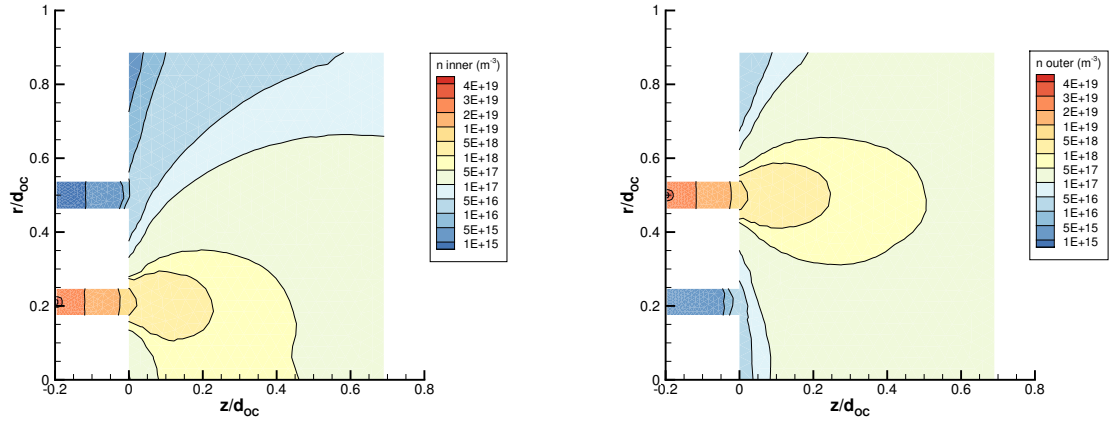
(a) Xenon originating in the inner channel.   (b) Xenon originating in the outer channel.

Figure 5.2: Number density of xenon propellant.

The number density distribution for xenon neutral particles diffusing through the computational domain is shown in Fig. 5.2. Figure 5.2(a) shows the density of xenon originating in the inner channel, which reaches a minimum value of 4.69×10^{14} m^{-3} in the near-anode region of the outer channel, and a maximum value of 4.24×10^{19} m^{-3} in the near-anode region of the inner channel. Next, Fig. 5.2(b) displays the density of gas originating in the outer channel, which follows similar trends: the maximum value of 4.32×10^{19} m^{-3} is near the outer channel injector, while the minimum, 1.23×10^{15} m^{-3}, is found near the inner channel anode.

Figure 5.3(a) shows the computed number density profiles from the simulation, extracted along the inner (blue) and outer (orange) channel centerlines. Both xenon species are represented on the plot: the solid lines show the inner channel particles, while the dashed lines represent the outer channel particles. Qualitatively, the number density profile is almost identical for both propellant species in the channel where they are introduced. However, the ingestion at the inner channel centerline with outer channel propellant is greater than that of the outer channel centerline with inner channel xenon. This is also observed in Fig. 5.3(b).

(a) Number density values.
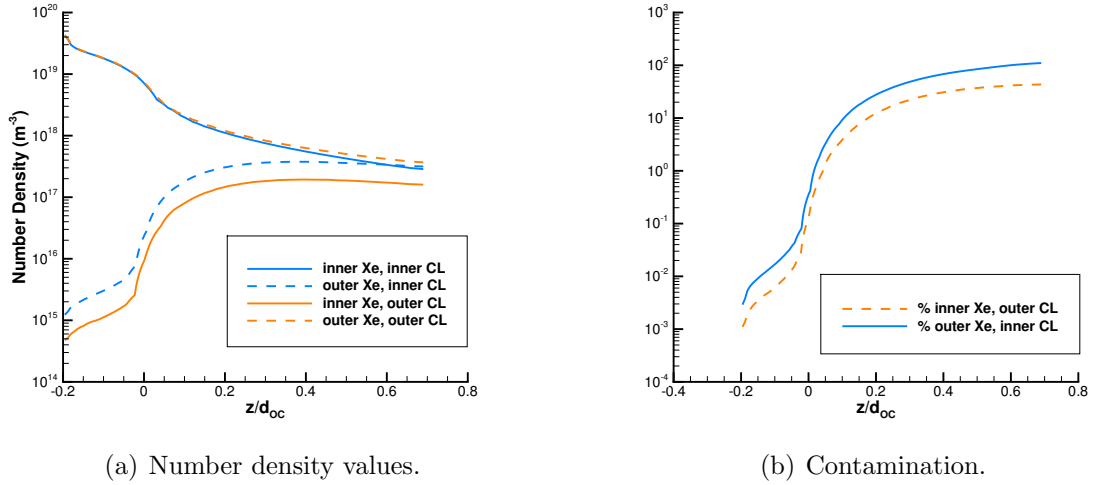
(b) Contamination.

Figure 5.3: The figure on the left shows number density data, while the figure on the right presents the percent contamination within a channel with particles from the other channel. Data values at the inner channel centerline are shown in blue, while orange is used for the outer channel centerline. Properties for xenon particles originating at the inner channel are plotted with solid lines, while the values for the outer channel are shown with dashed lines.

5.2.2.1 Local pressure profile

Experimental measurements carried out at PEPL [15] for cold flowing xenon from the radial sweeping of a Stabil-Ion Gauge in front of the thruster are shown in Fig. 5.4(a). Note that the ion gauge measures number density directly, and this is converted to pressure via the ideal gas law [50]:

$$p = nk_BT \tag{5.1}$$

In this case, the temperature used to convert number density to pressure is 400° C. The results indicate that with a base pressure measured inside the Large Vacuum Test Facility (LVTF) of 5.1×10^{-7} Torr-Xe the maximum pressure in dual-channel mode at axial location z=0.35 d_{OC} from the exit plane is 1.4×10^{-4} Torr-Xe, while

85

the maximum pressure with downstream injection is 8.7×10^{-5} Torr-Xe for both the inner and outer channels. The pressure profile for dual-channel mode qualitatively matches the sum of the single-channel test cases because the same flow is being injected into the chamber in the same locations. The total flow into the chamber when summing the two profiles is higher because of two effects that are included twice: the cathode flow and the background pressure. Therefore, the pressure magnitude is higher than in the dual channel case. The cathode flow is added twice because the center-mounted cathode is shared between the two channels. The background pressure is added twice because in both single channel cases we are matching the same background pressure by additional neutral injection; however, this effect is an order of magnitude smaller than that of the cathode flow. Since this measurement does not account for ionization, these results cannot definitively confirm the validity of this technique. However, they suggest that pressure from single channel modes can be approximately summed to compare to dual channel values. These data show that neutral density near the thruster is much higher in dual channel mode than in any of the two single channel modes even when the background pressure is the same.

Fig. 5.4(a) shows a comparison of measured and computed values of pressure. To insure consistency with the experimental procedure, the pressure from the DSMC results is computed similarly to the results obtained from the ion gauge. Thus the number density is converted to pressure by using the ideal gas law, and assuming a temperature value of 400° C. The simulation confirms, to order of magnitude, the experimental results. There are a few quantitative differences in the plots, such as the maximum magnitude for the outer channel profile. This can be reasonably explained by the consideration that the simulation data is tracking inner and outer particles separately for a dual channel condition. Conversely, the measured data show each channel individually and then operating together. There is no way to differentiate

(a) Experiment.
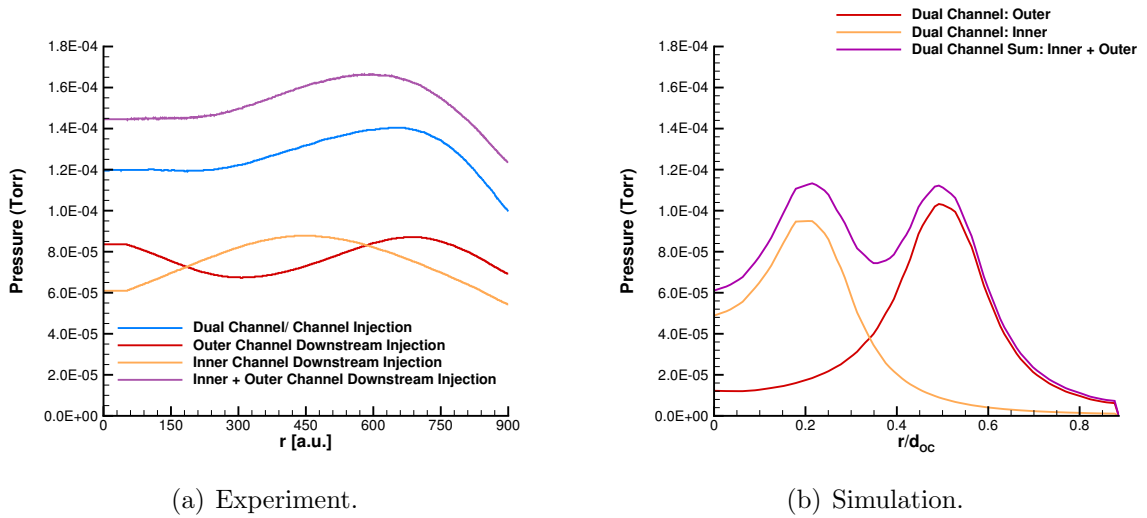
(b) Simulation.

Figure 5.4: Cold flow radial pressure maps from experiment (left) and simulation (right). The left figure shows the neutral pressure profile for single channel firing of the inner channel in yellow, single channel firing of the outer channel in red, and dual channel firing in blue. It also shows the summation of the two single channel conditions in purple. Numerical modeling results for dual channel neutral flow without back pressure are shown in the right figure, with labels based on the origin of the xenon species [15].

species coming from the inner channel versus the outer channel for dual channel experimental measurements. Additionally, there is the presence of the background pressure during experiments. Assuming that the xenon neutrals are at a temperature of 300 K since there is no plasma present to heat the neutrals, the density of the inner channel neutrals diffusing to the outer channel centerline (at z=0.35 d_{OC}) is calculated from the DSMC simulation to be 1.9×10^{17} m^{-3}, while the density of the outer channel neutrals diffusing to the inner channel centerline is 3.8×10^{17} m^{-3}. The typical ionization fraction in Hall thrusters is approximately 15% [39]; therefore, the neutral density near the channel would only be 85% of the calculated density. These values are used in the work by Cusson et. al. [15] to calculate thrust due to ingestion. When also taking into account the thrust changes due to divergence angle changes, the total thrust increase is calculated to be 10.7 ± 1.3 mN. This value has fully accounted for the measured dual-channel thrust increase within measurement uncertainty.

5.2.3 Summary

A neutral particle simulation was developed to compute the near-field pressure distributions, and number densities of xenon gas originating from the inner and outer channels of the X2 NHT. The pressure distributions were found to be in good qualitative agreement with the experimental measurements. Moreover, the number density values were used to estimate the increase in thrust due to neutral gas ingestion, and the thruster performance was accurately predicted within the uncertainty. This result suggests that local neutral ingestion is one of the dominant processes affecting nested Hall thruster performance. However, there are still other processes that could affect the performance to a lesser extent, such as plasma oscillations or cathode pressure gradients. Therefore, in the next Section a plasma simulation is prepared for the X2

thruster.

5.3   Plasma Simulations

The first step is to simulate the independent operation of the inner channel. The research goal is to explore the capabilities of the hybrid-PIC framework HPHall (Section 2.3) and sensitivity to numerical parameters. It is not possible to simulate the outer channel independent operation due to model limitations. Similarly, dual channel simulations which may be used to study the channel interaction cannot be performed with the original version of HPHall. The quasi-1D electron model cannot be used with the complicated X2 magnetic field topology which includes opposing radial components of the magnetic field in the two channels, and a separatrix region in the plume. The radial component of the magnetic field is plotted in Fig. 5.5, showing positive values in the inner channel region and negative values in the outer channel. Magnetic streamlines are also shown, and the separatrix region can be seen in the plume, between the two channels.
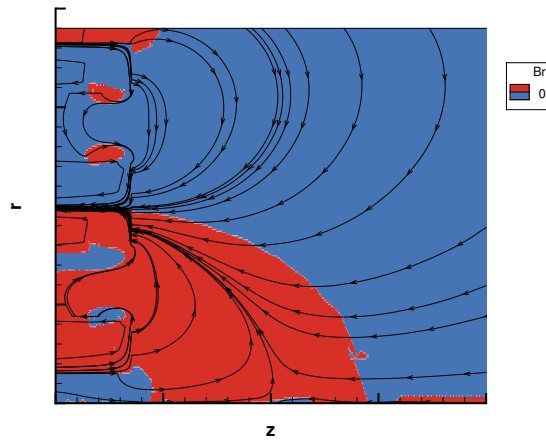
Figure 5.5: Radial component of the magnetic field changes sign between the inner and outer channels of the X2.

The simulation setup is explained in Section 5.3.1. Results from five sets of cases are shown in Section 5.3.3 and conclusions are presented in Section 5.3.4.

5.3.1 Simulation Setup

The thruster operating condition for the simulations is chosen based on the availability of experimental data. Since laboratory measurements for thrust, discharge current, electron temperature and plasma potential are available at $V_d = 200$ V and $\dot{m} = 75\%$ of nominal, the simulations are performed for this case.

HPHall is a serial code, and all simulations are ran in a Ubuntu 12.04 environment, on an Intel Xeon E5-1650 processor (12 cores at 3.2 GHz each). The code is compiled with GNU compilers. The magnetic field and computational mesh are presented in Section 5.3.1.1, the electron anomalous transport model is explained in Section 5.3.1.2, temperature anisotropy modeling is described in Section 5.3.1.3, and all the other significant computational parameters and physical effects are presented in Section 5.3.2.

5.3.1.1 Magnetic Field and Mesh

The magnetic field and mesh are generated independently in the pre-processing stage, using commercial software. The magnetic field is exported from Infolytica MagNet [47], and the structured elliptic mesh is built in Tecplot [96].

Figure 5.6(a) shows the 45×30 element computational mesh. Figure 5.6(b) shows the normalized magnitude of the magnetic field, along with magnetic field lines. Note that during laboratory testing [58] the magnets were tuned for each operating point,

so in order to simulate a different condition, the magnetic field input file needs to be updated.

Recall from Section 2.3.2 that in HPHall, the quasi-1D electron computational domain lies between the anode and cathode lambda lines, where the magnetic stream function lambda [24] is defined in Eq. 2.5.

The cathode potential is set at a point in the domain that lies on a lambda line which passes through the physical location of the cathode. This is the cathode lambda line. The X2 cathode is center mounted, and plasma potential data is available at the channel centerline. A value of 30 V was measured by Liang [58] with a floating emissive probe at the location indicated by a white circle in Fig. 5.6(b). The code uses a Dirichlet boundary condition for electron temperature at the cathode location, which is set to 1 eV.

Neutral xenon gas particles are injected through the anode at a flow rate of 7×10^{-6} kg/s with a temperature of 750 K [1] and a Mach number of 0 (free molecular flow with zero mean velocity). Similarly, Xe is added at the cathode location at a rate that is 10% of the anode flow, as reported by Liang [58]. Data for the X2 cathode was not available, but based on values used by Choi [14] for an H6 thruster cathode, neutrals are injected with a temperature of 823 K and Mach number of 0.6. Note that the internal cathode plasma is not modeled here. The cathode is simply a second neutral particle injector, similar to the anode.

(a) Computational mesh for PIC algorithm.

(b) Normalized magnetic field.
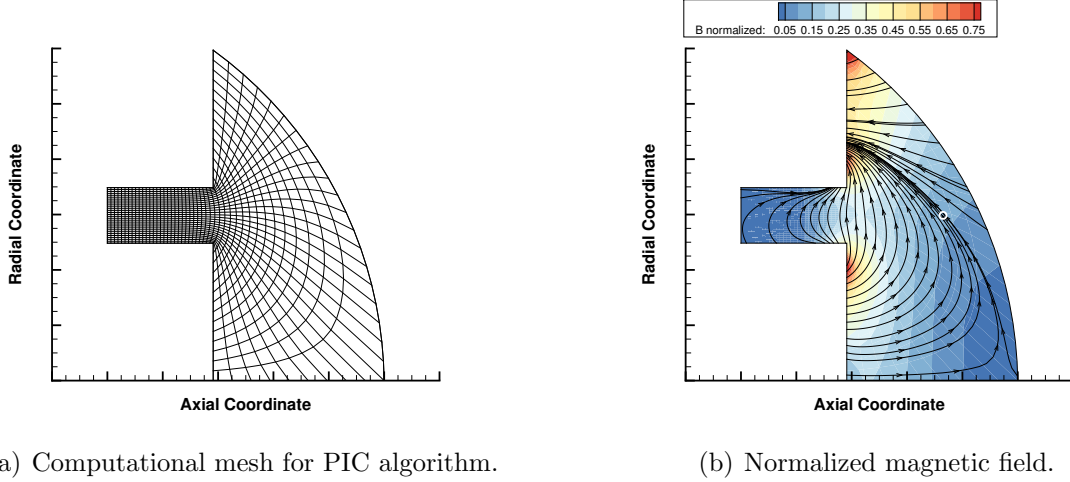
Figure 5.6: HPHall inputs generated with commercial software.

5.3.1.2 Electron Mobility

The version of HPHall used in this study employs a three-region mobility model, as described by Hofer [41]. This approach is an improvement from a single region model, which allows additional flexibility in selecting a mobility profile that more closely follows the measured anomalous mobility values in the discharge channel, exit plane and plume regions. The cross field mobility is defined as:

$$\mu_{e,\perp} = \frac{e}{\nu_e m_e} \left(\frac{1}{1 + \Omega_e^2} \right) \tag{5.2}$$

The total effective electron collision frequency is computed as the sum of the electron-neutral, electron-ion, wall and Bohm collision frequencies:

$$\nu_e = \nu_{en} + \nu_{ei} + \nu_w + \nu_b \tag{5.3}$$

The electron-neutral collision frequency is calculated as follows:

$$\nu_{en} = n_n \cdot Q_{en} \cdot \sqrt{\frac{8kT_e}{\pi m_e}} \tag{5.4}$$

where Q_{e-n} is the Maxwellian averaged cross-section of McEachran and Stauffer [63]. It is described by an analytical fit:

$$Q_{en} = \begin{cases} 7.55 \times 10^{-20}, & T_e < 1\text{eV} \\ 10^{-20} \cdot \left(\frac{94 \cdot \left(\frac{T_e}{2.21} - 0.364 \right)}{\left(1 + \left(\frac{T_e}{2.21} \right)^{1.7} \right)} + \frac{18T_e}{18 + T_e} \right), & T_e \geq 1\text{eV} \end{cases} \tag{5.5}$$

where T_e is in eV, and Q_{en} is in m^2.

The electron-ion collision frequency is computed as[45]:

$$\nu_{ei} = 2.91 \times 10^{-12} n_e T_e^{3/2} \ln \Lambda \tag{5.6}$$

where T_e is in eV and the Coulomb logarithm is:

$$\ln \Lambda = \begin{cases} 23 - \log \left(T_e^{-\frac{3}{2}} \sqrt{10^{-6} n_e} \right), & T_e \leq 10\text{eV} \\ 24 - \log \left(T_e^{-1} \sqrt{10^{-6} n_e} \right), & T_e > 10\text{eV} \end{cases} \tag{5.7}$$

The wall-collision frequency is defined as:

$$\nu_w(l, \chi) = \frac{\left[\left(\Delta A \frac{\delta_w}{1 - \delta_w} \Gamma_{brQ} \right)_{IW} + \left(\Delta A \frac{\delta_w}{1 - \delta_w} \Gamma_{brQ} \right)_{OW} \right]}{\Delta V(l) n_e(l, \chi)} \tag{5.8}$$

where l is the magnetic field line index, χ is the coordinate along the field line, ΔA and ΔV are area and volume elements centered on the field line, the subscripts IW and OW denote the inner and outer wall, δ_w is the secondary electron emission yield and Γ_{brQ} is the radial ion flux at the sheath edge.

Anomalous transport is modeled by including an adjustable coefficient, α that scales

the magnitude of the classical Bohm collision frequency:

$$\nu_b = \frac{1}{16}\alpha\omega_{ce} \qquad (5.9)$$

The boundaries of the three regions must be defined in relation to the thruster geometry, and values for the adjustable parameter α must be set in each region. Selecting these values involves an iterative procedure to ensure agreement with experimental data. Hofer [41] approached this problem by evaluating the Hall parameter from experimentally measured data, as shown in Fig. 5.7. This curve suggests how the three regions should be defined. In order to optimize the mobility coefficients, the plume mobility is first set to $\alpha = 1$, while the channel and exit coefficients are adjusted to match the discharge current. If necessary, the plume coefficient may then be adjusted to further improve the agreement with measurements.
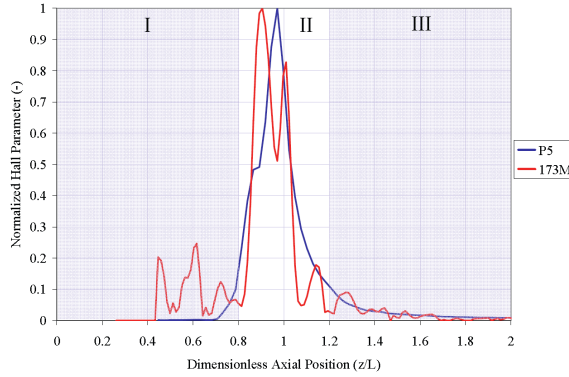
Figure 5.7: Hall parameter versus axial position computed from experimental data by Hofer [41]. The discharge channel exit plane is located at $z/L = 1$.

The simulations presented here follow a similar procedure. However, azimuthal and perpendicular values of current density [30] are not available, and therefore it is not possible to evaluate the Hall parameter based on measurements. Hence, the locations of the mobility regions are determined after multiple iterations. The dimensionless positions (axial coordinate over channel length) described by Hofer [41] are used as a

starting point. Adjustments are made iteratively, and the final region boundaries are selected based on the best match for simulation discharge current values compared to experiment. The mobility coefficients are selected similarly, and further discussion on this topic is provided in Section 5.3.3.4.

The final choices of Bohm region boundaries and coefficient values for the baseline case are summarized in Table 5.2. An interpolation is performed in the transition region to provide a smooth profile between mobility regions, but an abrupt transition may also be implemented. As shown in the second row, the start and end locations of the transition region may coincide.

Table 5.2: HPHall anomalous mobility parameters for the baseline X2 inner channel simulation.

Region	Start transition (z/L)	End transition (z/L)	Coefficient
channel	0.8	0.8	0.14
exit	0.8	1.13	0.07
plume	1.13	1.27	1.0

5.3.1.3   Temperature Anisotropy

Although the electron mobility has the most significant effect on thrust results, electron temperature anisotropy can also have a large influence. The quasi-1D electron model in HPHall [24] assumes that the electron temperature is constant along magnetic field lines, as described in Section 2.3.2.

Anisotropy is accounted for by including a correction for the electron temperature values used in the wall loss term, and Bohm speed computation, as shown in Eq. 5.10. A constant ratio of parallel to perpendicular temperatures is used throughout the entire domain, and for the simulations presented here the value is 0.86. The ef-

fects of this parameter on the simulation results are studied in Section 5.3.3.5.

$$T_e^{corrected} = \frac{T_{e,\parallel}}{T_{e,\perp}} T_e^{uncorrected} \tag{5.10}$$

5.3.2 Additional Parameters and Physics

The X2 thruster was tested in the LVTF at PEPL, and for the conditions of inter-est, Liang [58] reported a facility backpressure of 1.5×10^{-5} Torr. The backpressure effects are included in the simulation via neutral Xe injection at the outflow boundary of the domain at an assumed temperature of 300 K. For the present simulations, no significant changes are observed when compared to a vacuum test case.

However, to ensure that the model can capture these facility effects, a test case is prepared with a background pressure 20 times larger than that recorded in LVTF. A 17.3% increase in thrust and 17.8% increase in discharge voltage are observed when setting the backpressure to 3.11×10^{-4} Torr. The value corresponds to a neutral number density of 10^{19} m^{-3} which is on the order of the observed neutral density inside the thruster channel for the baseline simulation. This choice of backpressure is made to replicate neutral ingestion and observe changes in thrust and discharge current. The simulation outputs show a significant response, thus, in order to verify the thrust improvements observed by Liang in dual channel mode, it is important to include backpressure in the simulation.

The effect of CEX collisions between ions and neutrals is also studied. This process is modeled within HPHall as described by Parra [77].

In HPHall, the heavy species timestep is frozen while electron computations take

place. Thus, two different time increments are used. For stability, the electron timestep is set to a value of $O(10^3)$ smaller than the heavy species step. The timestep used for ions and neutrals, along with the spatial grid size are chosen to resolve gradients in the simulation.

The heavy species present in the simulations are xenon neutrals, singly charged, and doubly charged xenon ions. Smith [92] has added the capability to include triply charged ions, however it is not used for these simulations.

The total number of particles in the simulation varies both in time, and between the different cases studied. A comparison between the baseline and CEX simulations is reported in Section 5.3.3.2, and the effects of an increase in number of particles are investigated in Section 5.3.3.3.

The 812 K wall temperature value inside the channel is estimated based on thermocouple measurements performed on a SPT-100 thruster operating at similar power levels [1].

HPHall is run in three different stages. First, the domain is populated with neutrals, and this stage takes 20,000 timesteps. Next, ion particles are added for another 20,000 timesteps, but electron-ion collisions are turned off during this second stage. Finally, in the third stage, the ion-neutral and ion-ion collisions are activated, and this stage takes 80,000 timesteps (4 ms of physical time). Identical parameters are used for all three stages, with the exception of the electron time step which is adjusted to ensure stability. Table 5.3 summarizes the input parameter values.

Table 5.3: Input parameters for HPHall simulations of the Xe inner channel operation.

Parameter		Value
Propellant gas		Xe
Propellant flow rate at anode	(kg/s)	7×10^{-6}
Cathode flow rate	(kg/s)	7×10^{-7}
Facility backpressure	(Torr)	1.5×10^{-5}
Discharge voltage	(V)	200
Channel wall temperature	(K)	812
Heavy particle timestep	(s)	5×10^{-8}
Electron timestep	(s)	5×10^{-11}
Total simulation time	(ms)	4

5.3.3 Results

The effects of several simulation parameters and physical effects are studied. First, a baseline case is presented in Section 5.3.3.1. Next, CEX collisions are included in the simulation, and the observed differences are shown in Section 5.3.3.2. Further, two simulations similar to the baseline are run with higher total numbers of particles in Section 5.3.3.3. Sensitivity to the mobility coefficients is explored in Section 5.3.3.4. Finally, the effects of electron temperature anisotropy are investigated in Section 5.3.3.5. Unless otherwise noted, only one parameter is varied, while the others are kept the same as in the baseline case.

5.3.3.1 Baseline

Figure 5.8 shows contour maps of the number density of xenon neutral atoms (Fig. 5.8(a)) and singly charged xenon ions (Fig. 5.8(b)). Streamtraces are shown in both figures, and particles generally travel from higher to lower density regions. The two high density areas seen in the neutral plot correspond to the anode and cathode particle injection locations, while the high density area of the ion map is the ionization region.

Figures 5.9 and 5.10 illustrate the plasma potential and electron temperature from the simulation and show how these values compare to measurements [58] performed along the thruster centerline. The axial coordinate in the line plots is normalized with respect to the outer channel diameter of the X2. The normalized axial coordinate of 0 is located at the thruster exit. The simulation results are shown as the red line and the green squares indicate experimental values recorded during independent inner channel operation (IC).

A contour map of plasma potential is shown in Fig. 5.9(a). The potential decreases from 200 V to 30 V, as expected for the anode and cathode parameters used. As shown in Fig. 5.9(b), the decrease in potential matches the measurements very well. Figure 5.10(a) illustrates the distribution of electron temperature in the domain, with a peak near the thruster exit plane. The comparison with measurements shows that the peak is 2 eV higher and has a broader distribution in the simulation.

(a) Xe neutral atoms. (b) Xe$^+$ singly charged ions.
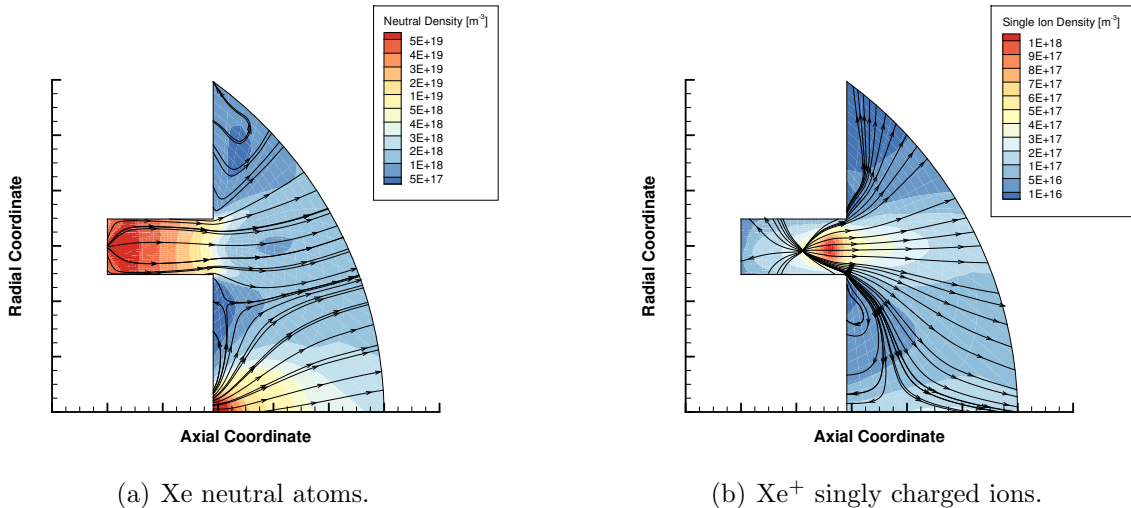
Figure 5.8: X2 inner channel time-averaged density contour maps from HPHall.
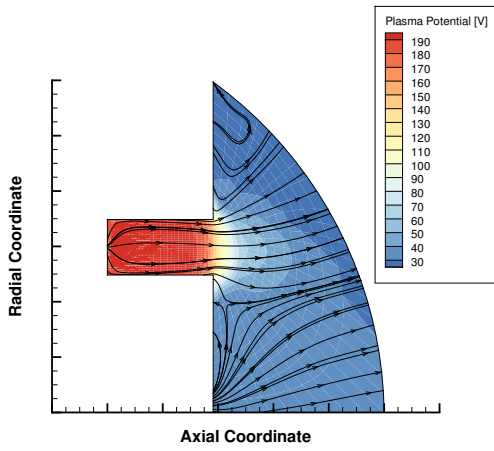
(a) Entire domain.
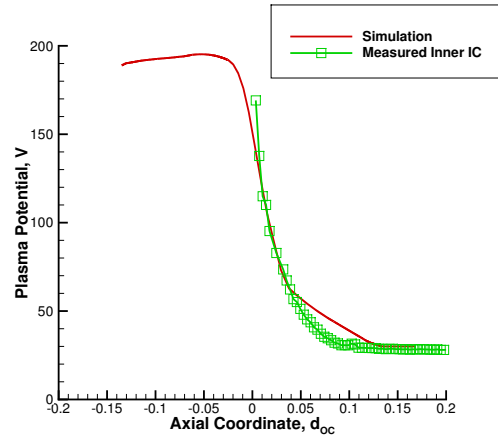
(b) Along inner channel centerline.

Figure 5.9: X2 inner channel time-averaged plasma potential from HPHall.
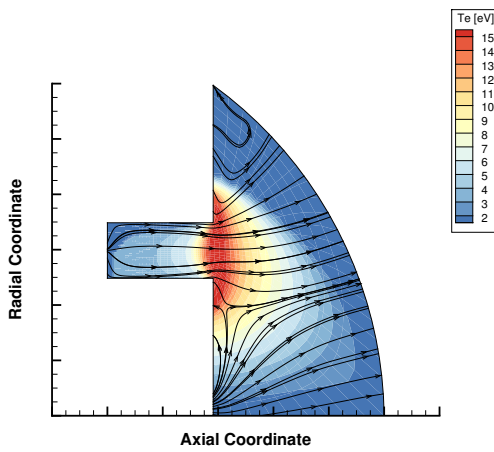
(a) Entire domain.
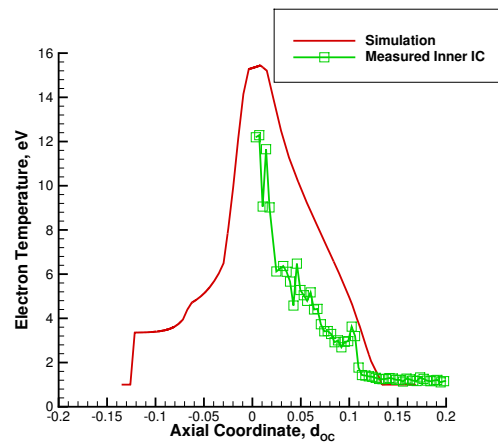
(b) Along inner channel centerline.

Figure 5.10: X2 inner channel time-averaged electron temperature from HPHall.

100

5.3.3.2 Effects of Charge Exchange

The plots shown for the baseline case in Section 5.3.3.1 remain largely unchanged after CEX collisions are included. This section will focus only on the differences that are observed.

Charge exchange collisions have an effect on neutral and ion velocities. This is expected, since during a CEX collision, a fast ion and a slow neutral will produce a slow neutral and a fast ion. We thus expect to see higher neutral velocities in the CEX case, and lower ion velocities. Figure 5.11 compares the ion velocity in the axial direction and it can be seen that the baseline case (Fig. 5.11(a)) shows a larger peak region than seen in the CEX simulation (Fig. 5.11(b)). A similar effect is observed for the radial ion velocity, in Fig. 5.12. However, the trend is reversed when considering the axial neutral velocity shown in Fig. 5.13. A region of high axial neutral velocity can be observed in the CEX results (Fig. 5.13(b)) which is not present in the baseline case (Fig. 5.13(a)). The addition of charge exchange appears to not have a significant effect on the radial component of the neutral velocity as seen in Fig. 5.14.

The addition of charge exchange also changes the time dependent simulation behavior. Figure 6.16 indicates that discharge current oscillations have a lower amplitude in the CEX simulation, and they do not exhibit a decaying behavior as seen in the initial 0.5 ms transient of Fig. 5.15(a). The initial transient occurs because the pre-conditioning first and second simulation stages produce different results for the baseline versus CEX cases.

The total number of neutral particles in the simulation reaches a saturation level in both cases, as shown in Fig. 5.16. However, this value is an order of magnitude higher in the CEX (Fig. 5.16(b)) case than the baseline (Fig. 5.16(a)). Since the dynamic

range is significantly larger, CEX produces a much smoother curve.

The total number of ion particles in the simulation fluctuates differently for the baseline and CEX cases, as seen in Fig. 5.17. The baseline Fig. 5.17(a) shows an initial increase in the mean value, while the CEX plot shows the opposite in Fig. 5.17(b).

(a) Baseline.

(b) With charge exchange collisions.
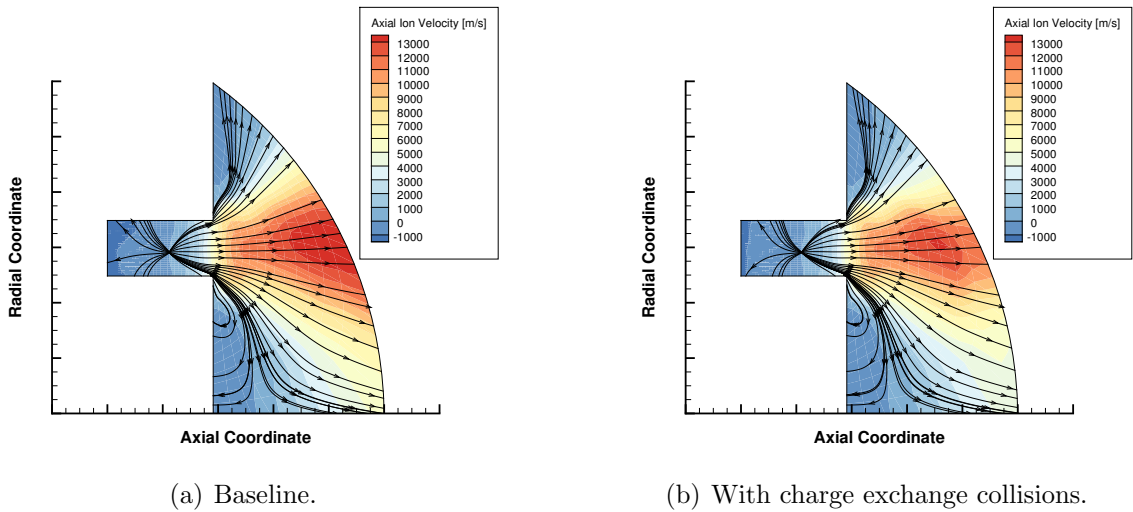
Figure 5.11: X2 inner channel time-averaged ion velocity in the axial direction from HPHall.

(a) Baseline.

(b) With charge exchange collisions.
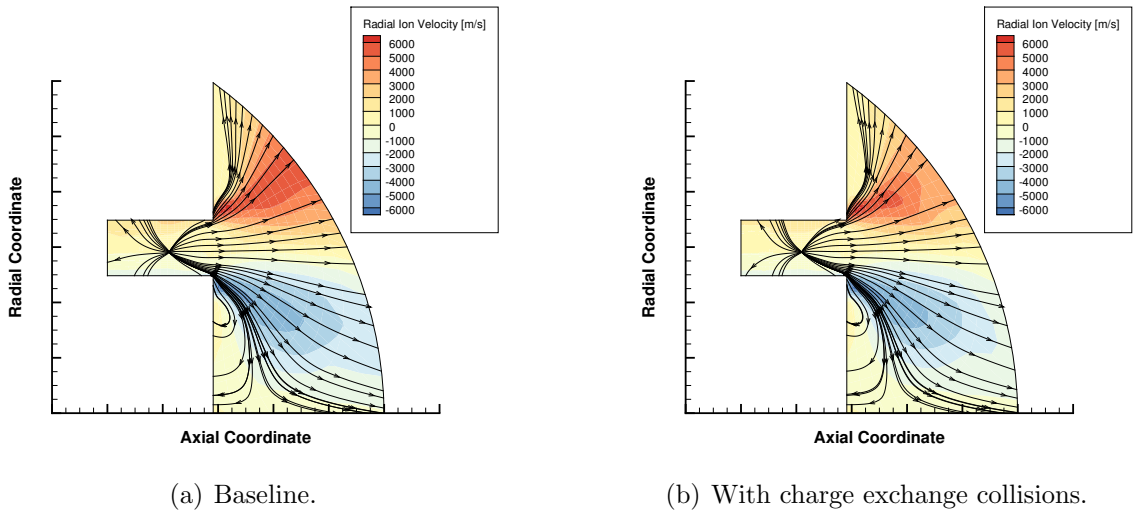
Figure 5.12: X2 inner channel time-averaged ion velocity in the radial direction from HPHall.
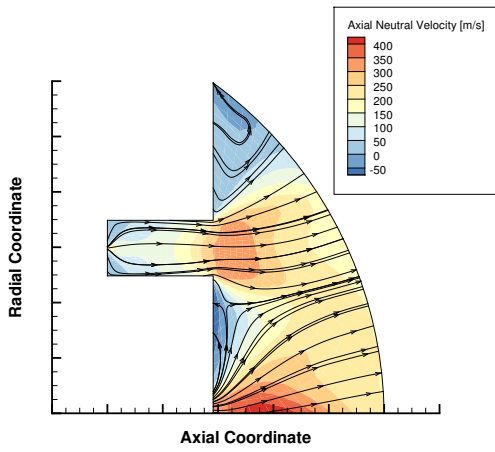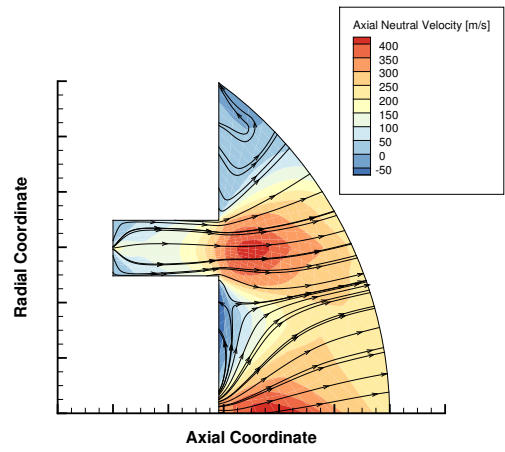
(a) Baseline.

(b) With charge exchange collisions.

Figure 5.13: X2 inner channel time-averaged neutral velocity in the axial direction from HPHall.
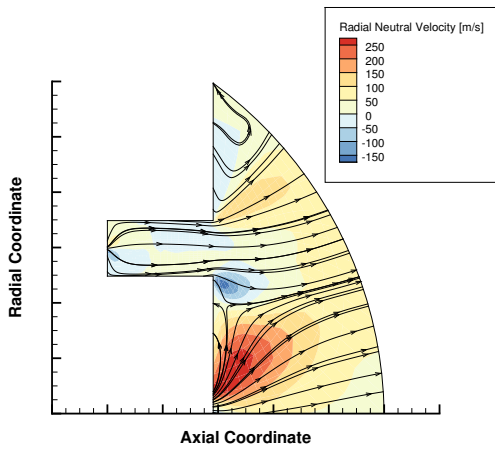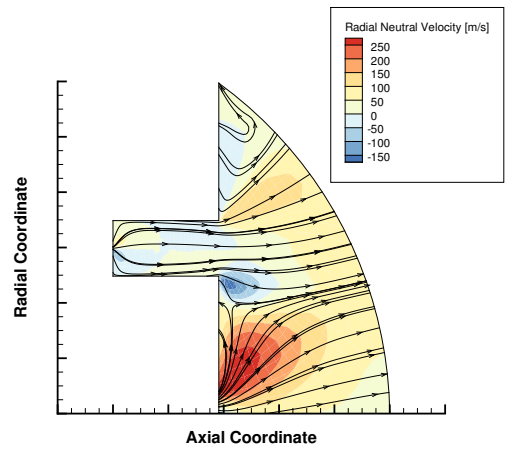
(a) Baseline.

(b) With charge exchange collisions.

Figure 5.14: X2 inner channel time-averaged neutral velocity in the radial direction from HPHall.
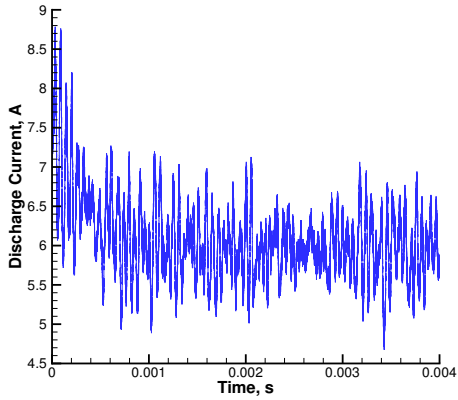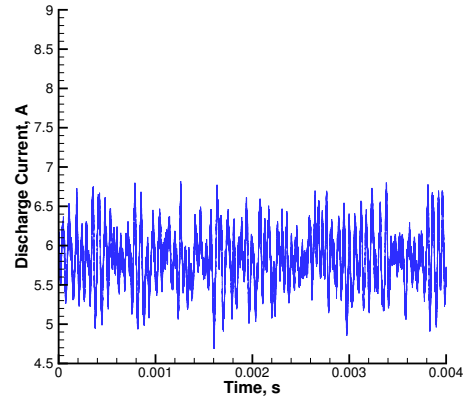
(a) Baseline.

(b) With charge exchange collisions.

Figure 5.15: Time evolution of discharge current.
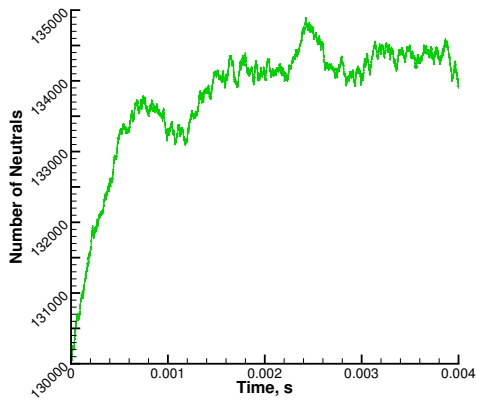
(a) Baseline.
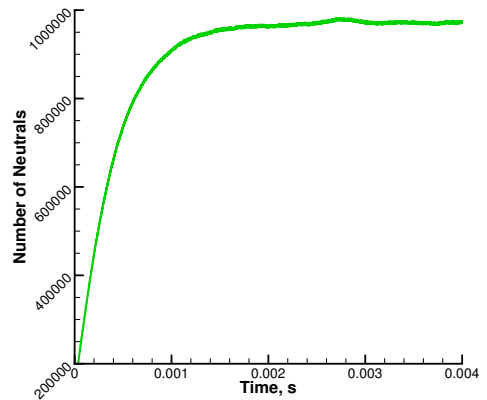
(b) With charge exchange collisions.

Figure 5.16: Time evolution of the total number of neutral particles.

104

(a) Baseline.

(b) With charge exchange collisions.
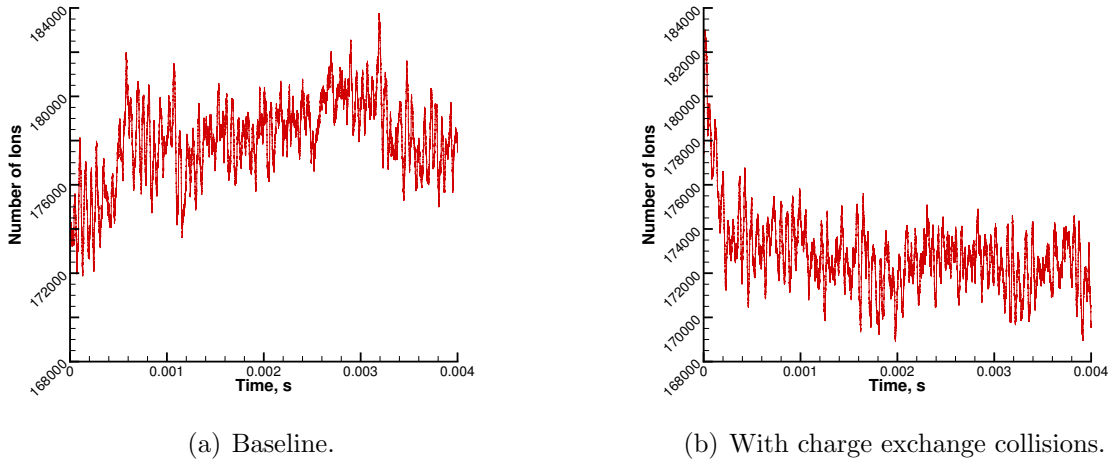
Figure 5.17: Time evolution of the total number of ion particles.

5.3.3.3 Increased Number of Particles

The differences in time dependent behavior between the baseline case and CEX simulation may be due to the large difference in the number of particles used in the two cases. Therefore, the baseline case simulation is run again, first with six (6x) and then with ten times (10x) more particles than the initial case. The time evolution of discharge current is shown in Fig. 5.18. The time dependent discharge current values for both 6x (Fig. 5.18(a)) and 10x (Fig. 5.18(b)) cases show lower noise levels when compared to the baseline and CEX cases from Fig. 6.16. This is expected because more particles in the PIC algorithm improve the accuracy of the heavy-species computation, and thus reduce numerical noise.

The total number of particles is compared for all four cases in Fig. 5.19. Figure 5.19(a) illustrates the variation in the total number of ions. The baseline and CEX curves are on the same order of magnitude, while for 6x and 10x the number of ions are approximately 6 and 10 times larger, respectively. Figure 5.19(b) shows how the total number of neutrals changes in time. All the baseline cases display a similar, and roughly constant behavior, with 6x and 10x cases producing 6 and 10 times more

particles respectively than the baseline. The number of ions in the CEX case starts at a similar value to the baseline, but keeps increasing for the first 0.0011 s until it reaches a steady state at approximately 960,000 particles.
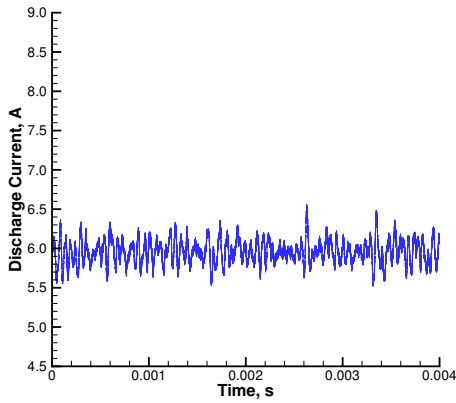
(a) 6 times more particles.
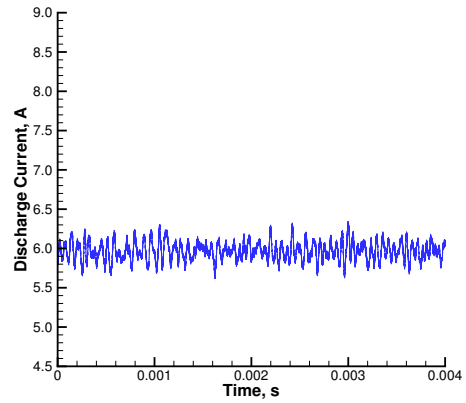
(b) 10 times more particles.

Figure 5.18: Time dependent discharge current. See Fig. 6.16 to compare with the baseline and charge exchange cases.
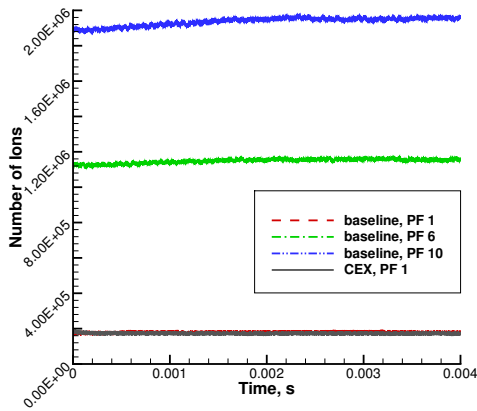
(a) 6 times more particles..
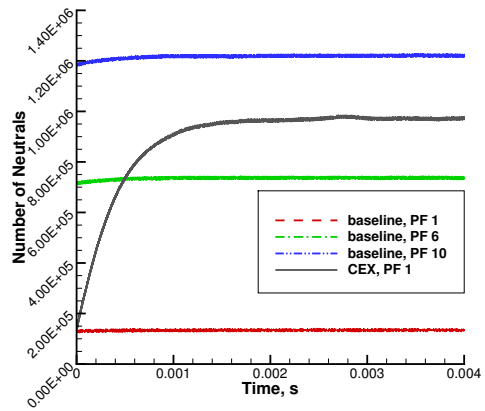
(b) 10 times more particles.

Figure 5.19: Comparison of total number of particles. The baseline and charge exchange cases use the same data as shown in Figs. 5.16 and 5.17.

Table 5.4 provides a summary of time averaged results from the four simulations, as well as laboratory data. The values shown in the last column are obtained from

Table 5.4: Time averaged results from HPHall simulations of the Xe inner channel operation.

Case	baseline	PF 6	PF 10	CEX	measured
Thrust (mN)	81.0	79.6	79.8	78.3	92.0 ± 3.00
Discharge current (A)	6.08	5.96	5.97	5.83	5.56 - 5.79
Electron current (A)	1.56	1.52	1.52	1.51	-
$\mathbf{Xe^{+1}}$ **current** (A)	4.09	4.02	4.03	3.91	-
$\mathbf{Xe^{+2}}$ **current** (A)	0.434	0.415	0.415	0.408	-
run time (hh:mm:ss)	09:39:23	50:42:21	82:11:04	28:22:02	-

Liang's [58] measurements. Although discharge current data was not reported directly, we extracted the current range from anode efficiency values provided in Liang's thesis. Note that the run time shown in the last column includes all three stages of the HPHall simulation.

The CEX case shows a decrease of 2.7 mN in total thrust from the baseline case. The time averaged values of currents also decreased by: 0.05 A for electrons, 0.18 A for singly charged ions and 0.026 A for doubly charged ions. However, the run time increased by approximately 17 hours. Overall, the addition of CEX improved agreement with experiment for the total discharge current, but reduced it for thrust.

The large number of particle simulations 6x and 10x agree very closely to each other for all observed quantities, so the baseline is only compared to the 6x case. A 1.4 mN decrease in thrust and 0.12 A decrease in total discharge current are observed. The electron current is 0.04 A lower, and singly and doubly charged ion currents are 0.07 A and 0.019 A lower, respectively. These simulations are significantly more expensive than the baseline case: the 6x case runs 5 times longer, while the 10x case runs 8 times longer.

5.3.3.4 Electron Mobility Coefficients

As described in Section 5.3.1.2, the mobility coefficients are selected through an iterative procedure to improve the match between computed discharge current and the measured value, which lies between 5.56 and 5.79 A [58].

Figure 5.20(b) shows how time averaged quantities vary with the choice of mobility coefficient for the channel exit region. Both the discharge current (Fig. 5.20(a)) and thrust (Fig. 5.20(b)) increase with higher values of the mobility parameter. Increased electron transport in this region leads to larger electric fields, and electron current. The higher electric field helps accelerate ions which leads to higher values of thrust. While the discharge current reaches the measured value for $\alpha = 0.065$, at this point the thrust is only 77.2 mN, which is 13.4 % lower than the measured 92 ± 3 mN. Further increasing the mobility parameter brings the computed thrust value higher, but it diminishes the agreement for discharge current. A compromise is made between matching the measurements for thrust and those for discharge current, and the mobility coefficient value of $\alpha = 0.07$ is chosen since it produces errors below 10% for both parameters.

It is observed that the time averaged discharge current and thrust do not vary monotonically with the plume mobility coefficient, unlike the channel exit coefficient. Therefore the parametric study of these quantities is performed at a larger particle factor (6x), to minimize the effects of noise. However, discharge current and thrust exhibit a similar behavior. As explained previously as we increase the electron mobility the electric fields and electron current also increase leading to higher values of I_d and thrust. Time averaged quantities are observed for coefficient values ranging between $\alpha = 1$ (classical Bohm mobility) and $\alpha = 43.75$. Discharge current is shown in Fig. 5.21(a) and thrust in Fig. 5.21(b). The behavior of both quantities is similar,
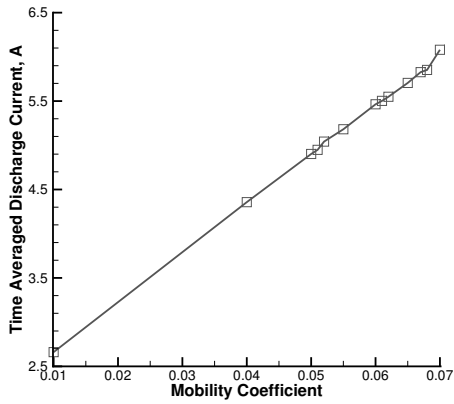
(a) Discharge current.
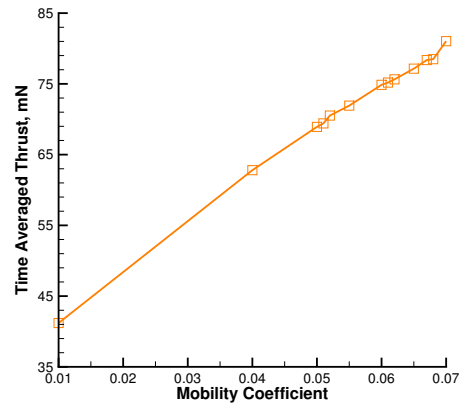
(b) Thrust.

Figure 5.20: Variation of time averaged quantities with mobility coefficient for the channel exit region (baseline). This corresponds to region II in Fig. 5.7.
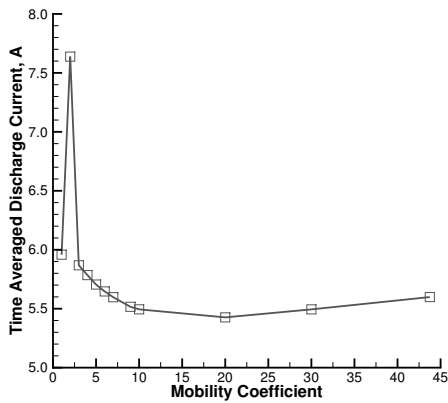
(a) Discharge current.
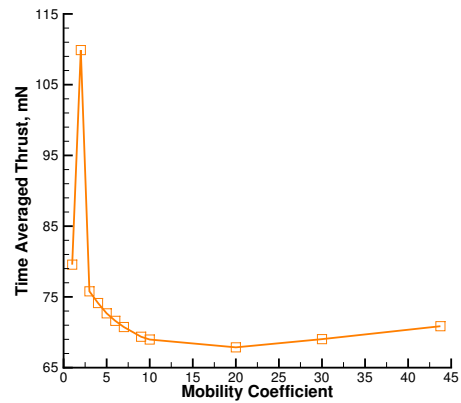
(b) Thrust.

Figure 5.21: Variation of time averaged quantities with mobility coefficient for the plume region (6x). This corresponds to region III in Fig. 5.7.

reaching the same maximum and minimum points. A coefficient value of $\alpha = 2$ produces a sharp increase in time averaged values: 30 mN (38.1%) for thrust and 1.68 A (28.2 %) for discharge current compared to $\alpha = 1$. Increasing the coefficient between $\alpha = 2$ and $\alpha = 10$ decreases the time averaged values, but the large coefficient value of $\alpha = 43.75$ produces an increase in thrust and discharge current. Since the plume coefficient does not yield a predictable behavior for the time averaged quantities, the initial value of $\alpha = 1$ is retained, pending future investigation.

5.3.3.5   Electron Temperature Anisotropy

Hara[34] suggests that temperature anisotropy may be accounted for by including the effects of azimuthal velocity in the energy balance, as shown in Eq. 5.11.

$$\epsilon = \frac{3}{2}T_e + KE_\theta = \frac{3}{2}T_e + \frac{\frac{1}{2}m_e v_\theta^2}{e} \tag{5.11}$$

The azimuthal velocity is computed from the $\vec{E} \times \vec{B}$ drift, and using the time-averaged axial and radial values available from HPHall, it may be written as in Eq. 5.12.

$$v_\theta = \frac{E_z B_r - E_r B_z}{B_r^2 + B_z^2} \tag{5.12}$$

Next, the anisotropy ratio may be computed as the ratio of the temperature derived from Eq. 5.11, and the actual value computed in the code. Based on this formulation, a map of effective temperature ratio parameter is constructed for the baseline case. Figure 5.22 shows that the electron temperature anisotropy ratio varies throughout the domain. In the region of high electron temperature, the computed ratio is between 0.89 and 0.95, compared to the 0.86 value that is used in the simulation. Therefore in

the future a dynamic way of computing the temperature ratio should be implemented, to account for the gradients observed in Fig. 5.22.
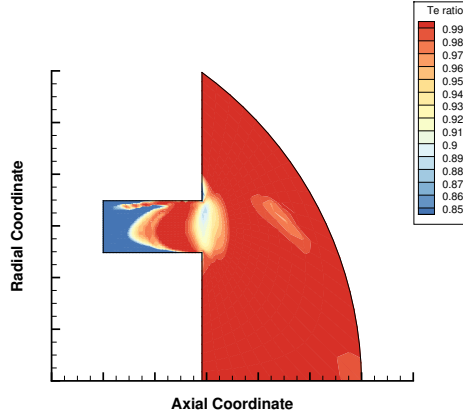
Figure 5.22: Estimate of electron temperature anisotropy ratio.

5.3.4   Summary

A first step in the simulation of a nested channel Hall effect thruster was presented. The numerical capabilities of HPHall were explored by including cathode neutral flow, neutral backpressure, observing simulation sensitivity to the mobility parameters, investigating the effects of charge exchange and analyzing the electron temperature anisotropy ratio.

The baseline case matched time averaged thrust and discharge current measurements to within 9% and 5%, respectively. In previous simulations, thrust has been matched to within the experimental error of 3.3 %. However, simultaneously matching the discharge current value is challenging because thrust tends to be lower than the measured value, while discharge current is higher. Simulations where the thrust is higher tend to also have higher discharge current values. This study shows the closest simultaneous agreement to X2 experimental data for both quantities, to date.

The inclusion of charge exchange collisions lowered the thrust and time averaged discharge current by 3.33% and 4.11%, respectively. The decrease occurred because a larger population of slow ions reached the boundary domain while faster neutrals remained near the channel exit. The CEX simulation results agreed with thrust measurements to within 14% and time averaged discharge current to within 0.7%. The current fractions for the baseline case were 0.904 for singly charged xenon ions and 0.095 for doubly charged ions. The addition of charge exchange did not make a significant impact on the current fractions, which were 0.905 and 0.094, respectively. However, the charge exchange simulation took approximately 3 times longer than the baseline case to complete, so the run time is expected to increase significantly for a larger numbers of particles.

Differences in the time dependent evolution of discharge current and number of neutral particles observed between the baseline and CEX simulation prompted new simulations with a larger number of particles: six and ten times more than the baseline. The two cases agreed well with each other. The 6x case showed a 1.7% decrease in thrust and 1.97% decrease in total discharge current when compared to the baseline case. The electron current was (1%) lower, and singly and doubly charged ion currents were 1.7% and 4.4% lower, respectively. The large particle factor cases were 5 and 8 times more expensive than the baseline simulation when using 6 times and 8 times more particles, respectively.

The HPHall time averaged outputs (thrust and discharge voltage) showed significant sensitivity to the mobility parameters. The addition of CEX collisions, and changes in number of particles had less of an effect on the simulation results, and major differences were observed only in the transient behavior. Additionally, it was shown that

the implementation of a constant electron temperature anisotropy ratio throughout the entire domain should be reconsidered.

Due to the complex magnetic field topology, the quasi-1D thermalized potential electron model used in HPHall is inadequate for studying the outer channel independent operation, or dual mode operation. Therefore, a two dimensional (axial-radial) axisymmetric electron model is developed and integrated within the HPHall framework, as described in Section VI.

CHAPTER VI

New 2D Axisymmetric Electron Fluid Model

6.1 Motivation

As described in Section 2.3, the hybrid-PIC approach can be very effective for modeling HETs with standard geometries and magnetic fields. However, recent developments in thruster design require updates to the computational tools available. In particular, the inherent limitations of the quasi-1D electron model pose significant barriers to modeling state-of-the-art devices, as discussed in Section 5.3.

Therefore, in this chapter a 2D axisymmetric fluid electron model is developed. Section 6.2 presents the governing equations, Section 6.3 describes the numerical discretization and Section 6.4 explains the boundary conditions. Next, Section 6.5 explains how the plasma potential and electron energy solvers are combined to form the standalone electron model. Section 6.6 shows how the model is verified, and finally, Section 6.7 describes the integration of the standalone electron model into the hybrid-PIC framework. Figure 6.1 shows how the different models become more complex through coupling, starting with the basic plasma potential and electron energy solvers and ending with the full hybrid-PIC model.
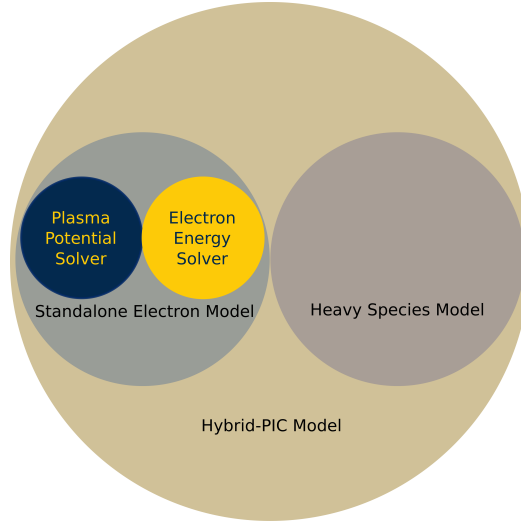
Figure 6.1: Integration of models.

6.2 Governing Equations

6.2.1 Momentum

The approach followed is to express the electron momentum equation as a generalized Ohm's law, and then combine it with charge conservation. This yields an equation that may be solved for the plasma potential.

The electron mobility, μ_e, and conductivity, σ, appear in the equations that follow, so they are both defined here:

$$\mu_e = \frac{e}{m_e \nu_e} \tag{6.1}$$

$$\sigma = n_e e \mu_e \tag{6.2}$$

We start with the momentum equation for electrons, as described in [29]:

$$m_e n_e \left[\frac{\partial \vec{v}_e}{\partial t} + (\vec{v}_e \cdot \nabla) \vec{v}_e \right] = q n_e \left(\vec{E} + \vec{v} \times \vec{B} \right) - \nabla \cdot \underline{\underline{P}}$$

$$- m_e n_e \left[\sum_i \nu_{ei} (\vec{v}_e - \vec{v}_i) + \nu_{en} (\vec{v}_e - \vec{v}_n) \right] \qquad (6.3)$$

Next, consider the electron flux:

$$\vec{\Gamma}_e = n_e \vec{v}_e \qquad (6.4)$$

And note that:

$$m_e n_e \nu \vec{v}_e = \frac{n_e e \vec{v}_e}{\mu} = \frac{e \vec{\Gamma}_e}{\mu}$$

Following the classical approximation [29] of negligible electron inertia, we set the convective derivative to 0 in Eq. 6.3. Introducing conductivity, we find the Generalized Ohm's law:

$$\vec{E} = -\frac{e \vec{\Gamma}_e}{\sigma} - \frac{e \vec{\Gamma}_e \times \vec{B}}{e n_e} - \frac{\nabla \cdot \underline{\underline{P}}}{e n_e} \qquad (6.5)$$

Assuming that the pressure tensor is isotropic, and applying the ideal gas law:

$$P = n_e k T_e [K] = n_e e T_e [eV] \qquad (6.6)$$

To facilitate future simplifications, introduce:

$$P = ep$$

$$p = n_e T_e$$

6.2.1.1 Derivation

Eq. 6.5 becomes:

$$\vec{E} = -\frac{e \vec{\Gamma}_e}{\sigma} - \frac{e \vec{\Gamma}_e \times \vec{B}}{e n_e} - \frac{\nabla \cdot (ep)}{e n_e} \qquad (6.7)$$

116

Multiplying Eq. 6.7 by the conductivity and rearranging, we find:

$$e\vec{\Gamma}_e = -\sigma\vec{E} - e\mu\vec{\Gamma}_e \times \vec{B} - e\mu\nabla \cdot p \tag{6.8}$$

Expressing Eq. 6.8 by components, we write:

$$\underline{z}: \qquad e\Gamma_{ez} = -\sigma E_z - \mu e(B_\theta\Gamma_{er} - B_r\Gamma_{e\theta}) - e\mu\frac{\partial p}{\partial z} \tag{6.9}$$

$$\underline{r}: \qquad e\Gamma_{er} = -\sigma E_r - \mu e(B_z\Gamma_{e\theta} - B_\theta\Gamma_{ez}) - e\mu\frac{\partial p}{\partial r} \tag{6.10}$$

$$\underline{\theta}: \qquad e\Gamma_{e\theta} = -\sigma E_\theta - \mu e(B_r\Gamma_{ez} - B_z\Gamma_{er}) - e\mu\frac{1}{r}\frac{\partial p}{\partial \theta} \tag{6.11}$$

We assume azimuthal symmetry and set $E_\theta = 0$ and $\frac{\partial p}{\partial \theta} = 0$. Eq. 6.11 then becomes:

$$\Gamma_{e\theta} = -\mu(B_r\Gamma_{ez} - B_z\Gamma_{er}) \tag{6.12}$$

Using Eq. 6.12 into Eqs. 6.9 and 6.10 we get:

$$\underline{z}: e\Gamma_{ez} = -\sigma E_z - \mu e\left[B_\theta\Gamma_{er} + B_r\mu(B_r\Gamma_{ez} - B_z\Gamma_{er}\right] - e\mu\frac{\partial p}{\partial z} \tag{6.13}$$

$$\underline{r}: e\Gamma_{er} = -\sigma E_r - \mu e\left[-B_z\mu(B_r\Gamma_{ez} - B_z\Gamma_{er}) - B_\theta\Gamma_{ez}\right] - e\mu\frac{\partial p}{\partial r} \tag{6.14}$$

From Eq. 6.14, the radial flux can be expressed in terms of the axial flux:

$$e\Gamma_{er} = \frac{-\sigma E_r - e\mu\frac{\partial p}{\partial r} + e\Gamma_{ez}(\mu^2 B_r B_z + \mu B_\theta)}{1 + \mu^2 B_z^2} \tag{6.15}$$

Similarly, from Eq. 6.13 the axial flux can be written as:

$$e\Gamma_{ez} = \frac{-\sigma E_z - e\mu\frac{\partial p}{\partial z} + e\Gamma_{er}(\mu^2 B_r B_z - \mu B_\theta)}{1 + \mu^2 B_r^2} \tag{6.16}$$

Then, using Eq. 6.15 into Eq. 6.13 we can solve for the axial flux:

$$e\Gamma_{ez} = \left(\frac{1 + \mu^2 B_z^2}{1 + \mu^2(B_r^2 + B_z^2 + B_\theta^2)}\right)\left(-\sigma E_z - e\mu\frac{\partial p}{\partial z}\right)$$
$$+ \left(\frac{-\mu B_\theta + \mu^2 B_r B_z}{1 + \mu^2(B_r^2 + B_z^2 + B_\theta^2)}\right)\left(-\sigma E_r - e\mu\frac{\partial p}{\partial r}\right) \tag{6.17}$$

Using the expression for axial flux from Eq. 6.17, we return to Eq. 6.15 and express the radial flux as:

$$e\Gamma_{er} = \left(\frac{\mu^2 B_r B_z + \mu B_\theta}{1 + \mu^2(B_r^2 + B_z^2 + B_\theta^2)}\right)\left(-\sigma E_z - e\mu\frac{\partial p}{\partial z}\right)$$
$$+ \left(\frac{1 + \mu^2 B_r^2}{1 + \mu(B_r^2 + B_z^2 + B_\theta^2)}\right)\left(-\sigma E_r - e\mu\frac{\partial p}{\partial r}\right) \tag{6.18}$$

Next we define the mobility coefficients:

$$coef_{zz} = \frac{1 + \mu^2 B_z^2}{1 + \mu^2 B^2}$$
$$coef_{zr} = \frac{\mu^2 B_z B_r - \mu B_\theta}{1 + \mu^2 B^2}$$
$$coef_{rz} = \frac{\mu^2 B_z B_r + \mu B_\theta}{1 + \mu^2 B^2}$$
$$coef_{rr} = \frac{1 + \mu^2 B_r^2}{1 + \mu^2 B^2}$$
$$coef_{perp} = \frac{1}{1 + \mu^2 B^2} \tag{6.19}$$

The axial and radial fluxes in Eqs. 6.17 and 6.18 can be written in a more compact way as:

$$e\Gamma_{ez} = coef_{zz}(-n_e e\mu E_z - e\mu\frac{\partial p}{\partial z}) + coef_{zr}(-n_e e\mu E_r - e\mu\frac{\partial p}{\partial r}) \tag{6.20}$$
$$e\Gamma_{er} = coef_{rz}(-n_e e\mu E_z - e\mu\frac{\partial p}{\partial z}) + coef_{rr}(-n_e e\mu E_r - e\mu\frac{\partial p}{\partial r}) \tag{6.21}$$

Further define:

$$\mu_{zz} = -\left(coef_{zz}\right)\mu$$

$$\mu_{zr} = -\left(coef_{zr}\right)\mu$$

$$\mu_{rz} = -\left(coef_{rz}\right)\mu$$

$$\mu_{rr} = -\left(coef_{rr}\right)\mu$$

$$\mu_{perp} = -\left(coef_{perp}\right)\mu \tag{6.22}$$

Finally, by components, the momentum equation becomes:

$$\Gamma_{e,z} = n_e\mu_{zz}E_z + n_e\mu_{zr}E_r + \mu_{zz}\frac{\partial p}{\partial z} + \mu_{zr}\frac{\partial p}{\partial r} \tag{6.23}$$

$$\Gamma_{e,r} = n_e\mu_{rz}E_z + n_e\mu_{rr}E_r + \mu_{rz}\frac{\partial p}{\partial z} + \mu_{rr}\frac{\partial p}{\partial r} \tag{6.24}$$

6.2.1.2 Charge conservation

The ion and electron charge conservation equations can be written as:

$$\frac{\partial n_i}{\partial t} + \nabla \cdot \vec{\Gamma}_i = S_i \tag{6.25}$$

$$\frac{\partial n_e}{\partial t} + \nabla \cdot \vec{\Gamma}_e = S_e \tag{6.26}$$

where S_e and S_i are the electron and ion source terms, respectively.

Next we assume quasi-neutrality, $n_e = n_i$, and identical source terms for electrons and ions: $S_e = S_i$. We obtain:

$$\nabla \cdot \left(\vec{\Gamma}_i - \vec{\Gamma}_e\right) = 0 \tag{6.27}$$

Since the formulation is axisymmetric, we expand for cylindrical coordinates (Ap-

pendix B):

$$\frac{\partial \Gamma_{e,r}}{\partial r} + \frac{\partial \Gamma_{e,z}}{\partial z} + \frac{\Gamma_{e,r}}{r} = \frac{\partial \Gamma_{i,r}}{\partial r} + \frac{\partial \Gamma_{i,z}}{\partial z} + \frac{\Gamma_{i,r}}{r} \qquad (6.28)$$

6.2.1.3   Master Equation for Momentum

Using the flux expressions (Eqs. 6.23 and 6.24) derived from the generalized Ohm's law into the charge conservation statement from Eq. 6.28 and noting $j_i = e\Gamma_i$, while $j_e = -e\Gamma_e$, we obtain:

$$\frac{\partial}{\partial r}\left(n_e\mu_{rz}E_z + n_e\mu_{rr}E_r + \mu_{rz}\frac{\partial p}{\partial z} + \mu_{rr}\frac{\partial p}{\partial r}\right) +$$
$$\frac{\partial}{\partial z}\left(n_e\mu_{zz}E_z + n_e\mu_{zr}E_r + \mu_{zz}\frac{\partial p}{\partial z} + \mu_{zr}\frac{\partial p}{\partial r}\right) +$$
$$\frac{1}{r}\left(n_e\mu_{rz}E_z + n_e\mu_{rr}E_r + \mu_{rz}\frac{\partial p}{\partial z} + \mu_{rr}\frac{\partial p}{\partial r}\right) =$$
$$\frac{1}{e}\left(\frac{\partial j_{i,r}}{\partial r} + \frac{\partial j_{i,z}}{\partial z} + \frac{j_{i,r}}{r}\right) \qquad (6.29)$$

Recall $\vec{E} = -\nabla\phi$:

$$-\frac{\partial}{\partial z}\left(n_e\mu_{zz}\frac{\partial\phi}{\partial z} + n_e\mu_{zr}\frac{\partial\phi}{\partial r}\right) - \frac{\partial}{\partial r}\left(n_e\mu_{rz}\frac{\partial\phi}{\partial z} + n_e\mu_{rr}\frac{\partial\phi}{\partial r}\right) -$$
$$-\frac{1}{r}\left(n_e\mu_{zr}\frac{\partial\phi}{\partial z} + n_e\mu_{rr}\frac{\partial\phi}{\partial r}\right) +$$
$$+\frac{\partial}{\partial z}\left(\mu_{zz}\frac{\partial p}{\partial z} + \mu_{zr}\frac{\partial p}{\partial r}\right) + \frac{\partial}{\partial r}\left(\mu_{rz}\frac{\partial p}{\partial z} + \mu_{rr}\frac{\partial p}{\partial r}\right) +$$
$$+\frac{1}{r}\left(\mu_{rz}\frac{\partial p}{\partial z} + \mu_{rr}\frac{\partial p}{\partial r}\right) =$$
$$=\frac{1}{e}\left(\frac{\partial j_{i,r}}{\partial r} + \frac{\partial j_{i,z}}{\partial z} + \frac{j_{i,r}}{r}\right) \qquad (6.30)$$

The steps followed to reach Equation 6.30 may also be written in tensor form as

follows:

$$\nabla \cdot \vec{\Gamma}_i = \nabla \cdot \vec{\Gamma}_e$$

$$= \nabla \cdot \begin{bmatrix} \Gamma_{e,z} \\ \Gamma_{e,r} \\ 0 \end{bmatrix}$$

$$= \nabla \cdot \left\{ \begin{bmatrix} \mu_{zz} & \mu_{zr} & 0 \\ \mu_{rz} & \mu rr & 0 \\ 0 & 0 & 0 \end{bmatrix} \cdot \begin{bmatrix} -n_e \frac{\partial \phi}{\partial z} + \frac{\partial}{\partial z} \\ -n_e \frac{\partial \phi}{\partial r} + \frac{\partial}{\partial r} \\ 0 \end{bmatrix} \right\}$$

$$= \nabla \cdot \left\{ \underline{\underline{\mu}} \cdot \begin{bmatrix} -n_e \frac{\partial \phi}{\partial z} + \frac{\partial}{\partial z} \\ -n_e \frac{\partial \phi}{\partial r} + \frac{\partial}{\partial r} \\ 0 \end{bmatrix} \right\} \qquad (6.31)$$

For ease of notation, we rewrite Eq. 6.30, and define a new left hand side (LHS) and right hand side (RHS):

$$LHS = \frac{\partial}{\partial z} \left(n_e \mu_{zz} \frac{\partial \phi}{\partial z} + n_e \mu_{zr} \frac{\partial \phi}{\partial r} \right) + \frac{\partial}{\partial r} \left(n_e \mu_{rz} \frac{\partial \phi}{\partial z} + n_e \mu_{rr} \frac{\partial \phi}{\partial r} \right)$$
$$+ \left(\frac{n_e \mu_{rz} \frac{\partial \phi}{\partial z} + n_e \mu_{rr} \frac{\partial \phi}{\partial r}}{r} \right)$$

$$RHS = \frac{\partial}{\partial z} \left(\mu_{zz} \frac{\partial p}{\partial z} + \mu_{zr} \frac{\partial p}{\partial r} \right) + \frac{\partial}{\partial r} \left(\mu_{rz} \frac{\partial p}{\partial z} + \mu_{rr} \frac{\partial p}{\partial r} \right)$$
$$+ \frac{\mu_{rz} \frac{\partial p}{\partial z} + \mu_{rr} \frac{\partial p}{\partial r}}{r} - \frac{1}{e} \left(\frac{\partial j_{i,r}}{\partial r} + \frac{\partial j_{i,z}}{\partial z} + \frac{j_{i,r}}{r} \right)$$

6.2.2   Energy

We start with the energy equation in vector form ([66], [29]):

$$\frac{3}{2}en_e\frac{\partial T_e}{\partial t} = \vec{E}\cdot\vec{j}_e + \nabla\cdot\left(\frac{5}{2}T_e\vec{j}_e + \underline{\underline{\kappa}}_e\cdot\nabla T_e\right) - \frac{3}{2}T_e\nabla\cdot\vec{j}_e$$
$$- \sum_s \dot{n}_s e\left(\epsilon_s + \frac{3}{2}T_e\right) + Q_e^T \tag{6.32}$$

where e is the elementary charge, n_e is the electron number density, T_e is the electron temperature, $\vec{E}$ is the electric field, $\vec{j}_e$ is the electron current density, $\underline{\underline{\kappa}}_e$ is the electron thermal conductivity tensor, $\dot{n}_s$ is the electron impact-ionization rate for species s, ϵ_s is the ionization potential of species s, and Q_e^T is the electron thermal heat-exchange term [29] defined in Eq. 6.33.

$$Q_e^T = -\sum_s n_e\frac{2m_e}{m_s}\nu_{es}\frac{3}{2}\left(\frac{kT_e}{e} - \frac{kT_s}{e}\right) \tag{6.33}$$

where ν_{es} is the collision frequency between electrons and species s.

To finalize the description of the standalone 2D electron model, we simplify the energy equation by neglecting the collision and ionization terms. However, both loss terms are reintroduced in the energy equation once the standalone electron model is integrated in the hybrid-PIC framework in Section 6.7. So for now, the working energy equation becomes:

$$\frac{3}{2}en_e\frac{\partial T_e}{\partial t} = \vec{E}\cdot\vec{j}_e + \nabla\cdot\left(\frac{5}{2}T_e\vec{j}_e + \underline{\underline{\kappa}}_e\cdot\nabla T_e\right) - \frac{3}{2}T_e\nabla\cdot\vec{j}_e \tag{6.34}$$

6.2.2.1   Derivation

Here we individually expand the terms from Eq. 6.34. First, the Joule heating term in Eq. 6.35, followed by the $\nabla\cdot\left(\frac{5}{2}T_e\vec{j}_e + \underline{\underline{\kappa}}_e\cdot\nabla T_e\right)$ term in Eq. 6.36.

$$\vec{E} \cdot \vec{j}_e = E_r \cdot j_{er} + E_z \cdot j_{ez} \tag{6.35}$$

$$\nabla \cdot \left(\frac{5}{2} T_e \vec{j}_e + \underline{\underline{\kappa}}_e \cdot \nabla T_e \right) = \frac{5}{2} \nabla \cdot \left(T_e \vec{j}_e \right) + \nabla \cdot \left(\underline{\underline{\kappa}}_e \cdot \nabla T_e \right)$$

$$= \frac{5}{2} \left(T_e \nabla \cdot \vec{j}_e + \vec{j}_e \cdot \nabla T_e \right) + \nabla \cdot \left(\underline{\underline{\kappa}}_e \cdot \nabla T_e \right) \tag{6.36}$$

Now we consider the terms from Eq. 6.36. We start with the divergence of $\vec{j}_e$ in Eq. 6.37, followed by the dot product of $\vec{j}_e$ and ∇T_e in Eq. 6.38, and finally, the conductivity term in Eq. 6.39.

$$\nabla \cdot \vec{j}_e = \frac{1}{r} \left(\frac{\partial (r j_{er})}{\partial r} \right) + \left(\frac{1}{r} \frac{\partial j_{e\theta}}{\partial \theta} \right) + \frac{\partial j_{ez}}{\partial z}$$

$$= \frac{1}{r} \left(r \frac{\partial (j_{er})}{\partial r} + j_{er} \frac{\partial r}{\partial r} \right) + \frac{\partial j_{ez}}{\partial z}$$

$$= \frac{\partial (j_{er})}{\partial r} + \frac{j_{er}}{r} + \frac{\partial j_{ez}}{\partial z} \tag{6.37}$$

$$\vec{j}_e \cdot \nabla T_e = j_{er} \cdot \left(\frac{\partial T_e}{\partial r} \right) + j_{ez} \cdot \left(\frac{\partial T_e}{\partial z} \right) \tag{6.38}$$

$$\nabla \cdot (\underline{\underline{\kappa}} \cdot \nabla T_e) = \nabla \cdot \left(\begin{bmatrix} \kappa_{zz} & \kappa_{zr} & 0 \\ \kappa_{rz} & \kappa_{rr} & 0 \\ 0 & 0 & 0 \end{bmatrix} \cdot \begin{bmatrix} \frac{\partial T_e}{\partial z} \\ \frac{\partial T_e}{\partial r} \\ 0 \end{bmatrix} \right)$$

$$= \nabla \cdot \begin{bmatrix} \kappa_{zz} \frac{\partial T_e}{\partial z} + \kappa_{zr} \frac{\partial T_e}{\partial r} \\ \kappa_{rz} \frac{\partial T_e}{\partial z} + \kappa_{rr} \frac{\partial T_e}{\partial r} \\ 0 \end{bmatrix}$$

$$= \frac{\partial}{\partial z} \left(\kappa_{zz} \frac{\partial T_e}{\partial z} + \kappa_{zr} \frac{\partial T_e}{\partial r} \right) + \frac{1}{r} \left\{ \frac{\partial}{\partial r} \left[r \left(\kappa_{rz} \frac{\partial T_e}{\partial z} + \kappa_{rr} \frac{\partial T_e}{\partial r} \right) \right] \right\}$$

$$= \frac{\partial}{\partial z} \left(\kappa_{zz} \frac{\partial T_e}{\partial z} + \kappa_{zr} \frac{\partial T_e}{\partial r} \right) + \frac{\partial}{\partial r} \left[\left(\kappa_{rz} \frac{\partial T_e}{\partial z} + \kappa_{rr} \frac{\partial T_e}{\partial r} \right) \right]$$

$$+ \frac{1}{r} \left[\left(\kappa_{rz} \frac{\partial T_e}{\partial z} + \kappa_{rr} \frac{\partial T_e}{\partial r} \right) \right] \tag{6.39}$$

6.2.2.2 Master Equation for Energy

Substituting Eqs. 6.35-6.39 into Eq. 6.34:

$$\frac{3}{2} e n_e \frac{\partial T_e}{\partial t} = E_r \cdot j_{er} + E_z \cdot j_{ez}$$

$$+ \frac{5}{2} T_e \cdot \left[\left(\frac{\partial j_{er}}{\partial r} \right) + \frac{j_{er}}{r} + \left(\frac{\partial j_{ez}}{\partial z} \right) \right]$$

$$+ j_{er} \cdot \left(\frac{\partial T_e}{\partial r} \right) + j_{ez} \cdot \left(\frac{\partial T_e}{\partial z} \right)$$

$$+ \frac{\partial}{\partial z} \left(\kappa_{zz} \frac{\partial T_e}{\partial z} + \kappa_{zr} \frac{\partial T_e}{\partial r} \right) + \frac{\partial}{\partial r} \left[\left(\kappa_{rz} \frac{\partial T_e}{\partial z} + \kappa_{rr} \frac{\partial T_e}{\partial r} \right) \right]$$

$$+ \frac{1}{r} \left[\left(\kappa_{rz} \frac{\partial T_e}{\partial z} + \kappa_{rr} \frac{\partial T_e}{\partial r} \right) \right]$$

$$- \frac{3}{2} T_e \cdot \left[\left(\frac{\partial j_{er}}{\partial r} \right) + \frac{j_{er}}{r} + \left(\frac{\partial j_{ez}}{\partial z} \right) \right] \tag{6.40}$$

Simplifying:

$$\frac{3}{2}en_e\frac{\partial T_e}{\partial t} = E_r \cdot j_{er} + E_z \cdot j_{ez}$$

$$+ T_e \cdot \left[\left(\frac{\partial j_{er}}{\partial r}\right) + \frac{j_{er}}{r} + \left(\frac{\partial j_{ez}}{\partial z}\right)\right]$$

$$+ j_{er} \cdot \left(\frac{\partial T_e}{\partial r}\right) + j_{ez} \cdot \left(\frac{\partial T_e}{\partial z}\right)$$

$$+ \frac{\partial}{\partial z}\left(\kappa_{zz}\frac{\partial T_e}{\partial z} + \kappa_{zr}\frac{\partial T_e}{\partial r}\right) + \frac{\partial}{\partial r}\left[\left(\kappa_{rz}\frac{\partial T_e}{\partial z} + \kappa_{rr}\frac{\partial T_e}{\partial r}\right)\right]$$

$$+ \frac{1}{r}\left[\left(\kappa_{rz}\frac{\partial T_e}{\partial z} + \kappa_{rr}\frac{\partial T_e}{\partial r}\right)\right] \tag{6.41}$$

6.3 Discretization

6.3.1 Conservative Finite Difference Stencil

To resolve both the normal (rr, zz) and tangential (rz, zr) terms, a 9 point stencil is required. As shown in Fig. 6.2(a), it uses information from eight neighbors (NW, NN, NE, WW, EE, SW, SS and SE) to compute a value at the center point (00).

Note the use of three grids, as shown in Fig. 6.2(b): one is cell centered, while the other two are staggered by half a cell spatially in the two directions. On the cell-centered grid blue points represent the cell centers and black points the nodes. The east-west (e-w) staggered grid is shown in green and the north-south (n-s) staggered grid is shown in red. The main unknowns, plasma potential and electron temperature, are computed at the cell center. However, gradients are computed on the cell interfaces to ensure conservation properties, which is why the n-s and e-w staggered grids are necessary. The following notation is used for the staggered meshes:

$$kz + \frac{1}{2} = kz + 1 \text{ on e-w staggered grid}$$

$$kr + \frac{1}{2} = kr + 1 \text{ on n-s staggered grid}$$

$$kz - \frac{1}{2} = kz \text{ on e-w staggered grid}$$

$$kr - \frac{1}{2} = kr \text{ on n-s staggered grid}$$

(a) Cell centered stencil.   (b) Cell centered, nodal and staggered grids.
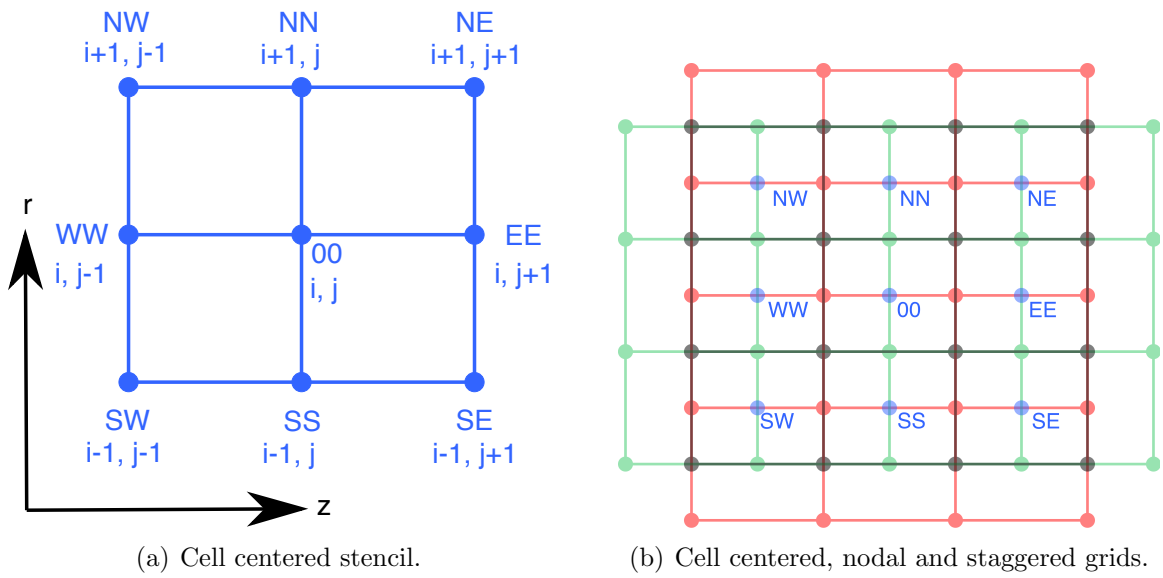
Figure 6.2: Numerical discretization.

6.3.2 Plasma Potential Discretization

$$LHS = \frac{(n_e\mu_{zz})^{kr,kz+\frac{1}{2}}\left(\phi^{kr,kz+1} - \phi^{kr,kz}\right) - (n_e\mu_{zz})^{kr,kz-\frac{1}{2}}\left(\phi^{kr,kz} - \phi^{kr,kz-1}\right)}{(\Delta z)^2}$$

$$+ \frac{(n_e\mu_{zr})^{kr,kz+\frac{1}{2}}\left(\phi^{kr+\frac{1}{2},kz+\frac{1}{2}} - \phi^{kr-\frac{1}{2},kz+\frac{1}{2}}\right) - (n_e\mu_{zr})^{kr,kz-\frac{1}{2}}\left(\phi^{kr+\frac{1}{2},kz-\frac{1}{2}} - \phi^{kr-\frac{1}{2},kz-\frac{1}{2}}\right)}{\Delta z \Delta r}$$

$$+ \frac{(n_e\mu_{rz})^{kr+\frac{1}{2},kz}\left(\phi^{kr+\frac{1}{2},kz+\frac{1}{2}} - \phi^{kr+\frac{1}{2},kz-\frac{1}{2}}\right) - (n_e\mu_{rz})^{kr-\frac{1}{2},kz}\left(\phi^{kr-\frac{1}{2},kz+\frac{1}{2}} - \phi^{kr-\frac{1}{2},kz-\frac{1}{2}}\right)}{\Delta r \Delta z}$$

$$+ \frac{(n_e\mu_{rr})^{kr+\frac{1}{2},kz}\left(\phi^{kr+1,kz} - \phi^{kr,kz}\right) - (n_e\mu_{rr})^{kr-\frac{1}{2},kz}\left(\phi^{kr,kz} - \phi^{kr-1,kz}\right)}{(\Delta r)^2}$$

$$+ \frac{(n_e\mu_{rz})^{kr,kz}\left(\frac{\phi^{kr,kz+\frac{1}{2}}-\phi^{kr,kz-\frac{1}{2}}}{\Delta z}\right) + (n_e\mu_{rr})^{kr,kz}\left(\frac{\phi^{kr+\frac{1}{2},kz}-\phi^{kr-\frac{1}{2},kz}}{\Delta r}\right)}{r} \qquad (6.42)$$

$$RHS = \frac{\mu_{zz}^{kr,kz+\frac{1}{2}}\left(p^{kr,kz+1} - p^{kr,kz}\right) - \mu_{zz}^{kr,kz-\frac{1}{2}}\left(p^{kr,kz} - p^{kr,kz-1}\right)}{(\Delta z)^2}$$

$$+ \frac{\mu_{zr}^{kr,kz+\frac{1}{2}}\left(p^{kr+\frac{1}{2},kz+\frac{1}{2}} - p^{kr-\frac{1}{2},kz+\frac{1}{2}}\right) - \mu_{zr}^{kr,kz-\frac{1}{2}}\left(p^{kr+\frac{1}{2},kz-\frac{1}{2}} - p^{kr-\frac{1}{2},kz-\frac{1}{2}}\right)}{\Delta z \Delta r}$$

$$+ \frac{\mu_{rz}^{kr+\frac{1}{2},kz}\left(p^{kr+\frac{1}{2},kz+\frac{1}{2}} - p^{kr+\frac{1}{2},kz-\frac{1}{2}}\right) - \mu_{rz}^{kr-\frac{1}{2},kz}\left(p^{kr-\frac{1}{2},kz+\frac{1}{2}} - p^{kr-\frac{1}{2},kz-\frac{1}{2}}\right)}{\Delta r \Delta z}$$

$$+ \frac{\mu_{rr}^{kr+\frac{1}{2},kz}\left(p^{kr+1,kz} - p^{kr,kz}\right) - \mu_{rr}^{kr-\frac{1}{2},kz}\left(p^{kr,kz} - p^{kr-1,kz}\right)}{(\Delta r)^2}$$

$$+ \frac{\mu_{rz}^{kr,kz}\left(\frac{p^{kr,kz+\frac{1}{2}}-p^{kr,kz-\frac{1}{2}}}{\Delta z}\right) + \mu_{rr}^{kr,kz}\left(\frac{p^{kr+\frac{1}{2},kz}-p^{kr-\frac{1}{2},kz}}{\Delta r}\right)}{r}$$

$$- \frac{1}{e}\left(\frac{j_{i,r}^{kr+1,kz} - j_{i,r}^{kr,kz}}{\Delta r} + \frac{j_{i,z}^{kr,kz+1} - j_{i,z}^{kr,kz}}{\Delta z} + \frac{j_{i,r}^{kr,kz}}{r}\right) \qquad (6.43)$$

Note that in the above discretization some values must be evaluated at the cell interfaces, which is equivalent to a $\frac{1}{2}$ index. These values are located on the staggered grids, but may be obtained by averaging their cell-centered neighbors:

$$\phi^{kr+\frac{1}{2},kz+\frac{1}{2}} = \frac{\phi^{kr+1,kz+1} + \phi^{kr+1,kz} + \phi^{kr,kz+1} + \phi^{kr,kz}}{4}$$

$$\phi^{kr-\frac{1}{2},kz+\frac{1}{2}} = \frac{\phi^{kr-1,kz+1} + \phi^{kr-1,kz} + \phi^{kr,kz+1} + \phi^{kr,kz}}{4}$$

$$\phi^{kr+\frac{1}{2},kz-\frac{1}{2}} = \frac{\phi^{kr+1,kz-1} + \phi^{kr+1,kz} + \phi^{kr,kz-1} + \phi^{kr,kz}}{4}$$

$$\phi^{kr-\frac{1}{2},kz-\frac{1}{2}} = \frac{\phi^{kr-1,kz-1} + \phi^{kr-1,kz} + \phi^{kr,kz-1} + \phi^{kr,kz}}{4}$$

$$\phi^{kr,kz+\frac{1}{2}} = \frac{\phi^{kr,kz+1} + \phi^{kr,kz}}{2}$$

$$\phi^{kr,kz-\frac{1}{2}} = \frac{\phi^{kr,kz-1} + \phi^{kr,kz}}{2}$$

$$\phi^{kr+\frac{1}{2},kz} = \frac{\phi^{kr+1,kz} + \phi^{kr,kz}}{2}$$

$$\phi^{kr-\frac{1}{2},kz} = \frac{\phi^{kr-1,kz} + \phi^{kr,kz}}{2} \tag{6.44}$$

which gives:

$$\phi^{kr+\frac{1}{2},kz+\frac{1}{2}} - \phi^{kr-\frac{1}{2},kz+\frac{1}{2}} = \frac{\phi^{kr+1,kz+1} + \phi^{kr+1,kz} - \phi^{kr-1,kz+1} - \phi^{kr-1,kz}}{4}$$

$$\phi^{kr+\frac{1}{2},kz-\frac{1}{2}} - \phi^{kr-\frac{1}{2},kz-\frac{1}{2}} = \frac{\phi^{kr+1,kz-1} + \phi^{kr+1,kz} - \phi^{kr-1,kz-1} - \phi^{kr-1,kz}}{4}$$

$$\phi^{kr+\frac{1}{2},kz+\frac{1}{2}} - \phi^{kr+\frac{1}{2},kz-\frac{1}{2}} = \frac{\phi^{kr+1,kz+1} + \phi^{kr,kz+1} - \phi^{kr+1,kz-1} - \phi^{kr,kz-1}}{4}$$

$$\phi^{kr-\frac{1}{2},kz+\frac{1}{2}} - \phi^{kr-\frac{1}{2},kz-\frac{1}{2}} = \frac{\phi^{kr-1,kz+1} + \phi^{kr,kz+1} - \phi^{kr-1,kz-1} - \phi^{kr,kz-1}}{4}$$

$$\phi^{kr,kz+\frac{1}{2}} - \phi^{kr,kz-\frac{1}{2}} = \frac{\phi^{kr,kz+1} - \phi^{kr,kz-1}}{2}$$

$$\phi^{kr+\frac{1}{2},kz} - \phi^{kr-\frac{1}{2},kz} = \frac{\phi^{kr+1,kz} - \phi^{kr-1,kz}}{2}$$

The discretized potential (Eq. 6.42) can thus be expressed only with cell centered values:

$$
\begin{aligned}
LHS = {}& \frac{(n_e\mu_{zz})^{kr,kz+1}\left(\phi^{kr,kz+1} - \phi^{kr,kz}\right) - (n_e\mu_{zz})^{kr,kz}\left(\phi^{kr,kz} - \phi^{kr,kz-1}\right)}{(\Delta z)^2} \\
& + \frac{(n_e\mu_{zr})^{kr,kz+1}\left(\phi^{kr+1,kz+1} + \phi^{kr+1,kz} - \phi^{kr-1,kz+1} - \phi^{kr-1,kz}\right)}{4\Delta z\Delta r} \\
& - \frac{(n_e\mu_{zr})^{kr,kz}\left(\phi^{kr+1,kz-1} + \phi^{kr+1,kz} - \phi^{kr-1,kz-1} - \phi^{kr-1,kz}\right)}{4\Delta z\Delta r} \\
& + \frac{(n_e\mu_{rz})^{kr+1,kz}\left(\phi^{kr+1,kz+1} + \phi^{kr,kz+1} - \phi^{kr+1,kz-1} - \phi^{kr,kz-1}\right)}{4\Delta r\Delta z} \\
& - \frac{(n_e\mu_{rz})^{kr,kz}\left(\phi^{kr-1,kz+1} + \phi^{kr,kz+1} - \phi^{kr-1,kz-1} - \phi^{kr,kz-1}\right)}{4\Delta r\Delta z} \\
& + \frac{(n_e\mu_{rr})^{kr+1,kz}\left(\phi^{kr+1,kz} - \phi^{kr,kz}\right) - (n_e\mu_{rr})^{kr,kz}\left(\phi^{kr,kz} - \phi^{kr-1,kz}\right)}{(\Delta r)^2} \\
& + \frac{\left((n_e\mu_{rz})^{kr+1,kz+1} + (n_e\mu_{rz})^{kr,kz+1}\right)}{2}\left(\frac{\phi^{kr,kz+1}}{2r\Delta z}\right) \\
& - \frac{\left((n_e\mu_{rz})^{kr+1,kz-1} + (n_e\mu_{rz})^{kr,kz-1}\right)}{2}\left(\frac{\phi^{kr,kz-1}}{2r\Delta z}\right) \\
& + \left(\frac{(n_e\mu_{rr})^{kr+1,kz}\phi^{kr+1,kz}}{2r\Delta r}\right) - \left(\frac{(n_e\mu_{rr})^{kr-1,kz}\phi^{kr-1,kz}}{2r\Delta r}\right)
\end{aligned} \tag{6.45}
$$

which can be written in compact form:

$$
\begin{aligned}
LHS = {}& \phi^{kr,kz+1}A_{EE} + \phi^{kr,kz}A_{00} + \phi^{kr,kz-1}A_{WW} + \phi^{kr+1,kz+1}A_{NE} \\
& + \phi^{kr+1,kz}A_{NN} + \phi^{kr-1,kz+1}A_{SE} + \phi^{kr-1,kz}A_{SS} \\
& + \phi^{kr+1,kz-1}A_{NW} + \phi^{kr-1,kz-1}A_{SW}
\end{aligned} \tag{6.46}
$$

where the A coefficients for plasma potential are defined as:

$$A_{00} = -\frac{(n_e\mu_{zz})^{kr,kz+1}}{(\Delta z)^2} - \frac{(n_e\mu_{zz})^{kr,kz}}{(\Delta z)^2} - \frac{(n_e\mu_{rr})^{kr+1,kz}}{(\Delta r)^2}$$
$$- \frac{(n_e\mu_{rr})^{kr+1,kz}}{(\Delta r)^2} \tag{6.47}$$

$$A_{EE} = \frac{(n_e\mu_{zz})^{kr,kz+1}}{(\Delta z)^2} + \frac{(n_e\mu_{rz})^{kr+1,kz}}{4\Delta r\Delta z} - \frac{(n_e\mu_{rz})^{kr,kz}}{4\Delta r\Delta z}$$
$$+ \frac{(n_e\mu_{rz})^{kr+1,kz+1} + (n_e\mu_{rz})^{kr,kz+1}}{2(2r\Delta z)} \tag{6.48}$$

$$A_{WW} = \frac{(n_e\mu_{zz})^{kr,kz}}{(\Delta z)^2} - \frac{(n_e\mu_{rz})^{kr+1,kz}}{4\Delta r\Delta z} + \frac{(n_e\mu_{rz})^{kr,kz}}{4\Delta r\Delta z}$$
$$- \frac{(n_e\mu_{rz})^{kr+1,kz-1} + (n_e\mu_{rz})^{kr,kz-1}}{2(2r\Delta z)} \tag{6.49}$$

$$A_{NN} = \frac{(n_e\mu_{zr})^{kr,kz+1}}{4\Delta z\Delta r} - \frac{(n_e\mu_{zr})^{kr,kz}}{4\Delta z\Delta r} + \frac{(n_e\mu_{rr})^{kr+1,kz}}{(\Delta r)^2}$$
$$+ \frac{(n_e\mu_{rr})^{kr+1,kz}}{2r\Delta r} \tag{6.50}$$

$$A_{SS} = -\frac{(n_e\mu_{zr})^{kr,kz+1}}{4\Delta z\Delta r} + \frac{(n_e\mu_{zr})^{kr,kz}}{4\Delta z\Delta r} + \frac{(n_e\mu_{rz})^{kr,kz}}{(\Delta r)^2}$$
$$- \frac{(n_e\mu_{rr})^{kr-1,kz}}{2r\Delta r} \tag{6.51}$$

$$A_{NE} = \frac{(n_e\mu_{zr})^{kr,kz+1}}{4\Delta z\Delta r} + \frac{(n_e\mu_{rz})^{kr+1,kz}}{4\Delta r\Delta z} \tag{6.52}$$

$$A_{SE} = -\frac{(n_e\mu_{zr})^{kr,kz+1}}{4\Delta z\Delta r} - \frac{(n_e\mu_{rz})^{kr,kz}}{4\Delta r\Delta z} \tag{6.53}$$

$$A_{NW} = -\frac{(n_e\mu_{zr})^{kr,kz}}{4\Delta z\Delta r} - \frac{(n_e\mu_{rz})^{kr+1,kz}}{4\Delta r\Delta z} \tag{6.54}$$

$$A_{SW} = \frac{(n_e\mu_{zr})^{kr,kz}}{4\Delta z\Delta r} + \frac{(n_e\mu_{rz})^{kr,kz}}{4\Delta r\Delta z} \tag{6.55}$$

6.3.3 Electron Temperature Discretization

We set up a first order accurate scheme in time, where the conductivity term is implicit. The superscript denotes the timestep, and Δt is the time increment.

$$\frac{3}{2}en_e^t\frac{T_e^{t+\Delta t}-T_e^t}{\Delta t}-\left[\frac{\partial}{\partial z}\left(\kappa_{zz}\frac{\partial T_e^{t+\Delta t}}{\partial z}+\kappa_{rz}\frac{\partial T_e^{t+\Delta t}}{\partial r}\right)\right.$$

$$+\frac{\partial}{\partial r}\left(\kappa_{rz}\frac{\partial T_e^{t+\Delta t}}{\partial z}+\kappa_{rr}\frac{\partial T_e^{t+\Delta t}}{\partial r}\right)$$

$$\left.+\frac{1}{r}\left(\kappa_{rz}\frac{\partial T_e^{t+\Delta t}}{\partial z}+\kappa_{rr}\frac{\partial T_e^{t+\Delta t}}{\partial r}\right)\right]$$

$$=E_r^t\cdot j_{er}^t+E_z^t\cdot j_{ez}^t$$

$$+T_e^t\cdot\left[\left(\frac{\partial j_{er}^t}{\partial r}\right)+\frac{j_{er}^t}{r}+\left(\frac{\partial j_{ez}^t}{\partial z}\right)\right]$$

$$+j_{er}^t\cdot\left(\frac{\partial T_e^t}{\partial r}\right)+j_{ez}^t\cdot\left(\frac{\partial T_e^t}{\partial z}\right) \tag{6.56}$$

and proceed to discretize Eq. 6.56 in space, where the subscript $-cc$ refers to cell center, $-ns$ is north-south staggered grid and $-ew$ is east-west staggered grid.

$$
\begin{aligned}
LHS = {} & \frac{3}{2} e n_e^t \frac{T_e^{t+\Delta t}}{\Delta t} \\
& - \left\{ \frac{\kappa_{zz-ew}^t[kr][kz+\frac{1}{2}]\left(T_{e-cc}^{t+\Delta t}[kr][kz+1] - T_{e-cc}^{t+\Delta t}[kr][kz]\right)}{(\Delta z)^2} \right. \\
& - \frac{\kappa_{zz-ew}^t[kr][kz-\frac{1}{2}]\left(T_{e-cc}^{t+\Delta t}[kr][kz] - T_{e-cc}^{t+\Delta t}[kr][kz-1]\right)}{(\Delta z)^2} \\
& + \frac{\kappa_{zr-ew}^t[kr][kz+\frac{1}{2}]\left(T_{e-cc}^{t+\Delta t}[kr+\frac{1}{2}][kz+\frac{1}{2}] - T_{e-cc}^{t+\Delta t}[kr-\frac{1}{2}][kz+\frac{1}{2}]\right)}{\Delta z \Delta r} \\
& - \frac{\kappa_{zr-ew}^t[kr][kz-\frac{1}{2}]\left(T_{e-cc}^{t+\Delta t}[kr+\frac{1}{2}][kz-\frac{1}{2}] - T_{e-cc}^{t+\Delta t}[kr-\frac{1}{2}][kz-\frac{1}{2}]\right)}{\Delta z \Delta r} \\
& + \frac{\kappa_{rz-ns}^t[kr+\frac{1}{2}][kz]\left(T_{e-cc}^{t+\Delta t}[kr+\frac{1}{2}][kz+\frac{1}{2}] - T_{e-cc}^{t+\Delta t}[kr+\frac{1}{2}][kz-\frac{1}{2}]\right)}{\Delta r \Delta z} \\
& - \frac{\kappa_{rz-ns}^t[kr-\frac{1}{2}][kz]\left(T_{e-cc}^{t+\Delta t}[kr-\frac{1}{2}][kz+\frac{1}{2}] - T_{e-cc}^{t+\Delta t}[kr-\frac{1}{2}][kz-\frac{1}{2}]\right)}{\Delta r \Delta z} \\
& + \frac{\kappa_{rr-ns}^t[kr+\frac{1}{2}][kz]\left(T_{e-cc}^{t+\Delta t}[kr+1][kz] - T_{e-cc}^{t+\Delta t}[kr][kz]\right)}{(\Delta r)^2} \\
& - \frac{\kappa_{rr-ns}^t[kr-\frac{1}{2}][kz]\left(T_{e-cc}^{t+\Delta t}[kr][kz] - T_{e-cc}^{t+\Delta t}[kr-1][kz]\right)}{(\Delta r)^2} \\
& + \frac{1}{r}\left[\frac{\kappa_{rz-cc}^t[kr][kz]\left(T_{e-cc}^{t+\Delta t}[kr][kz+\frac{1}{2}] - T_{e-cc}^{t+\Delta t}[kr][kz-\frac{1}{2}]\right)}{\Delta z} \right. \\
& \left.\left. + \frac{\kappa_{rr-cc}^t[kr][kz]\left(T_{e-cc}^{t+\Delta t}[kr+\frac{1}{2}][kz] - T_{e-cc}^{t+\Delta t}[kr-\frac{1}{2}][kz]\right)}{\Delta r} \right] \right\}
\end{aligned}
\tag{6.57}
$$

$$RHS = \left(\frac{E_{r-ns}^t[kr+1][kz] \cdot j_{er}^t[kr+1][kz] + E_{r-ns}^t[kr][kz] \cdot j_{er}^t[kr][kz]}{2} \right.$$

$$\left. + \frac{E_{z-ew}^t[kr][kz+1] \cdot j_{ez}^t[kr][kz+1] + E_{z-ew}^t[kr][kz] \cdot j_{ez}^t[kr][kz]}{2} \right)$$

$$+ T_{e-cc}^t[kr][kz] \cdot \left[\left(\frac{j_{er-ns}^t[kr+1][kz] - j_{er-ns}^t[kr][kz]}{\Delta r} \right) \right.$$

$$+ \left(\frac{j_{er-ns}^t[kr+1][kz] + j_{er-ns}^t[kr][kz]}{2r} \right)$$

$$\left. + \left(\frac{j_{ez-ew}^t[kr][kz+1] - j_{ez-ew}^t[kr][kz]}{\Delta z} \right) \right]$$

$$+ j_{er-cc}^t[kr][kz] \cdot \left(\frac{T_{e-ns}^t[kr+1][kz] - T_{e-ns}^t[kr][kz]}{\Delta r} \right)$$

$$+ j_{ez-cc}^t[kr][kz] \cdot \left(\frac{T_{e-ew}^t[kr][kz+1] - T_{e-ew}^t[kr][kz]}{\Delta z} \right)$$

$$+ \frac{3}{2} \cdot \frac{e}{4\Delta t} \left(n_{e-ns}^t[kr+1][kz]T_{e-ns}^t[kr+1][kz] \right.$$

$$+ n_{e-ns}^t[kr][kz]T_{e-ns}^t[kr][kz]$$

$$+ n_{e-ew}^t[kr][kz+1]T_{e-ew}^t[kr][kz+1]$$

$$+ n_{e-ew}^t[kr][kz]T_{e-ew}^t[kr][kz] \big) \tag{6.58}$$

We calculate the one half locations on the cell-centered grid as in the plasma potential discretization (Eq. 6.44) and re-write Eq. 6.57:

$$
\begin{aligned}
LHS = {} & \frac{3}{2} e n_e^t \frac{T_e^{t+\Delta t}}{\Delta t} \\
& - \Bigg\{ \frac{\kappa_{zz-ew}^t[kr][kz+\frac{1}{2}]}{(\Delta z)^2} \left(T_{e-cc}^{t+\Delta t}[kr][kz+1] - T_{e-cc}^{t+\Delta t}[kr][kz] \right) \\
& - \frac{\kappa_{zz-ew}^t[kr][kz-\frac{1}{2}]}{(\Delta z)^2} \left(T_{e-cc}^{t+\Delta t}[kr][kz] - T_{e-cc}^{t+\Delta t}[kr][kz-1] \right) \\
& + \frac{\kappa_{zr-ew}^t[kr][kz+\frac{1}{2}]}{4\Delta z \Delta r} \left(T_{e-cc}^{t+\Delta t}[kr+1][kz+1] + T_{e-cc}^{t+\Delta t}[kr+1][kz] \right. \\
& \left. - T_{e-cc}^{t+\Delta t}[kr-1][kz+1] - T_{e-cc}^{t+\Delta t}[kr-1][kz] \right) \\
& - \frac{\kappa_{zr-ew}^t[kr][kz-\frac{1}{2}]}{4\Delta z \Delta r} \left(T_{e-cc}^{t+\Delta t}[kr+1][kz-1] + T_{e-cc}^{t+\Delta t}[kr+1][kz] \right. \\
& \left. - T_{e-cc}^{t+\Delta t}[kr-1][kz-1] - T_{e-cc}^{t+\Delta t}[kr-1][kz] \right) \\
& + \frac{\kappa_{rz-ns}^t[kr+\frac{1}{2}][kz]}{4\Delta r \Delta z} \left(T_{e-cc}^{t+\Delta t}[kr+1][kz+1] + T_{e-cc}^{t+\Delta t}[kr][kz+1] \right. \\
& \left. - T_{e-cc}^{t+\Delta t}[kr+1][kz-1] - T_{e-cc}^{t+\Delta t}[kr][kz-1] \right) \\
& - \frac{\kappa_{rz-ns}^t[kr-\frac{1}{2}][kz]}{4\Delta r \Delta z} \left(T_{e-cc}^{t+\Delta t}[kr-1][kz+1] + T_{e-cc}^{t+\Delta t}[kr][kz+1] \right. \\
& \left. - T_{e-cc}^{t+\Delta t}[kr-1][kz-1] - T_{e-cc}^{t+\Delta t}[kr][kz-1] \right) \\
& + \frac{\kappa_{rr-ns}^t[kr+\frac{1}{2}][kz]}{(\Delta r)^2} \left(T_{e-cc}^{t+\Delta t}[kr+1][kz] - T_{e-cc}^{t+\Delta t}[kr][kz] \right) \\
& - \frac{\kappa_{rr-ns}^t[kr-\frac{1}{2}][kz]}{(\Delta r)^2} \left(T_{e-cc}^{t+\Delta t}[kr][kz] - T_{e-cc}^{t+\Delta t}[kr-1][kz] \right) \\
& + \frac{1}{2r} \left[\frac{\kappa_{rz-cc}^t[kr][kz]}{\Delta z} \left(T_{e-cc}^{t+\Delta t}[kr][kz+1] - T_{e-cc}^{t+\Delta t}[kr][kz-1] \right) \right. \\
& \left. \left. + \frac{\kappa_{rr-cc}^t[kr][kz]}{\Delta r} \left(T_{e-cc}^{t+\Delta t}[kr+1][kz] - T_{e-cc}^{t+\Delta t}[kr-1][kz] \right) \right] \right\}
\end{aligned}
\tag{6.59}
$$

We compute the cell-center cross-term values of thermal conductivity by averaging

on the n-s staggered grid:

$$
\begin{aligned}
LHS = {} & \frac{3}{2}en_e^t\frac{T_e^{t+\Delta t}}{\Delta t} \\
& - \left\{ \frac{\kappa_{zz-ew}^t[kr][kz+\frac{1}{2}]}{(\Delta z)^2}\left(T_{e-cc}^{t+\Delta t}[kr][kz+1] - T_{e-cc}^{t+\Delta t}[kr][kz]\right) \right. \\
& - \frac{\kappa_{zz-ew}^t[kr][kz-\frac{1}{2}]}{(\Delta z)^2}\left(T_{e-cc}^{t+\Delta t}[kr][kz] - T_{e-cc}^{t+\Delta t}[kr][kz-1]\right) \\
& + \frac{\kappa_{zr-ew}^t[kr][kz+\frac{1}{2}]}{4\Delta z\Delta r}\left(T_{e-cc}^{t+\Delta t}[kr+1][kz+1] + T_{e-cc}^{t+\Delta t}[kr+1][kz]\right. \\
& - \left.T_{e-cc}^{t+\Delta t}[kr-1][kz+1] - T_{e-cc}^{t+\Delta t}[kr-1][kz]\right) \\
& - \frac{\kappa_{zr-ew}^t[kr][kz-\frac{1}{2}]}{4\Delta z\Delta r}\left(T_{e-cc}^{t+\Delta t}[kr+1][kz-1] + T_{e-cc}^{t+\Delta t}[kr+1][kz]\right. \\
& - \left.T_{e-cc}^{t+\Delta t}[kr-1][kz-1] - T_{e-cc}^{t+\Delta t}[kr-1][kz]\right) \\
& + \frac{\kappa_{rz-ns}^t[kr+\frac{1}{2}][kz]}{4\Delta r\Delta z}\left(T_{e-cc}^{t+\Delta t}[kr+1][kz+1] + T_{e-cc}^{t+\Delta t}[kr][kz+1]\right. \\
& - \left.T_{e-cc}^{t+\Delta t}[kr+1][kz-1] - T_{e-cc}^{t+\Delta t}[kr][kz-1]\right) \\
& - \frac{\kappa_{rz-ns}^t[kr-\frac{1}{2}][kz]}{4\Delta r\Delta z}\left(T_{e-cc}^{t+\Delta t}[kr-1][kz+1] + T_{e-cc}^{t+\Delta t}[kr][kz+1]\right. \\
& - \left.T_{e-cc}^{t+\Delta t}[kr-1][kz-1] - T_{e-cc}^{t+\Delta t}[kr][kz-1]\right) \\
& + \frac{\kappa_{rr-ns}^t[kr+\frac{1}{2}][kz]}{(\Delta r)^2}\left(T_{e-cc}^{t+\Delta t}[kr+1][kz] - T_{e-cc}^{t+\Delta t}[kr][kz]\right) \\
& - \frac{\kappa_{rr-ns}^t[kr-\frac{1}{2}][kz]}{(\Delta r)^2}\left(T_{e-cc}^{t+\Delta t}[kr][kz] - T_{e-cc}^{t+\Delta t}[kr-1][kz]\right) \\
& + \left(\frac{\kappa_{rz-ns}^t[kr+\frac{1}{2}][kz+1] + \kappa_{rz-ns}^t[kr-\frac{1}{2}][kz+1]}{4r\Delta z}\right)T_{e-cc}^{t+\Delta t}[kr][kz+1] \\
& - \left(\frac{\kappa_{rz-ns}^t[kr+\frac{1}{2}][kz-1] + \kappa_{rz-ns}^t[kr-\frac{1}{2}][kz-1]}{4r\Delta z}\right)T_{e-cc}^{t+\Delta t}[kr][kz-1] \\
& + \frac{\kappa_{rr-ns}^t[kr+1][kz]}{2r\Delta r}T_{e-cc}^{t+\Delta t}[kr+1][kz] \\
& - \left. \frac{\kappa_{rr-ns}^t[kr-1][kz]}{2r\Delta r}T_{e-cc}^{t+\Delta t}[kr-1][kz]\right\}
\end{aligned}
\tag{6.60}
$$

We further rewrite Eq. 6.60 as:

$$LHS = \frac{3}{2}en_e^t\frac{T_e^{t+\Delta t}}{\Delta t}$$

$$+ Te^{t+\Delta t}[kr][kz+1]A_{EE} + Te^{t+\Delta t}[kr][kz]A_{00}$$

$$+ Te^{t+\Delta t}[kr][kz-1]A_{WW}$$

$$+ Te^{t+\Delta t}[kr+1][kz+1]A_{NE} + Te^{t+\Delta t}[kr+1][kz]A_{NN}$$

$$+ Te^{t+\Delta t}[kr+1][kz-1]A_{NW}$$

$$+ Te^{t+\Delta t}[kr-1][kz+1]A_{SE} + Te^{t+\Delta t}[kr-1][kz]A_{SS}$$

$$+ Te^{t+\Delta t}[kr-1][kz-1]A_{SW} \qquad (6.61)$$

where the A coefficients for temperature are defined as:

$$
\begin{aligned}
A_{EE} = -\Bigg(& \frac{\kappa^t_{zz-ew}[kr][kz+\frac{1}{2}]}{(\Delta z)^2} + \frac{\kappa^t_{rz-ew}[kr+\frac{1}{2}][kz]}{4\Delta r \Delta z} \\
& - \frac{\kappa^t_{rz-ew}[kr+\frac{1}{2}][kz]}{4\Delta r \Delta z} \\
& + \frac{\kappa^t_{rz-ns}[kr+\frac{1}{2}][kz+1] + \kappa^t_{rz-ns}[kr-\frac{1}{2}][kz+1]}{4r\Delta z} \Bigg)
\end{aligned}
\tag{6.62}
$$

$$
\begin{aligned}
A_{00} = -\Bigg(& -\frac{\kappa^t_{zz-ew}[kr][kz+\frac{1}{2}]}{(\Delta z)^2} - \frac{\kappa^t_{zz-ew}[kr][kz-\frac{1}{2}]}{(\Delta z)^2} \\
& - \frac{\kappa^t_{rr-ns}[kr+\frac{1}{2}][kz]}{(\Delta r)^2} - \frac{\kappa^t_{rr-ns}[kr-\frac{1}{2}][kz]}{(\Delta r)^2} \Bigg)
\end{aligned}
\tag{6.63}
$$

$$
\begin{aligned}
A_{WW} = -\Bigg(& \frac{\kappa^t_{zz-ew}[kr][kz-\frac{1}{2}]}{(\Delta z)^2} - \frac{\kappa^t_{rz-ns}[kr+\frac{1}{2}][kz]}{4\Delta r \Delta z} \\
& + \frac{\kappa^t_{rz-ns}[kr-\frac{1}{2}][kz]}{4\Delta r \Delta z} \\
& - \frac{\kappa^t_{rz-ns}[kr+\frac{1}{2}][kz-1] + \kappa^t_{rz-ns}[kr-\frac{1}{2}][kz-1]}{4r\Delta z} \Bigg)
\end{aligned}
\tag{6.64}
$$

$$
A_{NE} = -\left(\frac{\kappa^t_{zr-ew}[kr][kz+\frac{1}{2}]}{4\Delta z \Delta r} + \frac{\kappa^t_{rz-ns}[kr+\frac{1}{2}][kz]}{4\Delta r \Delta z} \right)
\tag{6.65}
$$

$$
\begin{aligned}
A_{NN} = -\Bigg(& \frac{\kappa^t_{zr-ew}[kr][kz+\frac{1}{2}]}{4\Delta z \Delta r} - \frac{\kappa^t_{zr-ew}[kr][kz-\frac{1}{2}]}{4\Delta z \Delta r} \\
& + \frac{\kappa_{rr-ns}[kr+\frac{1}{2}][kz]}{(\Delta r)^2} + \frac{\kappa^t_{rr-ns}[kr+\frac{1}{2}][kz]}{2r\Delta r} \Bigg)
\end{aligned}
\tag{6.66}
$$

$$
A_{NW} = -\left(-\frac{\kappa^t_{zr-ew}[kr][kz-\frac{1}{2}]}{4\Delta z \Delta r} - \frac{\kappa^t_{rz-ns}[kr+\frac{1}{2}][kz]}{4\Delta r \Delta z} \right)
\tag{6.67}
$$

$$
A_{SE} = -\left(-\frac{\kappa^t_{zr-ew}[kr][kz+\frac{1}{2}]}{4\Delta z \Delta r} - \frac{\kappa^t_{rz-ns}[kr-\frac{1}{2}][kz]}{4\Delta r \Delta z} \right)
\tag{6.68}
$$

$$
\begin{aligned}
A_{SS} = -\Bigg(& -\frac{\kappa^t_{zr-ew}[kr][kz+\frac{1}{2}]}{4\Delta z \Delta r} + \frac{\kappa^t_{zr-ew}[kr][kz-\frac{1}{2}]}{4\Delta z \Delta r} \\
& + \frac{\kappa^t_{rr-ns}[kr-\frac{1}{2}][kz]}{(\Delta r)^2} - \frac{\kappa^t_{rr-cc}[kr-\frac{1}{2}][kz]}{2r\Delta r} \Bigg)
\end{aligned}
\tag{6.69}
$$

$$
A_{SW} = -\left(\frac{\kappa^t_{zr-ew}[kr][kz-\frac{1}{2}]}{4\Delta z \Delta r} + \frac{\kappa^t_{rz-ns}[kr-\frac{1}{2}][kz]}{4\Delta r \Delta z} \right)
\tag{6.70}
$$

6.3.4 Thermal Conductivity

We implement the expression derived by Braginskii [75], and also referenced by Goebel and Katz [29], which defines the thermal conductivity in the directions parallel and perpendicular to the magnetic field lines:

$$\kappa_\parallel = 3.16 \frac{ne^2 T_e}{m} \tau_e \tag{6.71}$$

$$\kappa_\perp = 4.66 \frac{ne^2 T_e}{m \omega_e^2 \tau_e} \tag{6.72}$$

where the total collision time, τ_e, and electron cyclotron frequency, ω_e, are defined as:

$$\tau_e = \frac{1}{\nu_{ei} + \nu_{en}} \tag{6.73}$$

$$\omega_e = \frac{qB}{m} \tag{6.74}$$

We are working in a coordinate system independent of the magnetic field lines, so a coordinate transformation is necessary to compute the thermal conductivity tensor in the axial-radial (r-z) coordinate system.

$$\begin{bmatrix} \kappa_{zz} & \kappa_{zr} \\ \kappa_{rz} & \kappa_{rr} \end{bmatrix} = \Theta \begin{bmatrix} \kappa_\perp & 0 \\ 0 & \kappa_\parallel \end{bmatrix} \Theta^{-1} \tag{6.75}$$

The transformation matrix, Θ, and its inverse are defined as:

$$\Theta = \begin{bmatrix} \cos\theta & -\sin\theta \\ \sin\theta & \cos\theta \end{bmatrix} \tag{6.76}$$

$$\Theta^{-1} = \begin{bmatrix} \cos\theta & \sin\theta \\ -\sin\theta & \cos\theta \end{bmatrix} \tag{6.77}$$

$$\sin\theta = \frac{B_z}{B} \tag{6.78}$$

$$\cos\theta = \frac{B_r}{B} \tag{6.79}$$

Therefore:

$$\begin{aligned} \kappa_{zz} &= \cos^2(\theta)\,\kappa_\perp + \sin^2(\theta)\,\kappa_\| \\ &= \left(\frac{B_r}{B}\right)^2 \kappa_\perp + \left(\frac{B_z}{B}\right)^2 \kappa_\| \end{aligned} \tag{6.80}$$

$$\begin{aligned} \kappa_{zr} &= -\sin(\theta)\cos(\theta)\,\kappa_\perp + \sin(\theta)\cos(\theta)\,\kappa_\| \\ &= -\frac{B_z B_r}{B^2}\kappa_\perp + \frac{B_z B_r}{B^2}\kappa_\| \end{aligned} \tag{6.81}$$

$$\begin{aligned} \kappa_{rr} &= \sin^2(\theta)\,\kappa_\perp + \cos^2(\theta)\,\kappa_\| \\ &= \left(\frac{B_z}{B}\right)^2 \kappa_\perp + \left(\frac{B_r}{B}\right)^2 \kappa_\| \end{aligned} \tag{6.82}$$

$$\begin{aligned} \kappa_{rz} &= -\sin(\theta)\cos(\theta)\,\kappa_\perp + \sin(\theta)\cos(\theta)\,\kappa_\| \\ &= -\frac{B_z B_r}{B^2}\kappa_\perp + \frac{B_z B_r}{B^2}\kappa_\| \end{aligned} \tag{6.83}$$

6.4 Boundary Conditions

6.4.1 Pressure

Pressure is determined by electron temperature and number density. Both quantities are known throughout the entire domain either because they are computed previously,

or because an initial guess is made during the first iteration. Therefore, we simply set the pressure values on the boundary in a consistent way through Dirichlet boundary conditions.

6.4.2 Plasma Potential

Figure 6.3 shows the north wall and two adjacent cells. The potential values at the cell centers are ϕ_{00} and ϕ_{EE}. We will show the expression for the electric field at at the wall, at node location NE.
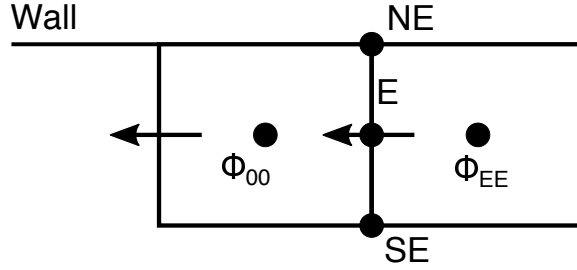
Figure 6.3: Description of the north boundary condition in the tangential direction.

$$\Gamma_{ez}^E = \left(n_e \mu_{zz} E_z + \frac{\mu_{zz}}{e} \frac{\partial p}{\partial z} \right)^E + \boxed{\left(n_e \mu_{zr} E_r + \mu_{zr} \frac{\partial p}{\partial r} \right)^E} \tag{6.84}$$

We express the boxed term in Eq. 6.84 as an average between north and south values:

$$\left(n_e \mu_{zr} E_r + \frac{\mu_{zr}}{e} \frac{\partial p}{\partial r} \right)^E = \frac{1}{2} \boxed{\left(n_e \mu_{zr} E_r + \mu_{zr} \frac{\partial p}{\partial r} \right)^{NE}} $$
$$+ \frac{1}{2} \left(n_e \mu_{zr} E_r + \mu_{zr} \frac{\partial p}{\partial r} \right)^{SE} \tag{6.85}$$

We now consider the boxed term in Eq. 6.85 for two types of north boundary material:

1. metal (anode and cathode)

2. dielectric (thruster channel walls)

For metal:

$$E_r^{NE} = \frac{\phi_{wall} - \frac{1}{2}\left(\phi_0 + \phi_{ee}\right)}{(\Delta r/2)} \tag{6.86}$$

In addition, the potential at the wall, ϕ_{wall} must be specified as the anode or cathode value.

For dielectric:

$$\mu_{zr} = -coef_{zr}\mu$$

$$\mu_{rr} = -coef_{rr}\mu$$

$$coef_{rr}\left(n_e\mu_{zr}E_r + \mu_{zr}\frac{\partial p}{\partial r}\right) = coef_{zr}\left(n_e\mu_{rr}E_r + \mu_{rr}\frac{\partial p}{\partial r}\right)$$

$$\left(n_e\mu_{zr}E_r + \mu_{zr}\frac{\partial p}{\partial r}\right) = \frac{coef_{zr}}{coef_{rr}}\left(n_e\mu_{rr}E_r + \mu_{rr}\frac{\partial p}{\partial r}\right) \tag{6.87}$$

Consider Eq. 6.24 for the radial electron flux, and we obtain:

$$\left(n_e\mu_{zr}E_r + \mu_{zr}\frac{\partial p}{\partial r}\right) = \frac{coef_{zr}}{coef_{rr}}\left[\Gamma_{er} - \left(n_e\mu_{rz}E_z + \mu_{rz}\frac{\partial p}{\partial z}\right)\right] \tag{6.88}$$

At the dielectric wall boundary, the sheath edge requires $\Gamma_{ir} = \Gamma_{er}$. Further rearranging Eq. 6.88 yields:

$$E_r^{NE} = \frac{1}{n_e\mu_{zr}} \cdot \frac{coef_{zr}}{coef_{rr}}\left[\Gamma_{ir} - \left(n_e\mu_{rz}E_z + \mu_{rz}\frac{\partial p}{\partial z}\right)\right] - \frac{1}{n_e} \cdot \frac{\partial p}{\partial r} \tag{6.89}$$

6.4.3 Electron Temperature

For the anode and cathode, we use Dirichlet boundary conditions. However, for the dielectric walls, we use a Neumann boundary condition in the direction perpendicular to the wall, and no special handling in the tangential direction. For the north

wall, where T_e^{NN} is in the ghost cell:

$$\frac{\partial T_e}{\partial r} = Q \tag{6.90}$$

$$\frac{T_e^{NN} - T_e^{00}}{\Delta r} = Q$$

$$T_e^{NN} = \Delta r Q + T_e^{00} \tag{6.91}$$

We assume $Q = 0$, which is equivalent to an insulating wall. We are not including wall losses, however these may be introduced by adding an electron-wall collision frequency.

6.5   Standalone 2D-axisymmetric Fluid Electron Model

A flowchart of the standalone 2D electron model is presented in Fig. 6.4. The first box shows the inputs: the thruster magnetic field, the electron mobility, the electron density and the ion current. The magnetic field is constant in time. Due to the quasi-neutrality assumption, the electron number density is derived from a previous heavy-species calculation. Next an initial guess must be made for the electron temperature. For the standalone 2D electron model, these input values are time-averaged results from an HPHall simulation that used the quasi-1D electron model. The potential solver algorithm is then applied to compute the plasma potential, electric field and electron current density. Next, these values are used in the energy solver. If the number of maximum electron timesteps (N_e) is reached, then the plasma potential, electric field, electron current density and electron temperature are output. Otherwise, the process is repeated with the newly computed value of electron temperature.
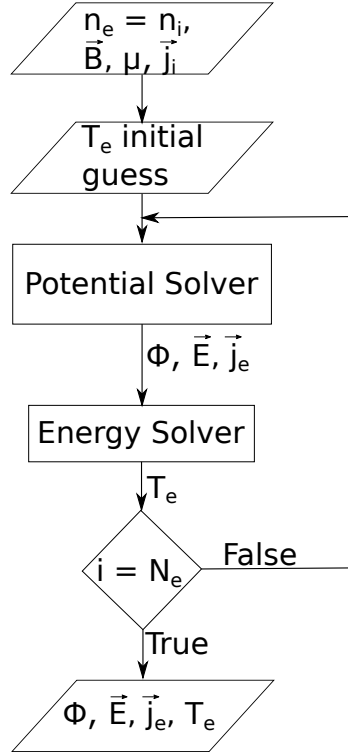
Figure 6.4: Standalone 2D electron model flowchart.

6.6 Verification

We are interested in developing a time-dependent simulation platform for Hall thrusters which are known to show unsteady behavior. Since the plasma potential equation is elliptic, the only time dependence that we observe comes from the energy equation. We first verify current conservation, in Section 6.6.1, by running only the potential solver, without the energy solver, hence the results from that section are not time dependent. However, in Section 6.6.2 we focus on verifying the accuracy and stability properties of the energy equation. We thus introduce a simplified analytic solution in Section 6.6.2.1 that is only relevant to the temperature equation, so the plasma potential solver is disabled for all work presented in Sections 6.6.2.2 and 6.6.2.3. However, we return to the full standalone model which includes the potential solver, when we verify convergence in Section 6.6.3.

6.6.1 Current Conservation

The first step for model verification is the computation of the electron current at the anode and cathode. In this section, only the plasma potential solver is used, the electron temperature module is turned off. A series of test cases are prepared: the first six cases only focus on the thruster channel, and they are developed to reduce differences between the 2D electron model and the HPHall simulation that may be due to mesh or boundary condition handling, in particular the implementation of the cathode line from HPHall [21]. The seventh test case includes the thruster plume. The first three test cases have a zero axial component of the magnetic field, while the final four have a curved magnetic field with both axial and radial nonzero magnetic field components. For the thruster channel cases (1-6) three magnetic field magnitudes are tested: a nominal case (low), an intermediate case, and a high value case (approximately double the value of the low field case, when comparing magnitudes at the location of maximum field strength). The magnetic field topologies are shown in Figure 6.5. Notice that for the plume case the curvature of the magnetic field is reversed in the plume.

The plasma potential boundary conditions for the channel and plume test cases are shown in Figures 6.6(a) and 6.6(b), respectively. The anode boundary is a Dirichlet condition where the potential is set to 300 V, while for the cathode, the value is set to 0 V. The walls, thruster pole pieces, as well as north and south plume boundaries use a dielectric boundary condition for plasma potential. Through this boundary condition we ensure that the electron current equals the ion current at the wall, in the normal direction.

For electron temperature, the anode and cathode use Dirichlet conditions, with values of 2 eV and 20 eV, respectively, which are chosen based on time-averaged HPHall
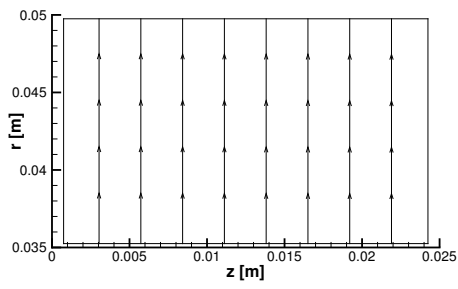
(a) Cases 1, 2, and 3.
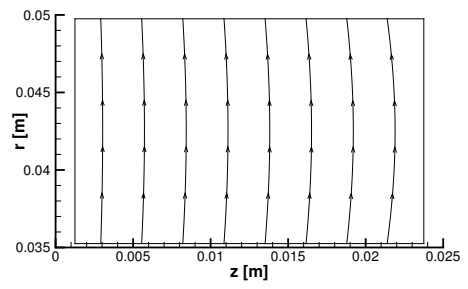
(b) Cases 4, 5, and 6.
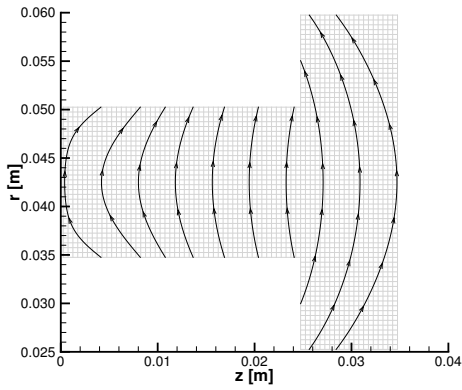
(c) Case 7.

Figure 6.5: Magnetic field topologies.

results for electron temperature. For the walls, a Neumann type condition is implemented, and the temperature flux is set to zero in the normal direction. No special considerations are included for the tangential direction.
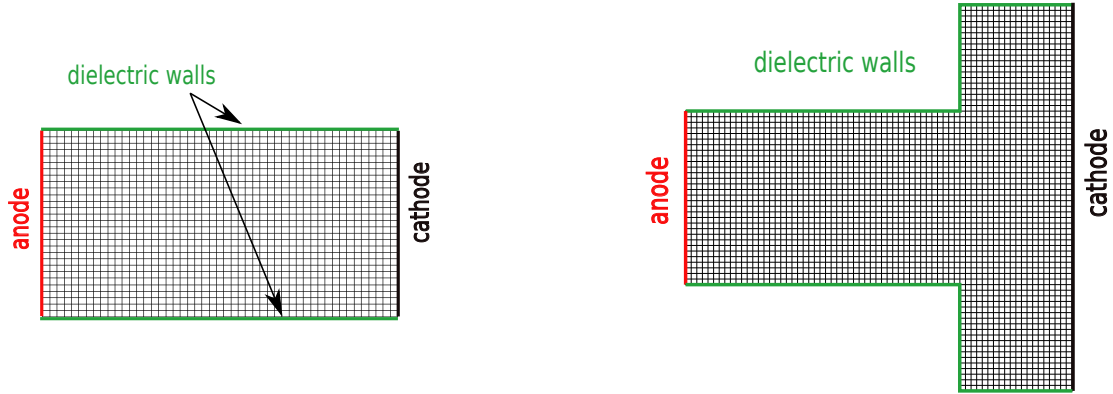
(a) Cases 1-6.

(b) Case 7.

Figure 6.6: Domain and boundary condition types for potential.

The electron current values are calculated by integrating the electron current density radially at the anode and cathode locations. In Table 6.1 we observe that in all five test cases the electron current is conserved through the domain. While for simulation results we typically report data with three significant digits, in the present case the anode and cathode currents were identical up to the fourth decimal place, suggesting that maximum losses due to the finite discretization are only 0.00049%.

Table 6.1: Discharge Current

Case	B_z	B_{max} (G)	I_{anode} (A), 2D	$I_{cathode}$ (A), 2D
1	0	317	4.16	4.16
2	0	422	3.40	3.40
3	0	633	2.49	2.49
4	$\neq 0$	316	4.56	4.56
5	$\neq 0$	422	3.59	3.59
6	$\neq 0$	633	2.36	2.36
7	$\neq 0$	790	5.03	5.03

6.6.2 Analytic Solution for Heat Equation

Verifying the full implementation of the energy equation solver for an HET is challenging due to its inherent complexity. However, a simplification that retains the main characteristics of the electron temperature equation may be verified with an analytic solution. This "toy problem" is defined in Section 6.6.2.1. In order to compare values over the entire 2D domain, the L_1 and L_2 norms will be employed later in this work. They are each defined in Appendix B. The plasma potential solver is turned off in this section.

6.6.2.1 Reduced Order Problem

Consider the 2D heat equation, as applied to a heated plate with length L (in x) and height H (in y). Further assume that the thermal conductivity is anisotropic in the two directions x and y, thus the values of κ_x and κ_y are different. Note that in this Section we are using the variable u instead of T_e for temperature to highlight that this is an analytic solution to a simplified problem, and not actual electron temperature. Further note that the thermal conductivity used in this section has different units than that used in the full energy equation: here we use eV m^2/s, while in Eq. 6.41 the units for conductivity are $\frac{eV \cdot s}{m^3 \cdot kg}$.

The physical setup is as follows: at time t = 0 s, the plate is at the uniform tempera-
ture u_0 and it is allowed to cool down in time [33]. Three of its edges (east, west and
south) are held at a constant temperature of 0 (Dirichlet boundary: u = 0 eV). The
remaining fourth edge (north) is insulated (Neumann boundary with $\frac{\partial u}{\partial y} = 0$). The
governing equation is:

$$u_t = \kappa_x \cdot u_{xx} + \kappa_y \cdot u_{yy} \; , \; 0 \leq x \leq L, \; , \; 0 \leq y \leq H \tag{6.92}$$

The boundary conditions are:

$$u(0, y, t) = 0 \text{ eV} = u(L, y, t) = u(x, 0, t) \; ; \; \frac{\partial u}{\partial y}(x, H, t) = 0 \tag{6.93}$$

The initial condition is:

$$u(x, y, 0) = 100 \text{ eV} \tag{6.94}$$

Solution details are given in Appendix C. The analytic solution with the given bound-
ary and initial conditions is found to be:

$$u(x, y, t) = \sum_{m=1}^{\infty} \sum_{n=1}^{\infty} A_{m2n-1} \cdot \sin\left(\frac{(2n-1)\pi x}{L}\right) \cos\left(\frac{(2m-1)\pi y}{2H}\right) \cdot e^{-\lambda_{m2n-1}t}$$

$$A_{m2n-1} = -\frac{1600}{(2n-1)(2m-1)(\pi^2)}$$

$$\lambda_{m2n-1} = \kappa_x \left(\frac{(2n-1)\pi}{L}\right) + \kappa_y \left(\frac{(2m-1)\pi}{2H}\right) \tag{6.95}$$

Results at time t = 1 ns are shown in Fig. 6.7 for four combinations of thermal conductivities:

- $\kappa_x = \kappa_y = 100$ eV m^2/s

- $\kappa_x = 100$ & $\kappa_y = 10{,}000$ eV m^2/s

- $\kappa_x = 10{,}000$ & $\kappa_y = 100$ eV m^2/s

- $\kappa_x = \kappa_y = 10{,}000$ eV m^2/s

As expected, we see that the diffusion process acts faster in the direction for which the conductivity is larger, and for those cases, the temperature decreases preferentially in the direction of higher conductivity.
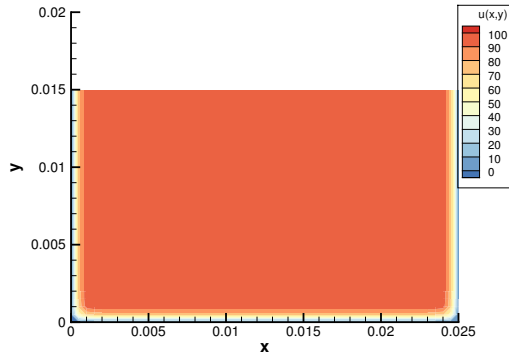
(a) $\kappa_x = 100$ and $\kappa_y = 100$.
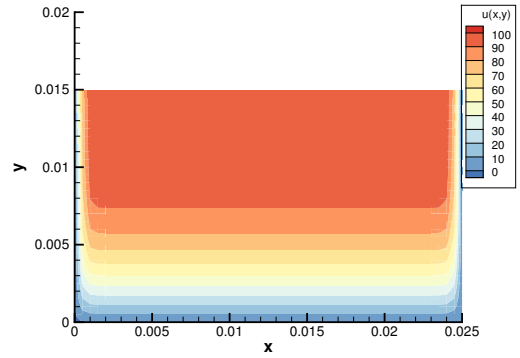
(b) $\kappa_x = 100$ and $\kappa_y = 10{,}000$.
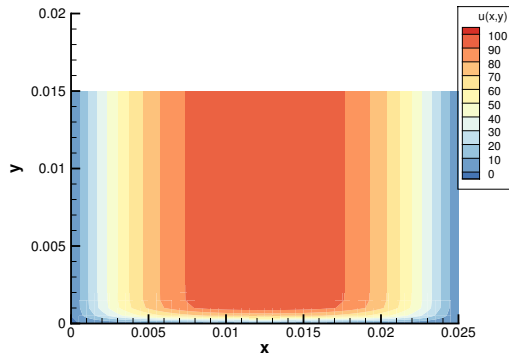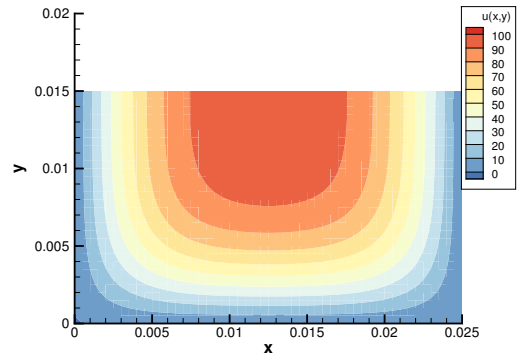
(c) $\kappa_x = 10{,}000$ and $\kappa_y = 100$.

(d) $\kappa_x = 10{,}000$ and $\kappa_y = 10{,}000$.

Figure 6.7: Analytic (series) solution to the heat equation with different, but constant thermal conductivities in the x and y directions. The units for conductivity in this case are eV m^2/s.

6.6.2.2 Isotropic thermal conductivity

In order to verify the implementation of the 2D electron energy solver, we keep only the time derivative and the conductivity terms from Eq. 6.32, while removing all additional terms. Thus we are left with the 2D heat equation.

While for the complete equation the implementation is semi-implicit in time, the scheme now becomes fully implicit for the 2D heat equation:

$$\frac{T_e^{t+\Delta t} - T_e^t}{\Delta t} - \left(\kappa \nabla^2 T_e^{t+\Delta t}\right) = 0 \tag{6.96}$$

where 10^2 eV$m^2/s \leq \kappa \equiv \frac{\kappa_e}{\frac{3}{2}en_e} \leq 10^4$ eVm^2/s. The bounds are determined from previous calculations by using the Braginskii equation [75] formulas for thermal conductivity.

Additional changes to the 2D model setup include the boundary conditions that are set to 0 at the anode, cathode and south wall, and a Neumann condition at the north wall. The initial temperature field is set to a value of 100 over the entire domain.

To investigate accuracy we run the energy solver for 0.5 μs of physical time with different timestep values, as shown in Fig. 6.8: Δt = 10 ns, 1 ns, 0.1 ns and 0.01 ns. While the scheme is stable and we can compute a solution within a single timestep, the accuracy degrades as Δt is increased. The more we refine the timestep, the better agreement we observe with the analytic solution.

The RMS (L_2 norm) and the mean (L_1 norm) difference between computational and analytic solutions over the entire domain are presented in Table 6.2. While other schemes may provide higher time accuracy, the present implementation is uncondi-

tionally stable, and immune to oscillations at large values of the timestep. Since HETs have unsteady physics, the robustness of the energy solver is important and thus the present numerical scheme will be used.

(a) x = 0.0125.

(b) y = 0.0075.
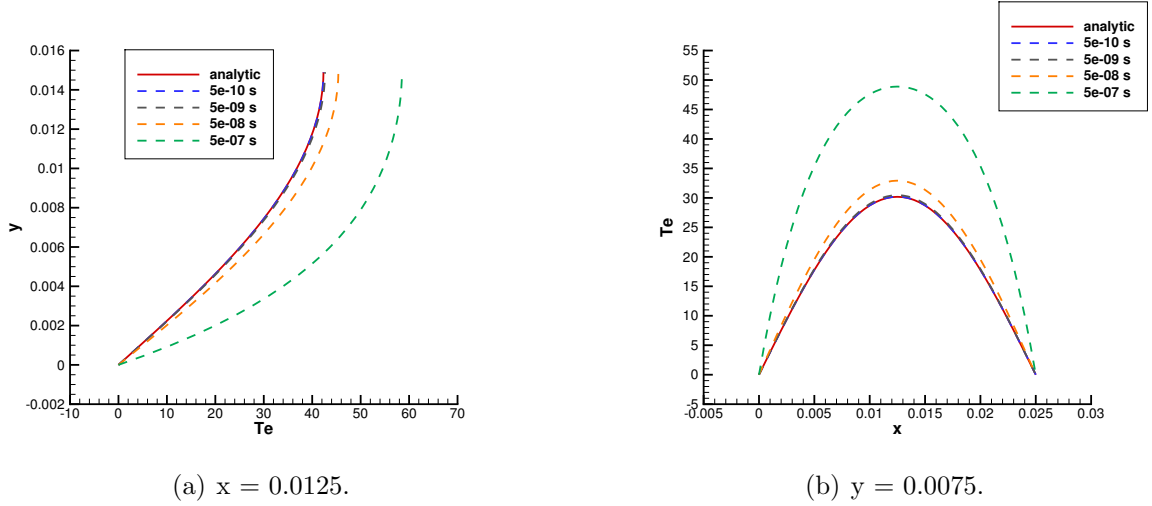
Figure 6.8: Electron temperature at time t = 0.5 μs from the vertical and horizontal centerlines with $\kappa_x = \kappa_y = 100$ eV m^2/s. The analytic solution is compared with simulation results obtained by using various timesteps. While the Δt = 50 ns simulation gives the closest result to the analytic solution, it requires 1000 steps. Increasing the timestep reduces the number of steps required at the cost of losing accuracy.

Table 6.2: L_1 and L_2 norms of the difference between the analytic and numerical temperature solutions.

timestep (s)	L_2 norm (% error)	L_1 norm (% error)
5×10^{-07}	133	109
5×10^{-08}	15.8	10.8
5×10^{-09}	12.6	2.62
5×10^{-10}	12.6	1.80

6.6.2.3 Anisotropic thermal conductivity

The L_1 and L_2 norms of the percent error between analytic and computed temperature values at time t = 0.5 μs are shown in Fig. 6.9. Four combinations of thermal conductivities are considered:

152

- $\kappa_x = \kappa_y = 100$ eV m^2/s

- $\kappa_x = 100$ & $\kappa_y = 10{,}000$ eV m^2/s

- $\kappa_x = 10{,}000$ & $\kappa_y = 100$ eV m^2/s

- $\kappa_x = \kappa_y = 10{,}000$ eV m^2/s

Different timestep values are used: 0.5 ps, 5 ps, 50 ps, 0.5 ns, 5 ns, 50 ns, and 0.5 μs. To verify convergence rate, a reference blue line is also included in the plots to show the slope of linear (O(1)) dependence. In all cases, the error diminishes at the O(1) rate, or faster. Note that in Fig. 6.9(a) we observe a slope that is less than one for timesteps smaller than 50 ps.

When using the original 51 x 31 mesh, the error appears to increase with decreasing timestep values, which may seem counterintuitive. However, the increase is due to other sources of error since we have effectively eliminated time errors. One such source is the spatial discretization, and refining the mesh by a factor of 2 in each direction, indeed yields a lower error in the region of interest ($\Delta t \leq 10^{-11}$), without changing the error plot for larger timesteps. The results for the refined mesh (101 x 61) are shown with a dashed line, while all the results with a continuous line are generated using the original 51 x 31 mesh.

The results in Fig. 6.9(a) also suggest that for low conductivities and a short time (0.5 μs), the lowest percent error that we can reach is O(10^{-3}), compared to the negligible values seen in the higher conductivity cases.
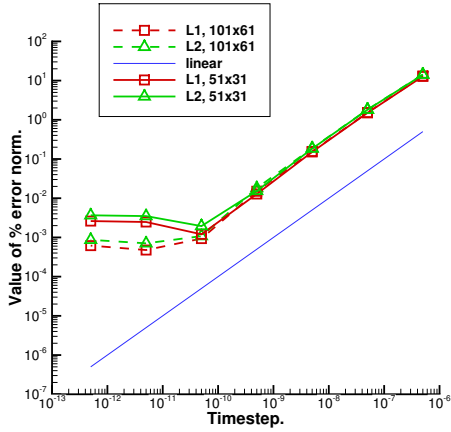
(a) $\kappa_x = 100$ and $\kappa_y = 100$.
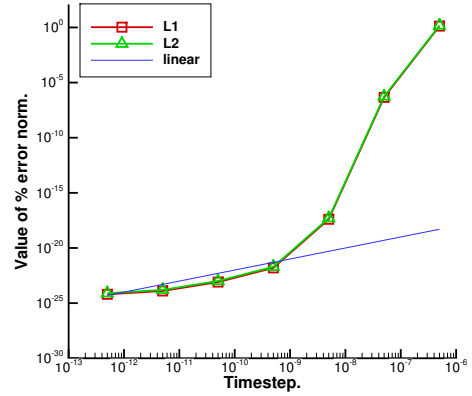
(b) $\kappa_x = 100$ and $\kappa_y = 10{,}000$.
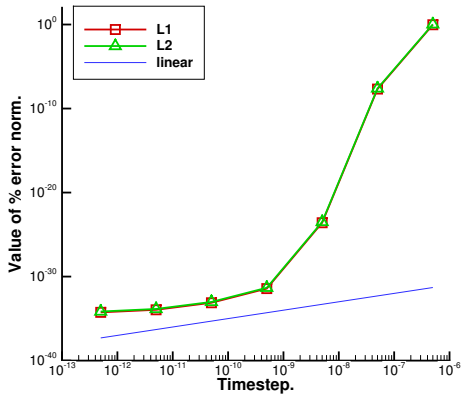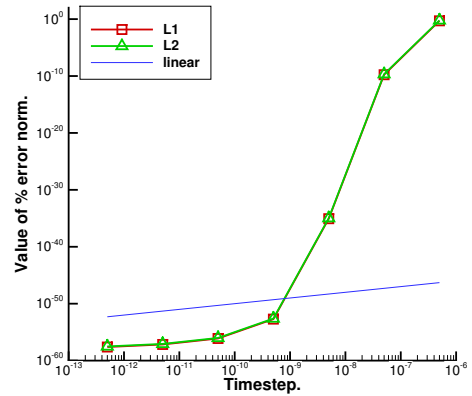
(c) $\kappa_x = 10{,}000$ and $\kappa_y = 100$.

(d) $\kappa_x = 10{,}000$ and $\kappa_y = 10{,}000$.

Figure 6.9: L_1 and L_2 norms of the percent error between analytic and computed temperature values at time t = 0.5 μs for different timestep values. The O(1) (linear) convergence line is also included for reference. The results shown with the solid lines use the original 51 x 31 computational mesh, while the dashed line results are obtained from a 101 x 61 refined mesh. The units for conductivity in this case are eV m^2/s

6.6.3 Standalone Electron Model Convergence

To simulate a Hall thruster-like problem, we set up a channel test case, that includes the anode, cathode and dielectric channel walls at the west, east and north-south boundaries respectively. For simplicity, a purely radial magnetic field is used. Here the energy equation from Eq. 6.32 is solved, and not just the heat equation, as in the verification cases from Section 6.6.2. The numerical scheme is now semi-implicit in time. Moreover, the plasma potential solver is also included.

The hybrid-PIC simulation HPHall is run with the quasi-1D electron model at a heavy species timestep of 5 ns and electron timestep of 3.33 ps (1500 times smaller) for 200,000 cycles. Then the time-averaged electron temperature and number density, axial and radial ion current densities, and electron mobility computed by HPHall are exported and loaded into the 2D electron model as inputs. From this starting point we are marching in time at an electron timestep value of 5 ns (same value as the heavy species timestep from the hybrid simulation).

We compute the residual of the electron temperature as the absolute value of the difference between the temperature at the previous time step and the newly computed temperature value:

$$T_e^{residual} = \frac{|T_e^{old} - T_e^{new}|}{T_e^{old}} \tag{6.97}$$

Next, we compute the L_1 and L_2 norms of the electron temperature residual over the entire domain at each timestep. Figure 6.10 shows a steep decrease of the norm of the residual (both L_1 and L_2) until the 2600th iteration. At this point both norms stabilize at a value below 10^{-10}. Since the electron temperature is used in the plasma potential model, as shown previously in the electron model flowchart in Fig. 6.4, we

also conclude convergence of the plasma potential.

Thus the electron model has reached a converged solution which can be used in the next step of the heavy species solver. While this demonstration of numerical convergence is necessary for verification, in practice larger values of the residual are acceptable. Therefore fewer iterations are necessary before passing the temperature and potential information to the heavy species solver.
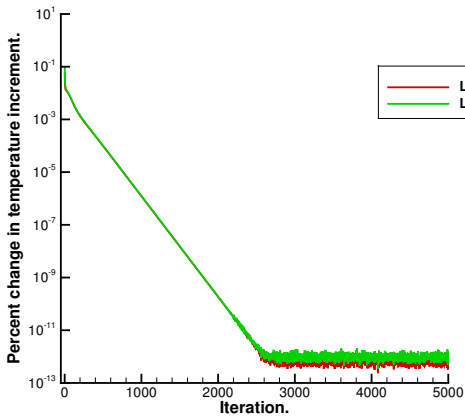
Figure 6.10: Electron temperature convergence is achieved after the 2600th iteration for a timestep of 5 ns for a strictly radial magnetic field.

We next follow the same process as described above, but with a curved magnetic field of the same magnitude. Figure 6.11(a) shows that for a curved magnetic field a timestep of 5 ns is too large, and while the temperature residual is bounded, it is not decreasing, and the value is large. We decrease the timestep, and for a value of 0.1 ns we observe the L_1 and L_2 norms decrease to a negligible value in Fig. 6.11(b).
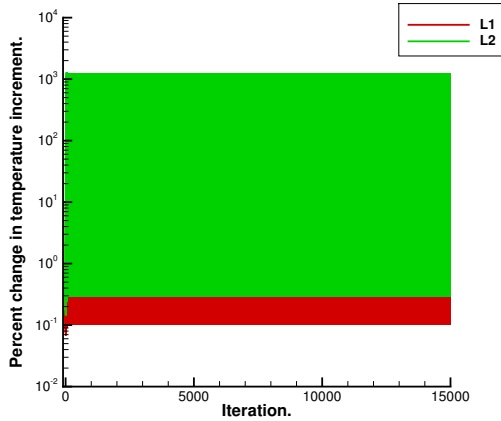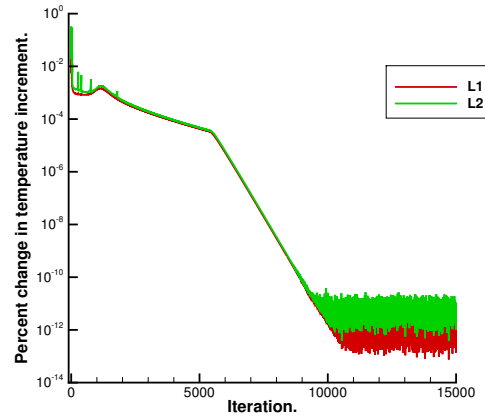
(a) Δt= 5 ns. (b) Δt= 0.1 ns.

Figure 6.11: Electron temperature convergence is achieved after 11,000 iterations for a curved magnetic field, and timestep of 0.1 ns, while using a large timestep of 5 ns as in the case where $B_z = 0$ gives a diverging solution.

6.7 Hybrid-PIC with 2D Electrons

The 2D electron standalone model has been developed in a modular fashion, thus allowing independent evaluation of its components [19]. First the plasma potential solver was verified by benchmarking in previous work [22] and current conservation was shown in Section 6.6.1. Next, the electron energy solver is verified in Section 6.6.2. Finally, the convergence test presented in Section 6.6.3 confirms that the standalone 2D electron model has been developed to a point where it may be coupled with a heavy species model.

The newly developed standalone 2D axisymmetric electron model is next implemented within the HPHall framework. The plasma potential and electron energy solvers are included directly as in the standalone model, with the addition of ionization losses and thermal heat-exchange losses for the energy equation, which were neglected previously. The user may select either the quasi-1D model, or the updated 2D axisymmetric electron model. A benchmarking test case is described in Section 6.7.1, while the results are presented in Section 6.7.2. The test case is selected such that the

157

results between the quasi-1D and 2D models should be similar.

6.7.1   Setup

A thruster channel-like test case is prepared. The domain extends axially from 0 to 0.025 m, and radially from 0.035 to 0.05 m. The anode is on the west boundary, the cathode on the east boundary, and the north and south boundaries are treated as dielectric walls. The magnetic field is strictly radial, with a maximum magnitude of 158 G. This test case is similar to the low magnitude radial magnetic field case shown in Section 6.6.1, and used in previous benchmarking work [22].

The plasma potential is set to 300 V at the anode and 0 V at the cathode, while the electron temperature is set to 1 eV at both the anode and cathode. The mass flow rate is 7 mg/s. Chamber background pressure is not included. Anomalous mobility parameter modeling is also not included ($\alpha = 0$).

Figure 6.12(a) shows the 51 X 31 2D Cartesian mesh used by both the PIC algorithm and the 2D electron model. The computational mesh used by the quasi-1D electron model follows the magnetic field lines, and it is shown for comparison in Fig. 6.12(b). To ensure a one-to-one comparison between the two models, the line-bunching algorithm in HPHall is suppressed, and the quasi-1D domain is generated such that each field line (51 in total) is represented.
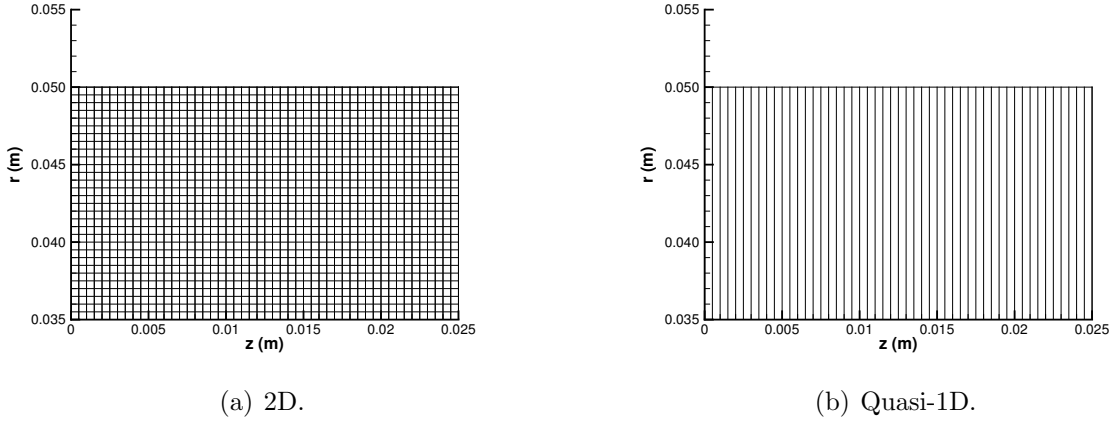
Figure 6.12: The computational mesh for the 2D and quasi-1D electron models. The heavy species PIC mesh coincides with the Cartesian mesh used for the 2D electron model.

6.7.2 Results

6.7.2.1 Short Simulation: 5 μs

Two analogous hybrid-PIC simulations are performed to evaluate the 2D and quasi-1D electron models. The heavy species timestep is 5 ns, and the total physical time simulated is 5 μs. The hybrid-PIC simulations are preconditioned [18] by first populating the domain with neutrals (20,000 iterations), and then ions (1,000 iterations), before initializing heavy species collisions which we then run for another 1,000 iterations.

Time-averaged spatial distributions of the plasma potential (Fig. 6.14) and electron temperature (Fig. 6.15) are generated with both the quasi-1D model and 2D electron model, however the 2D model uses a timestep that is ten times larger than that used in the quasi-1D results (Δ t = 50 ps).

The behavior at the boundaries appears different due to the fact that the 2D model

(a) Plasma potential.

(b) Electron temperature.

Figure 6.13: The time-averaged plasma potential and electron temperature computed by the 2D and quasi-1D electron models within the hybrid-PIC framework, extracted at the channel centerline.

solves for variables on the cell-centers, while the quasi-1D model works on the nodes. Thus, in the 2D model the cell-centered values must be extrapolated to the nodes, and in the present case a zeroth order extrapolation is used at the wall boundaries which is responsible for the differences seen in that region. However, the dielectric wall boundary is imposed within the cell-centered solver. An improved extrapolation technique is expected to show better agreement between the 2D and quasi-1D spatial distributions at the wall. Good agreement is observed at the centerline, as also shown in Fig. 6.13(a).

The electron temperature shows similar behavior between the 2D and quasi-1D electron models, however the increase in temperature appears to be more gradual for the 2D case. This behavior is also observed in the centerline value extracted in Fig. 6.13(b).

As discussed in Section 6.3.3, the 2D model uses a semi-implicit discretization in time which comes with enhanced stability properties. This is further verified in Section

(a) 2D.
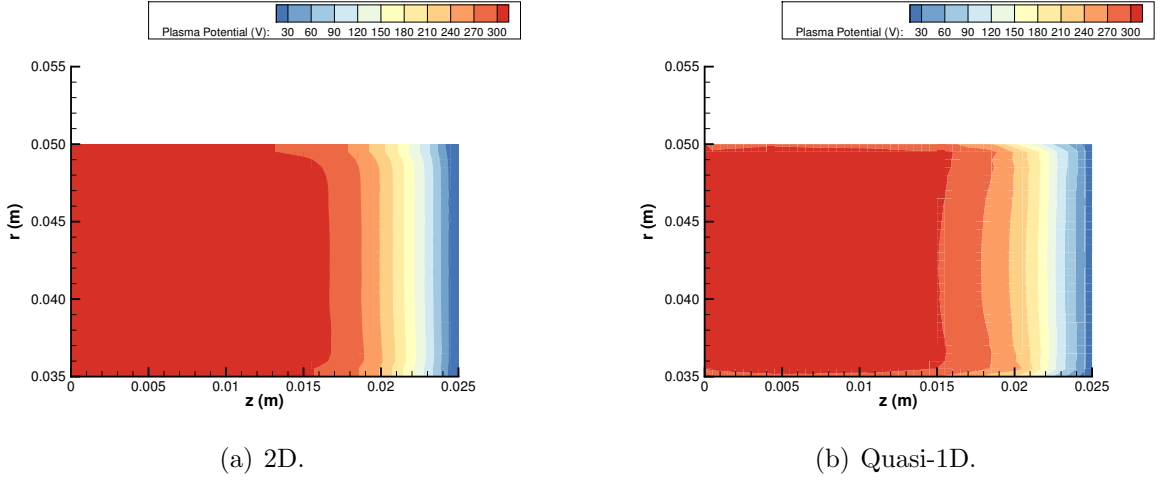
(b) Quasi-1D.

Figure 6.14: The time-averaged plasma potential computed by the 2D and quasi-1D electron models within the hybrid-PIC framework for 5 μ s of physical time.

6.6.2 for a "toy problem". On the other hand, the quasi-1D electron model uses an explicit discretization in time [24], which places limits on the timestep size. This is observed directly with the thruster channel-like test case.

The largest stable electron timestep that may be used with the quasi-1D model without generating instabilities and having the simulation crash is 5 ps and is one thousand times smaller than the heavy species timestep. However, in this particular case, the 2D electron model may run stably with timesteps as large as the heavy species timestep. Moreover, for this test case the 2D electron submodel outputs, plasma potential and electron temperature, are insensitive to the choice of timestep, as shown in Figs. 6.13(a) and 6.13(b), respectively. Additionally, the wall time values are summarized in Table 6.3. It is notable that when running the 2D model at a timestep of 5 ns we are able to complete the simulation 20% faster than when using the quasi-1D model. However, the 2D model becomes more expensive than the quasi-1D option as we consider lower timestep values: 20% more expensive for 50 ns, 4 times more expensive when using 0.5 ps and 40 times more expensive for 5 ps. Without the time-

implicit scheme the 2D model would have to run at a much lower timestep which would make it significantly more expensive than its quasi-1D counterpart.

Table 6.3: Wall time for different timestep values.

timestep (s)	electron model	wall time (s)
5×10^{-09}	2D-axi	576
5×10^{-10}	2D-axi	907
5×10^{-11}	2D-axi	3618
5×10^{-12}	2D-axi	36,363
5×10^{-12}	quasi-1D	723

(a) 2D.

(b) Quasi-1D.

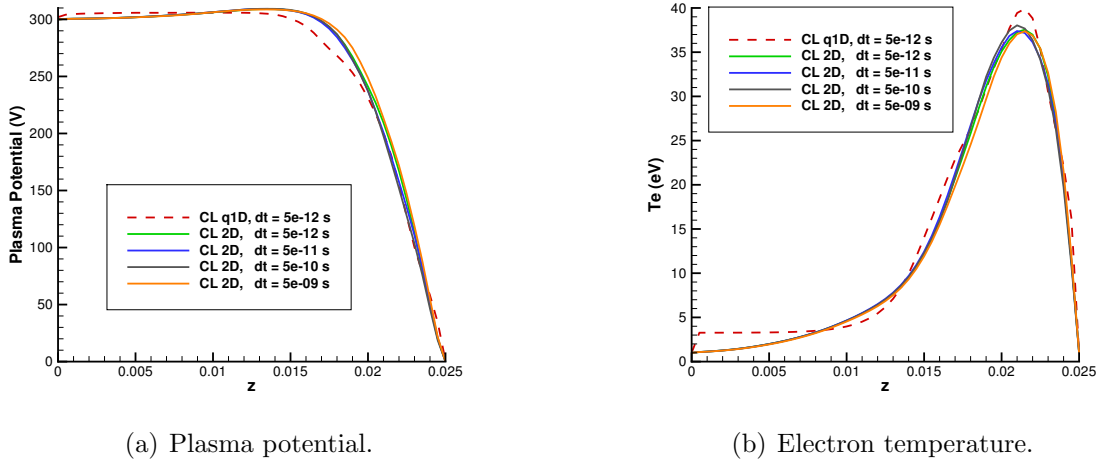Figure 6.15: The time-averaged electron temperature computed by the 2D and quasi-1D electron models within the hybrid-PIC framework for 5 μs of physical time.

Figure 6.16 shows the time evolution of the thruster discharge current. The values are similar for the 2D electron model, regardless of timestep choice. However the quasi-1D result produces lower current values in the initial stages (up to 2 μs). This is in part due to the pre-conditioning stages which give different starting values of current for the two models. As the simulation time approaches 5 μs all results converge towards a similar value of current.

162

Figure 6.16: Time evolution of the discharge current computed by the 2D and quasi-1D electron models within the hybrid-PIC framework for 5 μs of physical time.

6.7.2.2 Longer Simulation: 100 μs

Here we use the same test case in Section 6.7.2.1, but we simply run the final stage for 20,000 steps instead of just 1,000. Furthermore, the 2D model is running with an electron timestep of 0.5 ns, while the quasi-1D model is using the same 5 ps timestep as in the previous section.

In addition, the cell-centered values are extrapolated to the boundary nodes with a first order scheme as opposed to the zeroth order extrapolation from the previous section, and the improvement may be seen in Fig. 6.17(a) near the dielectric walls. However, Figure 6.17 also shows shows that the 2D model maintains a higher potential farther in the plume that the quasi-1D model, which translates to smoother gradients that may also be due to the extrapolation. We also note from Fig. 6.17(b) that after averaging over a larger number of iterations the quasi-1D model finally produces plasma potential contours that are aligned with the magnetic field, unlike what was observed in Fig. 6.14(b) for the 5 μs simulation.

The electron temperature also shows smoother gradients when computed with the 2D

163

model, versus the quasi-1D time-averaged result shown in Figure 6.18. As observed in the 5 μs results, the 2D model produces a lower temperature than the quasi-1D, which may be due to smoothing from the repeated interpolations when passing information between the nodes and cell centers.

Finally, the time dependent discharge current is shown in Fig. 6.19 in red for the quasi-1D model and in red for the 2D model. We notice that both models follow a similar trend, starting with a high value of current, then decreasing to a minimum and then gradually increasing again. However, the quasi-1D model is beginning to exhibit low amplitude oscillations whereas the 2D model does not display any visible oscillations. Recent efforts by Raisanen [81] have shown that the discharge current oscillations are highly sensitive to the choice of electron wall loss model, therefore future work should be directed towards modeling the wall losses accurately.

(a) 2D.
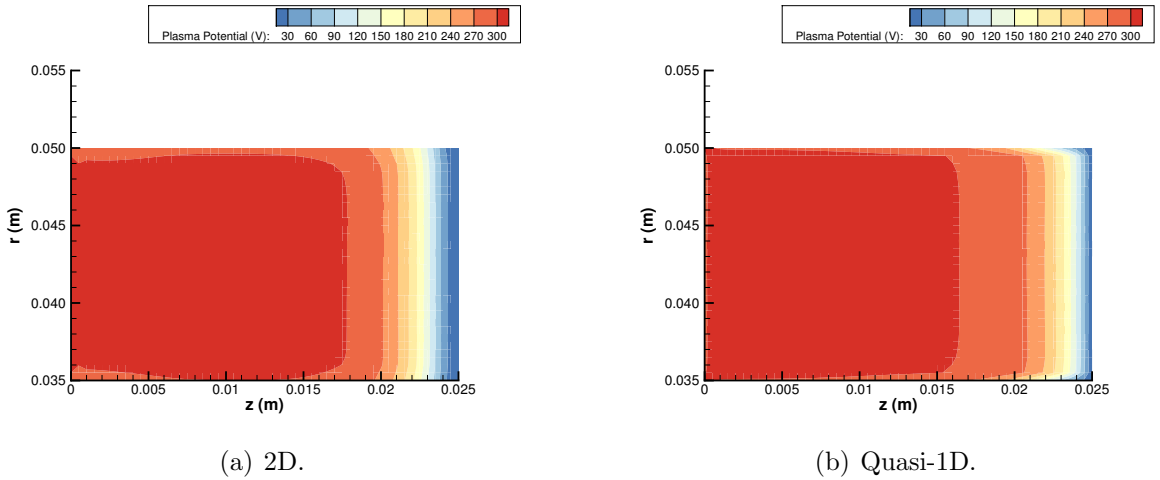
(b) Quasi-1D.

Figure 6.17: The time-averaged plasma potential computed by the 2D and quasi-1D electron models within the hybrid-PIC framework for 100 μs of physical time.
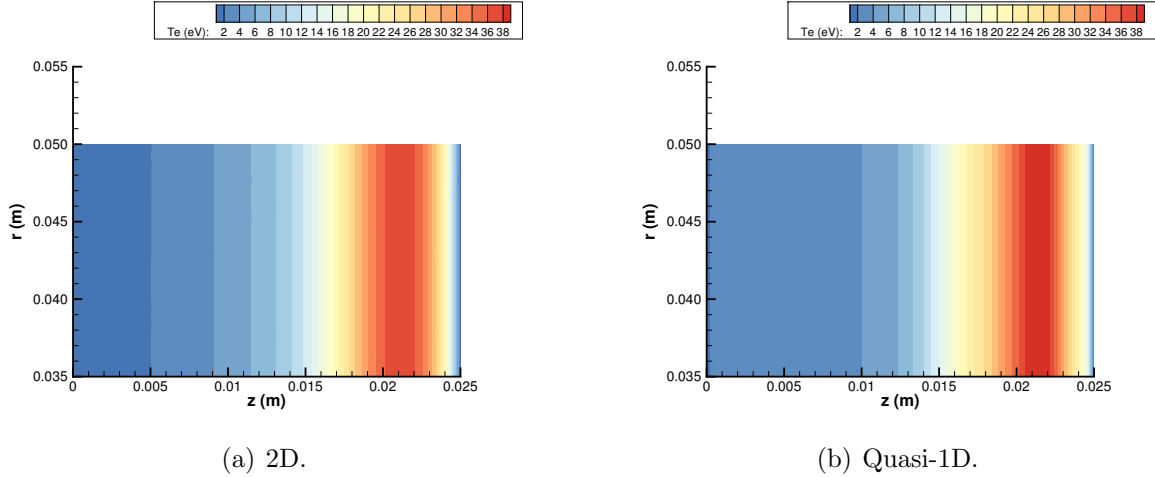
(a) 2D.
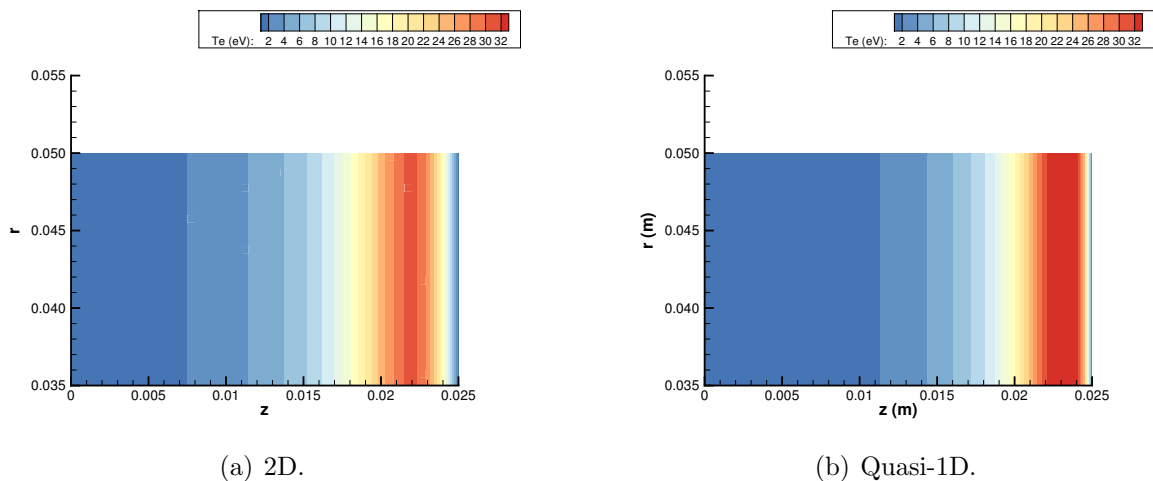
(b) Quasi-1D.

Figure 6.18: The time-averaged electron temperature computed by the 2D and quasi-1D electron models within the hybrid-PIC framework for 100 μs of physical time.
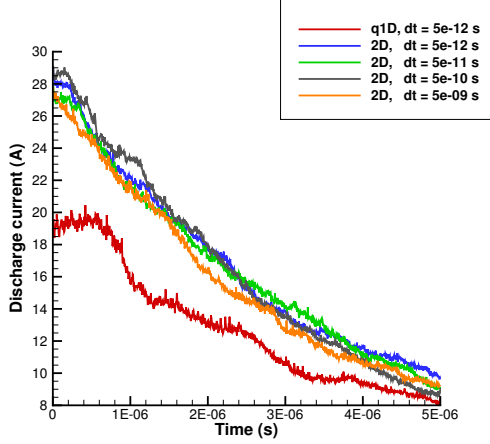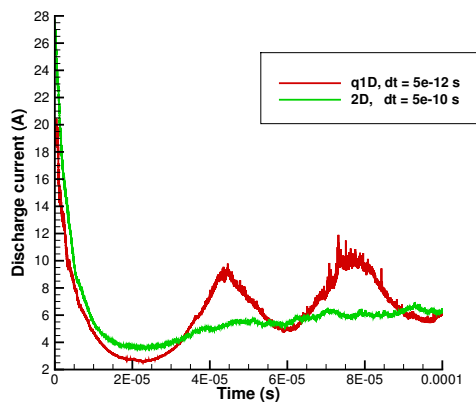

Figure 6.19: Time evolution of the discharge current computed by the 2D and quasi-1D electron models within the hybrid-PIC framework for 100 μs of physical time.

6.8   Summary

A standalone 2D axisymmetric electron model was presented. It is composed of a plasma potential solver and an electron energy solver. The plasma potential solver was verified by evaluating electron current conservation. The energy solver was verified against an analytic solution for a simplified problem with both isotropic and anisotropic thermal conductivities. The first order in time convergence rate was confirmed as expected, and the stability properties of the semi-implicit scheme were also tested. Next, convergence of the standalone 2D electron model was shown for a Hall thruster channel-like test case with a purely radial magnetic field. Finally, the 2D electron model was coupled with an existing heavy species PIC solver in a hybrid-PIC framework, and further evaluated through benchmarking against the pre-existing quasi-1D electron model. It was shown that the 2D and quasi-1D models produce similar physical results for a test case with a strictly radial magnetic field. Moreover, the advantage of using a semi-implicit time integration scheme was demonstrated as the 2D model was stable for timesteps that were three orders of magnitude larger than required in the quasi-1D model. For a short (5 μs) simulation time it was observed that the quasi-1D model produces average values of plasma potential that are not aligned with the magnetic field, however for longer simulations, this is no longer the case. On the other hand, the 2D electron model produced plasma potential values aligned with the magnetic field for both long and short simulations, and thus may be better suited for instantaneous computations as well as longer term simulations.

CHAPTER VII

Conclusions

7.1 Dissertation Summary

The current work has advanced the Hall thruster simulation state-of-the-art in several different directions. We started by introducing three different modeling approaches: full-fluid, direct simulation Monte Carlo, and hybrid-particle-in-cell. These approaches were then applied to study several problems related to the latest experimental advances in the field of high-power thruster development. In addition, a new 2D-axisymmetric electron submodel was constructed to address the shortcomings of the existing quasi-1D electron fluid model used within the hybrid-PIC framework.

When considering high-power Hall thrusters, three critical problems must be approached. First, higher power devices require larger flow rates which in turn leads to increased costs related to propellant use. Second, when using higher power devices we must consider that we are adding more energy into the system which can accentuate the erosion of surfaces and this is a potential end-of-life mechanism. Finally, recently developed high-power devices are designed with non-conventional geometries and complex magnetic fields, for example in the case of nested-channel Hall thrusters. It is critical that we gain a better physical understanding of these new thruster configurations, and explore new phenomena such as channel-to-channel interaction in a

NHT.

First, the problem of propellant cost was addressed by considering an alternative to the standard xenon gas. Thus, krypton propellant was implemented in the multi-fluid simulation framework Hall2De. The model was validated for the NASA-300M thruster by comparison with experimental performance measurements for the 400 V and 50 A operating condition. Thrust was computed to within 6% of the measured value for xenon operation, and within the experimental error of 2% for krypton operation. Next, the H6US thruster which to date has only operated with xenon propellant was simulated with the newly implemented krypton model. A simple thruster model was used to estimate the expected performance for krypton operation, and the trends observed from the full-fluid simulation were consistent between the two thrusters, and simplified model. While the thrust values observed for krypton operation were lower in all cases, the specific impulse was consistently higher since operating the thruster at the same power requires a lower flow rate for krypton. In conjunction with the new capability for numerical simulation, laboratory krypton testing may provide a less expensive option for Hall thruster investigations or qualification tests.

Second, the issue of channel wall erosion was considered. A recent optical diagnostic technique used to measure sputtered material in the plume of a Hall thruster was simulated numerically. The modeling approach produced a similar qualitative trend but overpredicted the measurements by a factor of 3. This may be reduced in the future, as described in Section 7.3. While in the current work we only presented an application of this technique to a legacy SPT-70 thruster, it has also been applied successfully to the High Voltage Hall Accelerator (HiVHAc) thruster [93, 57] and may further be extended to high-power devices. In addition, Hall2De was used to estimate the erosion rate for several NASA-300M thruster surfaces, for both xenon and

krypton. The conclusions were based on the incident ion current density to thruster surfaces, and while for the channel walls, the erosion rates are expected to be similar to within 10%, a significant difference was observe on the inner pole piece. At that location the Xe propellant produced higher erosion rates by a factor of 1.7 when compared to Kr. Finally, the outer pole piece erosion was also examined and while the Kr erosion rate was estimated to be twice as large as for Xe, the magnitude was four orders of magnitude smaller than for the other surfaces studied, so this effect is less significant.

Third, two different computational models were used to study the X2 nested channel Hall thruster. Initially a neutrals-only simulation was used to evaluate the near-field pressure distribution and compute the number densities of xenon originating from the two different channels. These values were further combined with experimental data from PEPL to explain the anomalous thrust increases observed initially for this device during development. Next, a plasma simulation of the inner-channel thruster operation was performed and thrust was matched to within 9%, while discharge current was matched to within 5% of the measured values. The sensitivity of the simulation to various parameters was tested and it was concluded that the value of the anomalous transport parameter in the plume region had the largest effect on the final performance results, while the inclusion of CEX collisions, and changes in number of simulation particles had less of an effect on the results. It was also determined that a new electron model is required in order to simulate the complicated geometry and magnetic fields encountered during dual channel thruster operation.

Fourth, a new 2D-axisymmetric non-magnetic-field-aligned electron model was developed in a modular fashion. Initially, a plasma potential solver was created, and then verified by showing current conservation for a series of Hall thruster channel-

like test cases with various magnetic field topologies. Next, a solver for the electron energy equation was implemented, and it was verified using a simplified problem - the anisotropic 2D heat equation - that yielded an analytic solution which was then compared to the computational result. The two solvers were then combined to form the standalone electron model which can solve the fluid conservation equations for electrons when given information regarding the heavy species in the plasma. Convergence of this combined model was further demonstrated by measuring the change in the value of electron temperature from one iteration to the next. Once the standalone model was verified, it was integrated within an existing hybrid-PIC framework, and a benchmarking test case was used to evaluate model performance. Since the discretization for the new model is Cartesian, and not magnetic-field aligned, for a purely radial magnetic field, we expected to see identical results between a computation performed with the quasi-1D model and the 2D model. This was confirmed to be true, along with improved stability over the quasi-1D model which is due to the semi-implicit time discretization used in the new model. For the test case that was used, we were able to solve the electron equations within a single time-step when using the hybrid-PIC model with 2D electrons, while for the quasi-1D submodel 1000 timesteps were needed to avoid the onset of instabilities.

7.2   Unique Contributions

1. All the necessary cross-sections to successfully include krypton as a species in a Hall thruster plasma model have been conveniently compiled in this work.

2. The simulation of a thruster that was never run on krypton may be used to estimate mass savings before a potential laboratory test. This technique was illustrated in the present work for the H6US, and may be extended to other

170

thrusters.

3. The Hall2De framework may also be used to estimate erosion rates and in the present case this was applied to Xe and Kr simulations of the NASA-300M.

4. The experimental procedure for the cavity-ring-down spectroscopy diagnostic was simulated and this technique may be applied to any unshielded thruster with boron nitride (or similar) dielectric walls to estimate the erosion rate and thus predict the thruster lifetime.

5. The neutral density distribution for a nested channel Hall thruster operating in dual-channel mode was computed, and used in conjunction with experimental measurements to confirm neutral ingestion is a plausible cause for anomalous thrust increase in multi-channel operation of a NHT.

6. A plasma simulation of the independent inner channel operation of the X2 NHT has shown that it is possible to match thrust within 10% and discharge current within 5% when using a hybrid-PIC method.

7. The development of a 2D axisymmetric electron model and its integration within the hybrid-PIC framework enables new research into the complex physics of Hall thrusters. In particular, deviations from the magnetic field isothermality may be captured, and simulations of thrusters with complex magnetic fields can easily be prepared, since the tedious step of aligning the mesh to the magnetic field has been eliminated.

7.3   Future Work

The krypton simulation results presented in Chapter III may be improved by obtaining the precise magnetic field configuration for all the NASA-300M test points. This would enable a larger parametric study over various thruster operating conditions. In

addition, electron temperature measurements for a thruster operating with krypton may improve our validation of the numerical results for other operating conditions. Furthermore, ion current fraction data would help validate the ionization model implemented in Hall2De for krypton propellant. Another direction for future research is to investigate the erosion rates on thruster pole pieces, the cathode, or for unshielded HETs, the channel walls. Due to lower ion densities in the near-field plume, one may expect to find lower erosion rates with a krypton propellant compared to that observed for xenon. A first step in this present work was to evaluate the incident ion current densities at the thruster surfaces, and the erosion rate is directly proportional to this parameter. However, the erosion rate is also proportional to the sputter yield which is a function of the ion energy and incidence angle. Future research should focus on determining the sputter yield, and this information combined with the incident ion current density presented in this work will yield the surface erosion rates.

There are several aspects of the erosion study from Chapter IV that may warrant further work in order to improve the correspondence between simulation and measurement. First, the VDF of the sputtered boron used in the simulation is obtained from a MD simulation conducted at 100 eV energy and 45° angle of incidence. Smith [91] has conducted further MD studies to understand the dependence of sputter yield on ion energy and incidence angle. The boron sputter yield was found to increase with incidence angle, reaching its maximum between 60° and 70° for a fixed 100 eV energy ion impact, followed by a steep decrease between 70° and normal. Additionally, for a fixed normal incidence angle, the sputter yield was found to increase with ion energy. These trends suggest that with lower incidence angle and/or lower ion energy, the ceramic wall sputter yield will be lower, which may help improve agreement in the present work with the CRDS data. Finally, there is considerable uncertainty in the total thruster operation time that is estimated at ±50%. This value then translates

to a $\pm 50\%$ uncertainty in the estimated erosion rate which is used as an input for the simulation. Therefore the thruster should be operated at a fixed point for several hours to significantly reduce the uncertainty in this critical parameter.

The technique presented in this work may be used to generate a database of line-integrated boron number density profiles that correspond to various erosion rates. The experimentally measured profile may then be compared to the database to identify the wall erosion rate.

The nested-channel HET study presented in Chapter V may be continued with a series of plasma simulations of the independent inner and outer channel operation and also dual channel operation. One goal would be to replicate the thrust gains observed experimentally. A secondary goal should be to identify any additional channel interaction mechanisms. In particular, the location of the ionization zone should be compared between independent and dual-channel operation, as well as the discharge current oscillations. However, in order to prepare a physical setup for the simulation additional experimental data must be collected, such as plasma potential, the electron temperature, and a map of the Hall parameter.

Additional benchmarking of the hybrid-PIC model with 2D axisymmetric fluid electrons from Chapter VI with simplified HET-like test cases is required before advancing to full thruster simulations. The next step is to investigate solutions for curved magnetic fields where the differences between the 2D and quasi-1D models are expected to become more visible. Further work is also required to evaluate various boundary conditions and wall loss effects on the simulation. Moreover, plume test cases must also be evaluated to ensure that the appropriate plume boundary conditions are identified. Finally, additional studies of the discharge current oscillations should also be

performed with a particular focus on eliminating spurious oscillations and attempting to reproduce physical ones from a well-characterized device, such as the H6US.

APPENDICES

APPENDIX A

Estimate of full-PIC Computational Cost

For a SPT-100 setup (only inside the discharge channel), the geometry is as follows:

- Axial: $L_x = 2.5$ cm

- Radial: $L_r = 1.5$ cm

- Azimuthal: $L_\theta \approx 20$ cm

Next, assume typical values of the temperature and plasma density: $T_e = 10$ eV and $n = 10^{17}$ m^{-3}.

We compute the Debye length:

$$\lambda_D = \sqrt{\frac{\epsilon \times k_B \times T_e}{e^2 \times n}}$$

$$= 10^{-5} \text{ m}$$

To resolve the Debye length in all three dimensions, the total number of cells must be on the order of $N_{cells} = 7.5 \times 10^{10}$. The timestep can be estimated as follows:

$$dt = \frac{\lambda_D}{v_{th}}$$

This gives dt = 1 ns. For ten breathing mode cycles, a simulation of 1 ms is required which translates into 10^6 iterations. Assuming 100 total particles per cell (including electrons, ions, and neutrals), the total number of particles is $N_p = 7.5 \times 10^{12}$. Because the particle count is 100 times the cell count, the storage requirements for the mesh are ignored. For each particle, 7 *doubles* (3 for position, 3 for velocity, 1 for mass) and 1 *int* must be stored, which gives us:

$$60 \text{ B/particle} \times 7.5 \times 10^{12} \text{ particles} = 4.5 \times 10^{14} \text{ B}$$

$$= 450 \text{ TB of required memory}$$

A multidimensional full-PIC code with a state-of-the-art Poisson solver was not available, so an assumption is made that the Poisson solver makes up most of the computational cost. Then, assuming a Successive Over-Relaxation (SOR) technique, the required number of numerical operations required for convergence given a desired level of accuracy from [38] is $N_{operations} = 22 \times (N_{cells})^{4/3}$ for a desired residual of 10^{-6}, or about 7×10^{15} SOR operations per time step. Finally, assuming a processor with 100 GFLOPS per core, similar to the Intel Core i9 7900X[54], the wall time is estimated as:

$$\frac{7 \times 10^{15} \text{ ops/it}}{10^{11} \text{ ops/s}} \times 10^9 \text{ its} = 7 \times 10^{13} \text{ s}$$

$$= 2.2 \times 10^6 \text{ years}$$

APPENDIX B

Mathematics Review

We first define several vector identities in cylindrical coordinates.

Gradient of scalar a:

$$\nabla a = \frac{\partial a}{\partial r}\hat{r} + \frac{\partial a}{\partial z}\hat{z} + \frac{1}{r}\frac{\partial a}{\partial \theta}\hat{\theta} \tag{B.1}$$

Divergence of vector $\vec{A}$:

$$\nabla \cdot \vec{A} = \frac{1}{r}\frac{\partial (rA_r)}{\partial r} + \frac{\partial A_z}{\partial z} + \frac{1}{r}\frac{\partial A_\theta}{\partial \theta} \tag{B.2}$$

Next we define the L_1 and L_2 norms for a 2D array A of size $m \times n$:

$$L_1 = \sum_{i=0}^{m}\sum_{j=0}^{n} \frac{A[i][j]}{m \times n} \tag{B.3}$$

$$L_2 = \sqrt{\frac{\sum\limits_{i=0}^{m}\sum\limits_{j=0}^{n} \left(A[i][j]\right)^2}{m \times n}} \tag{B.4}$$

Here we define the Taylor series expansion of a function f(x) at $(x+\Delta x)$ and $(x-\Delta x)$:

$$f(x + \Delta x) = f(x) + \Delta x f'(x) + \frac{\Delta x^2}{2!} f''(x) + \frac{\Delta x^3}{3!} f'''(x) + \ldots \tag{B.5}$$

$$f(x - \Delta x) = f(x) - \Delta x f'(x) + \frac{\Delta x^2}{2!} f''(x) - \frac{\Delta x^3}{3!} f'''(x) + \ldots \tag{B.6}$$

APPENDIX C

Analytic Solution for Anisotropic Heat Equation

Here we present the steps used to reach the analytic solution for the anisotropic heat equation. We are following the approach presented by [33] for a different problem setup. The equation we are solving is:

$$u_t = \kappa_x \cdot u_{xx} + \kappa_y \cdot u_{yy} \; , \; 0 \le x \le L, \; , \; 0 \le y \le H \tag{C.1}$$

The boundary conditions are:

$$u(0, y, t) = 0 = u(L, y, t) = u(x, 0, t) \; ; \; \frac{\partial u}{\partial y}(x, H, t) = 0 \tag{C.2}$$

The initial condition is:

$$u(x, y, 0) = 100 \tag{C.3}$$

We start by using separation of variables:

$$u(x, y, t) = X(x)Y(y)T(t) \tag{C.4}$$

We may now rewrite the PDE as:

$$\frac{T'(t)}{T(t)} = \kappa_x \frac{X''(x)}{X(x)} + \kappa_y \frac{Y''(y)}{Y(y)} \tag{C.5}$$

Since the left hand side is dependent on t and independent of x and y, while the right hand side is dependent on x and y, and independent of t it must be that both sides should equal a constant. We define this separation constant as $-\lambda$:

$$\frac{T'(t)}{T(t)} = -\lambda \tag{C.6}$$

$$\kappa_x \frac{X''(x)}{X(x)} + \kappa_y \frac{Y''(y)}{Y(y)} = -\lambda \tag{C.7}$$

Thus, from Eq. C.6:

$$T(t) = ce^{-\lambda t} \tag{C.8}$$

From the boundary conditions we find:

$$u(0, y, t) = 0 \Rightarrow X(0) = 0 \tag{C.9}$$

$$u(L, y, t) = 0 \Rightarrow X(L) = 0 \tag{C.10}$$

$$\frac{du}{dy}(x, 0, t) = 0 \Rightarrow Y'(0) = 0 \tag{C.11}$$

$$\frac{du}{dy}(x, H, t) = 0 \Rightarrow Y'(H) = 0 \tag{C.12}$$

Now consider Eq. C.7:

$$\kappa_y \frac{Y''(y)}{Y(y)} + \lambda = -\kappa_x \frac{X''(x)}{X(x)} \tag{C.13}$$

Following the same reasoning as above, the left hand side and right hand side must equal a constant, μ:

$$\kappa_y \frac{Y''(y)}{Y(y)} + \lambda = -\kappa_x \frac{X''(x)}{X(x)} = \mu \tag{C.14}$$

181

We focus on $X(x)$:

$$X''(x) + \frac{\mu}{\kappa_x} X(x) = 0 \text{ and } X(0) = X(L) = 0 \tag{C.15}$$

The solution is:

$$X_n(x) = \sin\left(\frac{n\pi x}{L}\right), \ \mu_n = \kappa_x \left(\frac{n\pi}{L}\right)^2, \ n = 1, 2, 3, ... \tag{C.16}$$

Next we consider $Y(y)$:

$$Y''(y) + \frac{\mu}{\kappa_y} Y(y) = 0 \text{ and } Y(0) = Y'(H) = 0 \tag{C.17}$$

We try:

$$Y_m(y) = -\sin\left((m - 1/2)\pi \frac{y}{H}\right) \tag{C.18}$$

$$Y'_m(y) = -\frac{H}{\pi(m - 1/2)} \cos\left((m - 1/2)\pi \frac{y}{H}\right) \tag{C.19}$$

$$Y''_m(y) = -\left(\frac{H}{\pi(m - 1/2)}\right)^2 \left[-\sin\left((m - 1/2)\pi \frac{y}{H}\right)\right] \tag{C.20}$$

Equation C.17 gives:

$$\frac{\lambda_{m,n} - \mu_n}{\kappa_y} = \left(\frac{\pi(m - 1/2)}{H}\right)^2 \tag{C.21}$$

$$\Rightarrow \lambda_{m,n} = \kappa_y \left(\frac{\pi(m - 1/2)}{H}\right)^2 + \mu_n \tag{C.22}$$

$$= \kappa_x \left(\frac{n\pi}{L}\right)^2 + \kappa_y \left(\frac{\pi(m - 1/2)}{H}\right)^2 \tag{C.23}$$

Thus, the particular solution to the original equation may be expressed as:

$$u_{m}n(x, y, t) = \sin\left(\frac{n\pi x}{L}\right) \left[-\sin\left((m - 1/2)\pi \frac{y}{H}\right)\right] e^{-\lambda_{m,n} t} \tag{C.24}$$

We apply superposition to obtain the general solution by summing over all m and n:

$$u(x, y, t) = \sum_{m=1}^{\infty} \sum_{n=1}^{\infty} A_{m,n} \sin\left(\frac{n\pi x}{L}\right) \left[-\sin\left((m - 1/2)\pi \frac{y}{H}\right)\right] e^{-\lambda_{m,n}t} \qquad \text{(C.25)}$$

To calculate $A_{m,n}$ we impose the initial condition, $u(x, y, 0) = 100$:

$$A_{m,n} = \frac{4}{LH} \int_{x=0}^{L} \int_{y=0}^{H} 100 \sin\left(\frac{n\pi x}{L}\right) \left[-\sin\left((m - 1/2)\pi \frac{y}{H}\right)\right] \qquad \text{(C.26)}$$

$$= -\frac{800}{n(2m - 1)\pi^2} \left(1 - (-1)^n\right) \Rightarrow A_{m,2n} = 0 \qquad \text{(C.27)}$$

$$A_{m,2n-1} = -\frac{1600}{(2n - 1)(2m - 1)\pi^2} \qquad \text{(C.28)}$$

The general solution is then:

$$\boxed{u(x, y, t) = \sum_{m=1}^{\infty} \sum_{n=1}^{\infty} A_{m,2n-1} \sin\left(\frac{(2n - 1)\pi x}{L}\right) \cos\left(\frac{(2m - 1)\pi y}{2H}\right) e^{-\lambda_{m,2n-1}t}} \qquad \text{(C.29)}$$

where:

$$\lambda_{m,2n-1} = \kappa_x \left(\frac{(2n - 1)\pi}{L}\right)^2 + \kappa_y \left(\frac{\pi(2m - 1)}{2H}\right)^2 \qquad \text{(C.30)}$$

BIBLIOGRAPHY

[1] B. A. Archipov, L. Z. Krochak, and N. A. Maslennikov. Thermal design of the electric propulsion system components: numerical analysis and testing at FAKEL. In *34th AIAA/ASME/SAE/ASEE Joint Propulsion Conference and Exhibit*, pages AIAA 98–3489, 1998.

[2] E. W. Bell, N. Djurić, and G. H. Dunn. Electron-impact ionization of In+ and Xe+. *Physical Review A*, 48(6):4286–4291, 1993.

[3] P. L. Bhatnagar, E. P. Gross, and M. Krook. A model for collision processes in gases. I. Small amplitude processes in charged and neutral one-component systems. *Physical Review*, 94(3):511–525, 1954.

[4] G. A. Bird. *Molecular Gas Dynamics and the Direct Simulation of Gas Flows*. Oxford University Press, Oxford, England, UK, 1994.

[5] C. K. Birdsall and A. B. Langdon. *Plasma Physics via Computer Simulation*. IOP Publishing, 1991.

[6] I. D. Boyd and T. E. Schwartzentruber. *Nonequilibrium Gas Dynamics and Molecular Simulation*. Cambridge University Press, 2017.

[7] I. D. Boyd, D. B. Van Gilder, and X. Liu. Monte Carlo Simulation of Neutral Xenon Flows in Electric Propulsion Devices. *Journal of Propulsion and Power*, 14(6):1009–1015, 1998.

[8] John Brophy. Technology for a robotic Asteroid Redirect Mission and its extensibility to future human and robotic missions. In *IEEE Aerospace Conference Proceedings*, volume 2015-June, 2015.

[9] Daniel L. Brown and Alec D. Gallimore. Evaluation of Facility Effects on Ion Migration in a Hall Thruster Plume. *Journal of Propulsion and Power*, 27(3):573–585, May 2011.

[10] Daniel L. Brown, Bryan M. Reid, Alec D. Gallimore, Richard Robert Hofer, and James M. Haas. Performance Characterization and Design Verification of the ## Laboratory Model Hall Thruster. In *54th JANNAF Propulsion Meeting*, Denver, CO, 2007.

[11] David Byers and John W. Dankanich. A Review of Facility Effects on Hall Effect Thru. In *Proceedings of the 31st International Electric Propulsion Conference*, Ann Arbor, MI, 2009.

[12] S. Chapman and T. G. Cowling. *The mathematical theory of non-uniform gaseous expansions.* Cambridge University Press, 2nd edition, 1952.

[13] S. Cho, S. Yokota, K. Hara, D. Takahashi, Y. Arakawa, K. Komurasaki, and A. Kobayashi. Hall Thruster Channel Wall Erosion Rate Measurement Method Using Multilayer Coating Chip. In *AIAA Joint Propulsion Conference and Exhibit.*, AIAA 2010-6697, July 2010.

[14] Maria Choi and Iain D. Boyd. Numerical Simulation of the Cathode Plume of a Hall Thruster. In *50th AIAA/ASME/SAE/ASEE Joint Propulsion Conference*, Reston, Virginia, jul 2014. American Institute of Aeronautics and Astronautics.

[15] Sarah E. Cusson, Marcel P. Georgin, Horatiu C. Dragnea, Ethan T. Dale, Vira Dhaliwal, Iain D. Boyd, and Alec D. Gallimore. On channel interactions in nested Hall thrusters. *Journal of Applied Physics*, 123(13):133303, apr 2018.

[16] C. J. Dasch. One-dimensional tomography: a comparison of Abel, onion-peeling, and filtered backprojection methods. *Appl. Opt.*, 31(8):1146–1152, 1992.

[17] Stefan Dietrich and Iain D. Boyd. Scalar and Parallel Optimized Implementation of the Direct Simulation Monte Carlo Method. *Journal of Computational Physics*, 126(2):328–342, 1996.

[18] Horatiu C. Dragnea and Iain D. Boyd. Simulation of a Nested Channel Hall Thruster. In *34th International Electric Propulsion Conference*, Kobe, Japan, 2015.

[19] Horatiu C. Dragnea and Iain D. Boyd. Axisymmetric Fully 2D Hybrid-PIC Model for Hall Thrusters. In *2018 Joint Propulsion Conference*, 2018.

[20] Horatiu C. Dragnea, Iain D. Boyd, Brian C. Lee, and Azer P. Yalin. Characterization of eroded boron atoms in the plume of a hall thruster. *IEEE Transactions on Plasma Science*, 43(1):35–44, 2015.

[21] Horatiu C. Dragnea, Kentaro Hara, and Iain D. Boyd. Fully 2D Numerical Simulation of a Nested Channel Hall Thruster. In *5th Space Propulsion Conference*, number 1, Rome, Italy, 2016.

[22] Horatiu C. Dragnea, Kentaro Hara, and Iain D. Boyd. Development of a 2D Axisymmetric Electron Fluid Model in Hall Thrusters. In *53rd AIAA/SAE/ASEE Joint Propulsion Conference*, number July, Atlanta, GA, 2017.

[23] Horatiu C. Dragnea, Alejandro Lopez Ortega, and Iain D. Boyd. Simulation of a Hall Effect Thruster with Krypton Propellant. In *53rd AIAA/SAE/ASEE Joint Propulsion Conference*, number July, 2017.

[24] John Michael Fife. *Hybric-PIC Modeling and Electrostatic Probe Survey of Hall Thrusters*. Department of aeronautics and astronautics, Massachusetts Institute of Technology, Boston, MA, USA, 1998.

[25] Roland Florenz. *The X3 100-Kw Class Nested-Channel Hall Thruster : Motivation , Implementation and Initial Performance*. PhD thesis, University of Michigan, 2014.

[26] Jason D Frieman, Hani Kamhawi, George Williams, Daniel Herman, Peter Y Peterson, James Gilland, and Richard Hofer. Long Duration Wear Test of the NASA HERMeS Hall Thruster. In *2018 Joint Propulsion Conference*, Cincinnati, OH, 2018.

[27] Manuel Gamero-Castaño and Ira Katz. Estimation of Hall Thruster Erosion Using HPHall. In *Proceedings of the International Electric Propulsion Conference 2005 (IEPC05)*, pages 1–10, 2005.

[28] L. Garrigues, Iain D. Boyd, and J. P. Boeuf. Computation of Hall Thruster Performance. *JOURNAL OF PROPULSION AND POWER*, 17(4), 2001.

[29] Dan M. Goebel and Ira Katz. *Fundamentals of Electric Propulsion: Ion and Hall Thrusters (JPL Space Science and Technology Series)*. Wiley, 2008.

[30] James M. Haas. *Low-Perturbation Interrogation of the Internal and Near-Field Plasma Structure of a Hall Thruster Using a High-Speed Probe Positioning System*, volume Ph.D. Diss. University of Michigan, 2001.

[31] James M. Haas, Richard Robert Hofer, Dan L. Brown, Bryan M. Reid, and Alec D. Gallimore. Design of the ## Hall Thruster for High Thrust/Power Investigation. In *54th JANNAF Propulsion Meeting*, Denver, CO, 2007.

[32] Scott James Hall. *Characterization of a 100-kW Class Nested-Channel Hall Thruster*. PhD thesis, University of Michigan, 2017.

[33] M. J. Hancock. "solutions to problems for 2d & 3d heat and wave equations," 18.303 linear partial differential equations [online], 2006, pp. 1-4. https://ocw.mit.edu/courses/mathematics/18-303-linear-partial-differential-equations-fall-2006/assignments/probpde3dsolns.pdf, 2017.

[34] Kentaro Hara, Michael J. Sekerak, Iain D. Boyd, and Alec D. Gallimore. Mode transition of a Hall thruster discharge plasma Theory for the anomalous electron transport in Hall effect thrusters Mode transition of a Hall thruster discharge plasma. *Journal of Applied Physics Journal of Applied Physics Physics of Plasmas Journal of Applied Physics II. Kinetic model Physics of Plasmas*, 1151(10):11101–122103, 2014.

[35] William A. Hargus, Gregory M. Azarnia, and Michael R. Nakles. A Comparison of Ion Acceleration Characteristics for Krypton and Xenon Propellants within a 600 Watt Hall Effect Thruster. In *48th AIAA/ASME/SAE/ASEE Joint Propulsion Conference & Exhibit*, Atlanta, GA, 2012.

[36] Michael L. Hause, Benjamin D. Prince, and Raymond J. Bemish. Krypton charge exchange cross sections for Hall effect thruster models. *Journal of Applied Physics*, 113(16), 2013.

[37] Daniel A. Herman, Todd Tofil, Walter Santiago, Hani Kamhawi, James E. Polk, John Steven Snyder, Richard R. Hofer, Frank Picha, Jerry Jackson, and May Allen. Overview of the Development and Mission Application of the Advanced Electric Propulsion System (AEPS). In *35th International Electric Propulsion Conference*, pages 1–14, Atlanta, GA, 2017.

[38] Roger W. Hockney and James W. Eastwood. *Computer simulation using particles*. A. Hilger, 1988.

[39] Richard R. Hofer. *Development and characterization of high-efficiency, high specific impulse xenon Hall thrusters*. PhD thesis, University of Michigan, 2004.

[40] Richard R. Hofer, Dan M. Goebel, Ioannis G. Mikellides, and Ira Katz. Design of a Laboratory Hall Thruster with Magnetically Shielded Channel Walls, Phase II: Experiments. In *48th AIAA/ASME/SAE/ASEE Joint Propulsion Conference & Exhibit*, Atlanta, GA, 2012.

[41] Richard R. Hofer, Ira Katz, Ioannis G. Mikellides, Dan M. Goebel, Kristina K. Jameson, Regina M. Sullivan, and Lee K. Johnson. Efficacy of Electron Mobility Models in Hybrid-PIC Hall Thruster Simulations. In *44th AIAA/ASME/SAE/ASEE Joint Propulsion Conference & Exhibit*, 2008.

[42] Richard R. Hofer, Ioannis G. Mikellides, Ira Katz, and Dan M. Goebel. BPT-4000 Hall thruster discharge chamber erosion model comparison with qualification life test data. In *Proceedings of the 30th International Electric Propulsion Conference*, 2007.

[43] Richard R. Hofer, Ioannis G. Mikellides, Ira Katz, and Dan M. Goebel. Wall Sheath and Electron Mobility Modeling in Hybrid-PIC Hall Thruster Simulations. In *43rd AIAA/ASME/SAE/ASEE Joint Propulsion Conference & Exhibit*, 2007.

[44] Wensheng Huang, Rohit Shastry, George C. Soulas, and Hani Kamhawi. Farfield Plume Measurement and Analysis on the NASA-300M and NASA-300MS. In *33rd International Electric Propulsion Conference*, Washington, D.C, 2013.

[45] J. D. Huba. *NRL PLASMA FORMULARY*. The Office of Naval Research, Washington, DC 20375, 2016.

[46] Automation Creations Inc. Matweb material property data. http://www.matweb.com, August 2013.

[47] Infolytica Corporation. MagNet.

[48] David T. Jacobson and David Manzella. 50 kW Class Krypton Hall Thruster Performance. In *39th AIAA/ASME/SAE/ASEE Joint Propulsion Conference and Exhibit*, Huntsville, Alabama, 2003.

[49] Benjamin A. Jorns, Dan M. Goebel, and Richard R. Hofer. Plasma Perturbations in High-Speed Probing of Hall Thruster Discharge Chambers: Quantification and Mitigation. In *51st AIAA/SAE/ASEE Joint Propulsion Conference 10.2514/6.2015-4006*, Orlando, FL, 2015.

[50] Karl Jousten. PRESSURE MEASUREMENT WITH IONIZATION GAUGES. Technical report, Physikalisch-Technische Bundesanstalt, Berlin, Germany, 1999.

[51] Hani Kamhawi, Thomas W. Haag, David T. Jacobson, and David H. Manzella. Performance Evaluation of a 20 kW Hall Effect Thruster. In *47th AIAA/ASME/SAE/ASEE Joint Propulsion Conference & Exhibit*, number August, 2011.

[52] Hani Kamhawi, Wensheng Huang, Thomas W. Haag, Rohit Shastry, George C. Soulas, Timothy Smith, Ioannis G. Mikellides, and Richard R. Hofer. Performance and Thermal Characterization of the NASA-300MS 20 kW Hall Effect Thruster. In *33rd International Electric Propulsion Conference*, number IEPC-2013-444, pages 1–23, Washington D.C., 2013.

[53] Ira Katz and Ioannis G. Mikellides. Neutral gas free molecular flow algorithm including ionization and walls for use in plasma simulations. *Journal of Computational Physics*, 230(4):1454–1464, 2011.

[54] Donald Kinghorn. "Intel Core-i9 7900X and 7980XE Skylake-X Linux Linpack Performance", Oct. 2017.

[55] A. Kramida, Yu. Ralchenko, J. Reader, and and NIST ASD Team. NIST Atomic Spectra Database (ver. 5.5.6), [Online]. Available: https://physics.nist.gov/asd [2018, July 26]. National Institute of Standards and Technology, Gaithersburg, MD., 2018.

[56] B. C. Lee, J. M. Taylor, R. W. Leach, and A. P. Yalin. Boron nitride erosion measurements of an SPT-70 Hall thruster via cavity ring-down spectroscopy. In *6th Joint Army-Navy-NASA-Air Force Spacecraft Propulsion Meeting*, April 2013.

[57] Brian Christopher Lee. *Real-time erosion measurements of the HiVHAc and SPT-70 Hall thrusters via cavity ring-down spectroscopy*. PhD thesis, Colorado State University, 2014.

[58] Raymond Liang. *The Combination of Two Concentric Discharge Channels into a Nested Hall-Effect Thruster*. PhD thesis, University of Michigan, 2013.

[59] Jesse A. Linnell and Alec D. Gallimore. Efficiency Analysis of a Hall Thruster Operating with Krypton and Xenon. *Journal of Propulsion and Power*, 22(6):1402–1418, 2006.

[60] Jesse A. Linnell and Alec D. Gallimore. Internal plasma potential measurements of a Hall thruster using xenon and krypton propellant. *Physics of Plasmas*, 131(10), 2006.

[61] David Manzella. *Scaling Hall thrusters to high power*. PhD thesis, Stanford, 2005.

[62] David Manzella, Robert Jankovsky, and Richard R. Hofer. Laboratory Model 50 kW Hall Thruster. In *38th AIAA/ASME/SAE/ASEE Joint Propulsion Conference & Exhibit*, Indianapolis, Indiana, 2002.

[63] R. P. McEachran and A. D. Stauffer. Elastic scattering of electrons from krypton and xenon. *Journal of Physics B: Atomic and Molecular Physics*, 17(17):2507–2507, 1984.

[64] Ioannis G. Mikellides and Ira Katz. Numerical simulations of Hall-effect plasma accelerators on a magnetic-field-aligned mesh. *Physical Review E - Statistical, Nonlinear, and Soft Matter Physics*, 86(4):1–17, 2012.

[65] Ioannis G. Mikellides, Ira Katz, and Richard R. Hofer. Design of Laboratory Hall Thruster with Magnetically Shielded Channel Walls, Phase I : Numerical Simulations. In *47th AIAA/ASME/SAE/ASEE Joint Propulsion Conference & Exhibit*, pages AIAA 2011–5809, San Diego, CA, 2011.

[66] Ioannis G. Mikellides, Ira Katz, Richard R. Hofer, and Dan M. Goebel. Hall-Effect Thruster Simulations with 2-D Electron Transport and Hydrodynamic Ions. *31st International Electric Propulsion Conference*, pages IEPC–2009–114, 2009.

[67] Ioannis G. Mikellides, Ira Katz, Richard R. Hofer, and Dan M. Goebel. Design of a Laboratory Hall Thruster with Magnetically Shielded Channel Walls, Phase III: Comparison of Theory with Experiment. In *48th AIAA/ASME/SAE/ASEE Joint Propulsion Conference & Exhibit*, Atlanta, GA, 2012.

[68] Ioannis G. Mikellides, Ira Katz, Richard R. Hofer, Dan M. Goebel, Kristi De Grys, and Alex Mathers. Magnetic shielding of the channel walls in a Hall plasma accelerator. *Physics of Plasmas*, 18(3), 2011.

[69] Ioannis G. Mikellides, Ira Katz, Hani Kamhawi, and Jonathan L. Van Noord. Numerical Simulations of a 20-kW Class Hall Thruster Using the Magnetic-Field-Aligned-Mesh Code Hall2De. In *32nd International Electric Propulsion Conference*, pages IEPC–2011–244, 2011.

[70] Ioannis G. Mikellides, Alejandro Lopez Ortega, and Benjamin Jorns. Assessment of Pole Erosion in a Magnetically Shielded Hall Thruster. *50th AIAA/ASME/SAE/ASEE Joint Propulsion Conference*, pages 1–20, 2014.

[71] A. I. Morozov, Yu. V. Esipchuk, G. N. Tilinin, A. V. Trofimov, Yu. A. Sharov, and G. Ya. Shchepkin. Effect of the Magnetic Field a Closed-Electron-Drift Accelerator. *Sov. Phys. Tech. Phys.*, 17(38):482, 1972.

[72] Michael R. Nakles and William A. Hargus. Background Pressure Effects on Ion Velocity Distribution Within a Medium-Power Hall Thruster. *Journal of Propulsion and Power*, 27(4):737–743, 2011.

[73] Michael R. Nakles, William A. Hargus, Jorge J. Delgado, and Ronald L. Corey. A Performance Comparison of Xenon and Krypton Propellant on an SPT-100 Hall Thruster. In *International Electric Propulsion Conference,*, Ann Arbor, MI, 2009.

[74] J. C. Nickel, K. Imre, D. F. Register, and S. Trajmar. Total electron scattering cross sections. I. He, Ne, Ar, Xe. *Journal of Physics B: Atomic and Molecular Physics*, 18(1):125–133, 1985.

[75] University of Texas. Braginskii equations. https://farside.ph.utexas.edu/teaching/plasma/lectures1/node35.html, 2016.

[76] Alejandro Lopez Ortega and Ioannis G. Mikellides. A New Cell-Centered Implicit Numerical Scheme for Ions in the 2-D Axisymmetric Code Hall2De. In *50th AIAA/ASME/SAE/ASEE Joint Propulsion Conference*, pages AIAA 2014–3621, 2014.

[77] F. I. Parra, E. Ahedo, J. M. Fife, and M. Martínez-Sánchez. A two-dimensional hybrid model of the Hall thruster discharge. *Journal of Applied Physics*, 100(2), 2006.

[78] A. Passaro, F. Nania, and A. Vicini. Full 3D PIC simulation of Hall Effect Thrusters. In *37th AIAA Plasmadynamics and Lasers Conference*, San Francisco, CA, 2006.

[79] Peter Y. Peterson, David T. Jacobson, David H. Manzella, and Jeremy W. John. The Performance and Wear Characterization of a High-Power High-Isp NASA Hall Thruster. In *41st AIAA/ASME/SAE/ASEE Joint Propulsion Conference & Exhibit*, Tucson, AZ, 2005.

[80] Giuseppe D. Racca. SMART-1 from Conception to Moon Impact. *AIAA Journal of Propulsion and Power*, 25(5), 2009.

[81] Astrid L. Raisanen, Kentaro Hara, and Iain D. Boyd. Two-dimensional Hybrid-Direct Kinetic Simulation of a Hall Thruster. In *2018 Joint Propulsion Conference*, 2018.

[82] Justin Ray. Fight to Save US Military Satellite Ends in Remarkable Rescue, jan 2012.

[83] D. F. Register, L. Vuskovic, and S. Trajmar. Elastic electron scattering cross sections for Xe in the 1-100 eV impact energy region. *Journal of Physics B: Atomic and Molecular Physics*, 19(11):1685–1697, 1986.

[84] Bryan M. Reid and Alec D. Gallimore. Plasma Potential Measurements in the Discharge Channel of a 6-kW Hall Thruster. In *44th AIAA/ASME/SAE/ASEE Joint Propulsion Conference & Exhibit*, 2008.

[85] Bryan M. Reid, Alec D. Gallimore, Richard Robert Hofer, Y. Li, and James M. Haas. Anode Design and Veri cation for the ## Hall Thruster. In *54th JANNAF Propulsion Meeting*, Denver, CO, 2007.

[86] R. Rejoub, B. G. Lindsay, and R. F. Stebbings. Determination of the absolute partial and total cross sections for electron-impact ionization of the rare gases. *Physical Review A*, 65(4):042713, 2002.

[87] B. Rubin, J. L. Topper, and A. P. Yalin. Total and differential sputter yields of boron nitride measured by quartz crystal microbalance. *Journal of Physics D: Applied Physics*, 42(20):205205, oct 2009.

[88] Joseph Homer Saleh, Fan Geng, Michelle Ku, and Mitchell L. R. Walker. Electric propulsion reliability: Statistical analysis of on-orbit anomalies and comparative analysis of electric versus chemical propulsion failure rates. *Acta Astronautica*, 139:141–156, oct 2017.

[89] Rohit Shastry. *Experimental characterization of the near-wall region in Hall thrusters and its implications on performance and lifetime.* Aerospace Engineering Department, University of Michigan, Ann Arbor, MI, 7 2011.

[90] Brandon D. Smith and Iain D. Boyd. Computation of total and differential sputter yields of boron nitride using molecular dynamics. In *33rd International Electric Propulsion Conference*, Washington DC, October 2013.

[91] Brandon D. Smith and Iain D. Boyd. Molecular dynamics investigation of hexagonal boron nitride sputtering and sputtered particle characteristics. *Journal of Applied Physics*, 120(5):053301, August 2016.

[92] Brandon D. Smith, Iain D. Boyd, and Hani Kamhawi. Influence of Triply-Charged Ions and Ionization Cross-Sections in a Hybrid-PIC Model of a Hall Thruster Discharge. In *50th AIAA/ASME/SAE/ASEE Joint Propulsion Conference*, pages 1–17, 2014.

[93] Brandon Denis Smith. *A Numerical Study of Wall Erosion and Material Transport in Hall Thrusters.* PhD thesis, University of Michigan, 2015.

[94] George C. Soulas, Thomas W. Haag, Daniel A. Herman, Wensheng Huang, Hani Kamhawi, and Rohit Shastry. Performance Test Results of the NASA-457M v2 Hall Thruster. In *48th AIAA/ASME/SAE/ASEE Joint Propulsion Conference & Exhibit*, Atlanta, GA, 2012.

[95] L. Tao and A. P. Yalin. LIF velocity measurement of sputtered boron atoms from boron nitride target. In *AIAA Joint Propulsion Conference and Exhibit.*, July 2010.

[96] Inc. Tecplot. Tecplot 360.

[97] K. Tinschert, A. Muller, R. Becker, and E. Salzborn. Electron impact multiple ionisation of multiply charged krypton ions. *Journal of Physics B: Atomic and Molecular Physics*, 20(8):1823–1838, 1987.

[98] D. Valentian, J. P. Bugeat, R. Tchuyan, S. Khartov, L. Latyshev, and V. Sierovaiskiy. THEORETICAL AND EXPERIMENTAL ANALYSIS OF STATIONARY PLASMA THRUSTER OPERATION. In *Proceedings of the International Electric Propulsion Conference 1993 (IEPC93)*, pages IEPC–93–226, 1993.

[99] W. G. Vincenti and C. H. Kruger. *Introduction to Physical Gas Dynamics*. Krieger Publishing Company, 1965.

[100] R. W. Wagenaar and F. J. de Heer. Total cross sections for electron scattering by Ne and Ar and Kr and Xe. *J. Phys. B: Atom. Molec. Phys.*, 18(10):2021–2036, 1985.

[101] Mitchell L. R. Walker, Allen L. Victor, Richard R. Hofer, and Alec D. Gallimore. Effect of Backpressure on Ion Current Density Measurements in Hall Thruster Plumes. *Journal of Propulsion and Power*, 21(3):408–415, 2005.

[102] R. C. Wetzel, F. A. Baiocchi, T. R. Hayes, and R. S. Freund. Absolute cross sections for electron-impact ionization of the rare-gas atoms by the fast-neutral-beam method. *Physical Review A*, 35(2), 1987.

[103] John Tamin Yim. *Computational Modeling of Hall Thruster Channel Wall Erosion*. PhD thesis, University of Michigan, 2008.

[104] John Tamin Yim. *Computational Modeling of Hall Thruster Channel Wall Erosion*. Aerospace Engineering Department, University of Michigan, Ann Arbor, MI, 2008.

[105] Jianmin Yuan and Zhijie Zhang. Low-energy electron scattering from Kr and Xe atoms. *Journal of Physics B: Atomic, Molecular and Optical Physics*, 22(16):2581–2588, 1989.

[106] V. V. Zhurin, H. R. Kaufman, and R. S. Robinson. Physics of closed drift thrusters. *Plasma Sources Science and Technology*, 8(1):R1–R20, feb 1999.